Spectral beam splitting for solar collectors

A photovoltaic-thermal receiver for linear solar concentrators

A thesis submitted in fulfilment of the requirements for the degree of Doctor of Philosophy

Ahmad Mojiri

Master of Science in Engineering, University of New South Wales

School of Aerospace Mechanical and Manufacturing Engineering

College of Science Engineering and Health

RMIT University

July, 2016

Declaration

I certify that except where due acknowledgement has been made, the work is that of the author alone; the work has not been submitted previously, in whole or in part, to qualify for any other academic award; the content of the thesis is the result of work which has been carried out since the official commencement date of the approved research program; any editorial work, paid or unpaid, carried out by a third party is acknowledged; and, ethics procedures and guidelines have been followed.

Ahmad Mojiri

July-2016

I would like to dedicate this thesis to my lovely wife, Aza, who unconditionally supported me throughout my PhD.
Thank you Aza!

Acknowledgements

I would like to thank my senior supervisor, Prof. Gary Rosengarten, for his excellent leadership and invaluable technical support. I also thank my co-supervisor, Prof. Kourosh Kalantar-zadeh, for his generous contribution and kind help. I would like to acknowledge the support of Dr Cameron Stanley from RMIT University who contributed to this research by conducting CFD analysis, major support with the experimental rig set-up, uncertainty analysis of the experimental results, and proof reading of the manuscripts.

I also acknowledge the support of Dr Vernie Everett, Ms Judith Harvey, Dr Elizabeth Thomsen and prof. Andrew Blakers from the Australian National University for supplying technical support and PV modules. I thank NEP-Solar and particularly Mr Johan Dreyer for providing a parabolic trough and continuous technical assistance. I also would like to thank Mr Bradly Sherwood, Mr Andre Clemann, Mr Alan Jones, and Mr Paul Porter at the Advance Manufacturing Precinct of RMIT University. In the end, I appreciate the Australian Government and the Australian Renewable Energy Agency for supporting me with APA and PhD top-up scholarships.

Abstract

There is an unprecedented need to transform energy production methods from fossil fuel based to renewable sources. Among these sources, wind and solar energy have gained significant momentum by cost reduction and system efficiency improvement. The cost of silicon PV cells has dropped from 76 dollars per watt in 1977 to below 30 cents per watt in 2015. Photovoltaic electricity has already reached grid parity in some countries including parts of the US and Australia. Solar energy is anticipated to be the world's largest power production method by 2050. However the transition won't be smooth and some challenges are perceived.

Utility scale PV fields can generate cheap electricity but their penetration can be curtailed once they reach 10% of total electricity supply. This is due to the lack of cost effective electrical energy storage. Even ambitious battery cost reduction in the next few years doesn't seem to be able to tackle this issue in short term. Hence, there is a significant need for innovative solar thermal power generators to be combined with PV converters to take advantage of cheap PV electricity and cost effective thermal energy and storage concurrently. The stored thermal energy can be converted into electricity cost effectively when there is no PV output due to absence of solar radiation. Collectors that simultaneously capture sunlight with PV cells and a thermal collector are called PV-T collectors.

Traditional PV-T collectors are made of a PV receiver coupled to a thermal fluid. Since commercial PV cells convert about 15-20% of the sunlight to electricity, the remainder of the light energy dissipates as heat in them. The dissipated heat can be collected by the thermal fluid and delivered as useful energy.

For low temperature applications this can be a suitable method. For high temperature cases such as thermal power plants or industrial heat generators, the PV cells should be thermally decoupled from the thermal absorber because their efficiency and durability deteriorate at high temperatures. This can be achieved by employing spectral beam splitting between the PV cells and the thermal absorber.

In this thesis, a new method for effective spectral beam splitting for high temperature, greater than 120°C, hybrid PV-T receivers for linear solar concentrators is introduced. For this purpose, direct absorption and spectral light filtering using selective thermal fluids and

semiconductor doped glass have been employed to achieve a relatively cost effective design for such receivers. The receiver was built and tested on a parabolic trough which is the first scalable experimental spectral splitting PV-T receiver built and tested in the literature.
The system achieved a 4% electrical conversion efficiency at about 120°C thermal output using silicon solar cells while keeping the cells operating at temperature below 60°C. A high level of thermal decoupling between the cells and the thermal absorber as well as an optical efficiency of over 60% was observed in the proposed system. Some recommendation for improving the systems' efficiency is also provided at the end of this work.

Table of contents

Nomenclature

Greek Symbols

α	angle between pupil normal and r (rad)
β_{th}	thermal beam splitting fraction
δT	temperature difference (K)
η	admittance
η_{pv}	PV cell conversion efficiency
η_{th}	thermal efficiency
γ	angle between r and R
λ	wavelength (nm)
ν	angle of the ray in thin film
Ω	solid angle
ϕ	angle between R and pupil surface normal (rad)
ψ	camera sensor response function
ρ	surface reflectivity
σ	standard deviation
θ	angle between r and object normal (rad)
θ_{mean}	PWMAI
$d\Omega$	solid angle subtended by dS_{en} (sr)

Acronyms / Abbreviations

$I(r, \hat{s}, \lambda)$ spectral directional radiation intensity $(W/m^2/nm/sr)$

$\dot{Q}_{hot,\,loss}$ heat loss from primary thermal absorber (W)

$\dot{Q}_{hot}$ primary absorber heat gain (W)

$\dot{Q}_{in}$ heat input (W)

$\dot{Q}_{loss-air}$ absorber heat loss to ambient air (W)

$\dot{Q}_{loss}$ total absorber heat loss (W)

$\dot{Q}_{PV}$ PV channel heat gain (W)

$\hat{n}$ unit normal vector

$\hat{s}$ unit vector

$\vec{r}$ position vector

a scanned area half width (m)

A_m mirror area (m^2)

A_{EnP} entrance pupil area (m^2)

AOI angle of incidence

B radiance $(W/m^2/sr)$

b scanned area half height (m)

C Lambertianness correction coefficient

CI confidence interval

D_hyd primary absorber hydraulic diameter (mm)

D_i primary thermal absorber diameter (mm)

d_i secondary cooling channel diameter (mm)

d_r physical thickness of layer r

dS surface element area (m^2)

dS' image element area (m^2)

dS_{en} surface element on the entrance pupil (m^2)

F radiant flux (W)

f lens focal length (m)

f_p parabolic trough focal length (m^2)

FF fill factor

G_d beam irradiance or direct normal irradiance (W/m^2)

I current (A)

$I(\theta,\phi)$ radiant intensity (W/sr)

I_λ spectral irradiance ($W/m^2/nm$)

I_λ^T transmitted spectral irradiance ($W/m^2/nm$)

I_{ph} photon generated current (A)

I_{sc} short circuit current

I_s dark saturation current (A)

l parabolic trough length (mm)

l_f individual filter length (mm)

l_pv PV cell length (mm)

M lens magnification

N complex refractive index

n diode ideality factor

P proximity factor

P_λ spectral power

Pr Prandtl number

PV pixel grey-scale value

$PWMAI$ power weighted mean angle of incidence

q total number of layers in thin film structures

R camera target distance (m)

r surface element to pupil element distance (m)

R_m rotation matrix

R_p cell parallel resistance (Ω)

R_s cell series resistance (Ω)

Re Reynolds number

s standard deviation

SE standard error

SR spectral response (A/W)

t tube wall thickness (mm)

t_f filter thickness (mm)

T_m translation matrix

T_λ^T spectral transmission

T_{amb} ambient temperature ($^\circ C$)

T_C secondary cooling channel temperature ($^\circ C$)

T_H primary absorber temperature ($^\circ C$)

V voltage (V)

V_{OC} open circuit voltage (V)

w_a parabolic trough aperture width (mm)

w_f filter width (mm)

w_pv PV cell width (mm)

W_r total receiver length (mm)

X, Y, Z image space coordinates (pixels)

x, y, z object space coordinates (m)

x_c, y_c, z_c camera location vector

x_n, y_n, z_n camera orientation vector

CPV concentrating photovoltaic

CPVT concentrating photovotaic thermal

LMC linear micro concentrator

SDAI standard deviation of angle of incidence

Chapter 1

Spectral splitting and solar energy - a literature review

The content of this chapter has been published as a review and a summary journal articles:
Ahmad Mojiri, Robert Taylor, Elizabeth Thomsen, and Gary Rosengarten. “Spectral beam splitting for efficient conversion of solar energy - a review”. In: *Renewable and Sustainable Energy Reviews 28*(2013)
Cameron Stanley, Ahmad Mojiri,and Gary Rosengarten. “Spectral light management for solar energy conversion systems”. In: *Nanophotonics (2016)*

Efficient energy harvesting from sunlight is considered to be a promising solution to the issues associated with burning fossil fuels. Burning hydrocarbons increases the concentration of greenhouse gases in the atmosphere resulting in adverse climate change. At the same time, depletion of such non-renewable resources in nature increases their prices.
The amount of worldwide energy consumption in 2014 was about 5.61×10^8 terajoules [1] which is equivalent to the average total power usage of about 17.8 terawatts. In comparison, the average radiation on the Earth received from the Sun is about 162,000 terawatts [2]. This implies that harvesting even a tiny fraction of the solar radiation can meet both the world’s current and future energy needs.
Photo-thermal and photovoltaic converters have been developed and commercialised as the two common mechanisms of capturing sunlight and delivering useful energy. Photo-thermal collectors transform the solar radiation into useful heat, while photovoltaic receivers (PV cells) are able to produce electricity directly from sunlight.
The first reported practical conversion of solar radiation into power was carried out by Agustin Mouchot in 1878 [3]. He used a solar thermal collector including a conical reflector

to run a heat engine. The first practical direct conversion of sunlight into electricity using photocells was carried out in the mid-1950s with a conversion efficiency of 6% [4]. Since then the collection and conversion mechanisms have evolved and conversion efficiencies have increased.

PV cells have now reached efficiencies as high as 46% [5] in laboratory measurements. However, such efficiency comes with a very high fabrication cost due to the need to manufacture multi-junction solar cells [6]. Commercially viable cells are mainly mono-crystalline and multi-crystalline silicon cells with module efficiencies ranging from 14 to 20%.

Concurrently with raising the efficiency, the cost reduction of solar conversion devices has been at the focus of research and development in the field of solar energy. Photovoltaic cells, particularly Silicon (Si) based ones, have shown a significant drop in price during the past few decades, from 76US$ per watt in 1976 down to 0.30$ per watt in 2015. This significant cost reduction, has expanded the PV contribution to the energy production portfolio especially during the recent years.

Deploying photovoltaic panels at small and utility scales is able to offset a part of electricity demand in the world. However, the transition from fossil fuels to renewable energy doesn't seem to be smooth. It is argued that once the PV contribution to the power network reaches about 10%, the electrical grid will be reluctant to absorb more intermittent PV electricity [7]. One method to tackle the intermittency problem of photovoltaic electricity is using electrical storages such as batteries. However, they are still an expensive option. Based on the current cost projections, the battery storage cost will remain high in near future. On the other hand, the cost of storing heat is significantly lower. The cost of thermal storage is in the range of 0.11 USD/kWh (for the cheapest sensible heat storage) to 50 USD/kWh (for phase change latent heat storage)[8]. This provides an opportunity for solar thermal systems to play a role in renewable energy industry. By combining these two options, PV and thermal receivers, we can benefit from the advantages of both methods concurrently.

Hybrid photovoltaic-thermal solar collectors (PV-T) are capable of generating heat and electricity concurrently. In traditional PV-T devices, the photovoltaic (PV) cells act as both the electrical generator and the thermal absorber. In those devices, the sunlight strikes the cells and is partially converted into electricity and partially into heat. The generated heat is carried away by a thermal fluid, flowing adjacent to the PV cells, as useful energy (Figure 1.1a). The main shortcoming of this method is the thermal coupling between the PV cell and the fluid which means that acquiring high-temperature heat from the thermal component generally compromises cell performance. To overcome this performance problem, spectral beam splitting has been proposed to thermally decouple the two components; the PV cells and the thermal fluid [9].

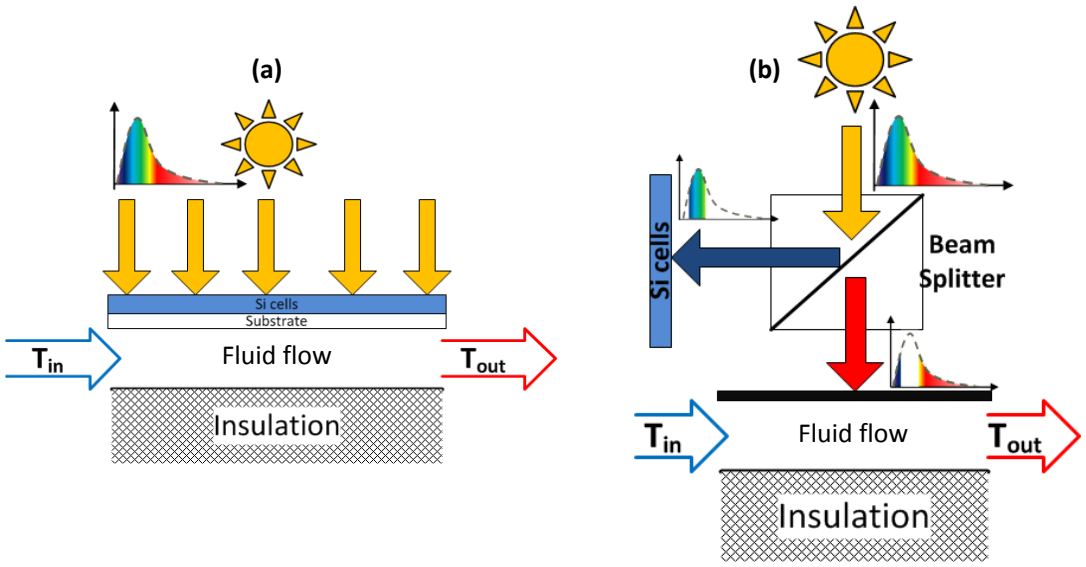

Fig. 1.1 Hybrid PV-T receivers. (a) A thermally coupled traditional PV-T receiver (b) A spectrally splitting thermally decoupled PV-T receiver

By using spectral beam splitting, the broad-band spectrum of the sunlight can be decomposed into different spectral bands. Then each band can be directed to the most suitable receiver for that spectral range, which can be a PV cell, a thermal absorber, or any other photo conversion device. By using such method, the PV receiver and the thermal absorber can be thermally decoupled from each other, and the operating temperature of the thermal receiver can rise to temperatures significantly higher than the temperature of the PV cells (see Figure 1.1b).

1.1 Spectral beam splitting concept

Sunlight on the earth's surface has a spectral distribution in the wavelength range of about 280nm to 4000nm as shown in Figure 1.2. This is due to the equivalent surface temperature of the sun which is approximately 5762K.

Unlike thermal absorbers which capture the whole solar spectrum effectively, PV cells have a fixed, material dependent, spectral response. Photons with energies lower than the band-gap pass through the semiconductor material and are generally absorbed (as heat) by the mounting at the back of the cell. Photons with energies higher than the band-gap are absorbed by the semiconductor material; however, the excess energy is not used by conventional single-junction PV cells, and is generally dissipated as heat. Hence, wavelengths both higher and

lower than the band-gap incur conversion losses, resulting in increased cell temperature that reduces its performance.

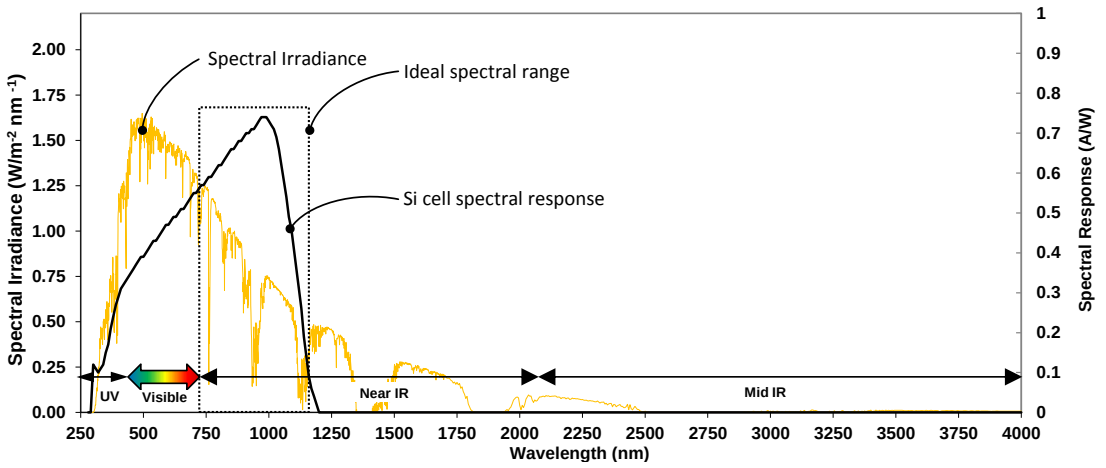

Fig. 1.2 Spectral response of Si cells against the terrestrial spectrum of the direct and circum-solar component of the sunlight; the ideal spectral range (discussed in next chapters) refers to the spectral range that has higher PV conversion efficiency

To quantify the performance of any solar cell across the spectrum, we refer to the "spectral response" (SR) of the cell which is defined as:

$$SR = \frac{I(A)}{P(W)} \tag{1.1}$$

In this equation, I is the current generated by the cell under a monochromatic radiation with the power of P. The spectral response curve of Si cells against the standard airmass 1.5 solar spectrum has been presented in Figure 1.2. The band-gap energy of Si is 1.1 eV which is equivalent to the energy of a photon with 1,127nm wavelength. This means that photons with wavelengths longer than 1127nm are not able to ionise the semiconductor and create electron hole pairs. On the other hand, photons with wavelengths significantly shorter than 1127 nm, have excessive energy that in addition to creating electron hole pairs, releases thermal energy in the cell junction. Photons with wavelengths in the range of about 700 to 1,100nm have energy level close the band-gap energy which means that their energy is mainly converted into electricity resulting in higher conversion efficiency.

The efficiency of a PV cell consisting of a single semiconductor material with a band-gap of 1.1 eV under the full solar spectrum is theoretically limited to about 30% [10]. This can be overcome by using spectral beam splitting. In this approach, light is divided into several

bands and each band is directed to the most suitable receiver. The suitable receivers can be different types of PV cells in lateral multi-junction PV cells (LMPVC) or a completely different type of converter such as a thermal receiver in PV-T systems. Both these options have been investigated by researchers during the past few decades focusing mainly on LMPVCs. Most of those methods of spectral beam splitting can also be applied for PV-T systems. In this chapter, a review on different spectral beam splitting mechanisms is provided and their applicability for hybrid PV-T receivers in linear solar concentrators is explored.

1.2 Spectral beam splitting methods

The concept of harvesting solar energy by splitting the solar spectrum and directing each band to the most efficient converter was suggested for the first time by Jackson [11] in 1955; however the first experimental work was demonstrated by Moon et al. [12] in 1978. This method is still used extensively to address the spectral mismatch problem of solar cells.
A thorough review on the application of spectral beam splitting for efficient harvesting of solar energy has been presented by Imenes and Mills [13]. They reviewed an extensive range of research activities in this field published up to 2003. However, because of high conversion efficiencies and increased design flexibility achieved by spectral splitting, the field has advanced considerably since then.
In this chapter, spectrally splitting solar receivers have bee investigated from the system point of view, including the optical elements (such as concentrators and wave-guides), net combined efficiency, and the type of splitting system used in the configuration. Hybrid configurations which harvest useful thermal energy in addition to electricity have been also reviewed. Next chapters, introduce new methods of spectral beam splitting for linear solar concentrators and investigate their applicability and performance using experimental methods.
Various mechanisms for spectral splitting of sunlight have been proposed. For example, holographic concentrators [14, 15] can split sunlight into several bands along with concentrating it. This mechanism has been shown to be advantageous in low concentration solar collectors [16]. The most well-known method is using thin-film wave interference optical filters as shown in Figure 1.3a. These filters can be designed to function as a band-stop, band pass, or an edge filter. A thorough theoretical background for designing such filters has been provided by Macleod [17].
Rugate filters are another class of wave interference filters that, unlike multilayer filters, consist of a continuously varying refractive index structure along their thickness. Because of

their continuous nature, rugate filters offer higher mechanical strength and toughness, which gives them a high durability under thermal loading in comparison to discrete multilayer filters. A few attempts to introduce selective absorbing/transmitting filters (Figure 1.3b) have been reported as well. A review on the physics of spectrally selective filtering methods has been presented by Peters et al. [18].

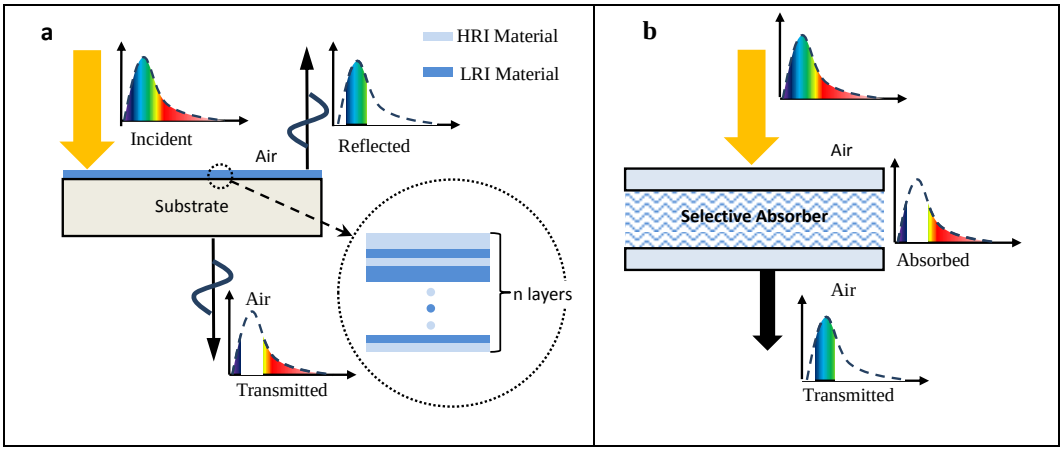

Fig. 1.3 Spectral splitting mechanisms. (a) Spectral splitting using a thin-film wave interference filter; HRI: High Refractive Index and LRI: Low Refractive Index. (b) Spectral splitting using a selective absorber (liquid or solid); the small graphs present the spectrum range available at each stage.

The cost of PV systems utilising spectral splitters is usually higher than the cost of standard PV systems. To be commercially viable, this increase in cost should be offset by the efficiency gain. To achieve this, the optical efficiency of the beam splitter and the concentrating components should be high enough to minimise the optical losses caused by the higher complexity of the system [19, 20]. Durability of such filters under high illumination in concentrating configurations is also a key issue to be addressed [21].

1.2.1 Wave interference filters

Wave interference filters are a mature technology for spectral light management. The theory is well developed [17] and commercial products for some applications are already in the market. These filters are generally made of alternating layers of materials creating step changes in the refractive index (in film structures, see Figure 1.3a) or continuously varying

refractive index layers (in rugate structure). Dependent on the number of layers deposited, the accuracy of their optical thicknesses and low absorption, a large flexibility in optical filtration is achievable. The production method of these filters is mainly physical or chemical vapour deposition (PVD or CVD) in a vacuum.

Needle optimisation is a common method to design multilayer dichroic filters [22, 23]. In this method the design starts with a simple initial configuration such as $0.5L(0.5LH0.5L)^n0.5L$ in which L and H are quarter wavelength optical thickness of low and high refractive index materials respectively, and n is an integer number of repeating stacks. Then the numerical optimisation method varies the thickness of each individual layer to meet a transmission/reflection target by minimising a merit function. The next cycle of needle optimisation starts with adding a new layer to the stack and repeating the thickness optimisation. As there hasn't been any analytical method introduced to uniquely design such filters, the result of needle optimisation can vary with different initial stacks.

For accurate spectral splitting, especially in band pass filters, a large number of layers is required. This can consequently increase the cost and complexity of the filter production [24]. The accuracy in the spectral response of the filter is generally compromised with its cost. The sensitivity of the whole system should also be evaluated against the spectral splitting metrics [25]. It is not always beneficial to add the extra optical components required for spectral splitting as insufficient accuracy can eliminate any expected efficiency gains over a standard system. The total efficiency of the system can drop below the efficiency of a high performance PV cell exposed to the full spectrum. For example Needleman et al. [26] recently showed that for a Si/Cu_2O PV configuration, a variation of more than 10% in the design wavelength band of a dichroic filter meant that a Si cell only will outperform the spectral splitting multi-junction cell.

In hybrid PV-T systems the issue can be less significant since the thermal receiver is normally insensitive to the spectral band in the solar spectrum range. However, any inaccuracy in the filter cut-off wavelength close to the band-gap of the cell can direct sub band-gap photons to the PV cells. These photons can't ionise the semiconductor in the PV cell. Hence all the photon energy will dissipate as heat. Such inaccuracies can rise due to several factors such as inherent filter design approximation (due to compromise between number of layers and performance), fabrication tolerances, incident angle dependency and thermal effects, etc.

Wave interference filters applicability for solar energy conversion is questionable. Although they might be suitable for point focusing systems [27–31], there hasn't been a successful design and demonstration for linear concentrators. Such linear concentrators generate lower concentration levels on the filter and the receiver. Considering the cost of manufacturing such filters, it is highly desirable to apply them under maximum concentration that doesn't

damage them. The possibility of employing them in ground based hybrid systems such as central receivers has been investigated in [32, 24].

A limitation of dichroic filters is their sensitivity to the angle of incidence. Theses filters are designed to match a transmission/reflection target under collimated beam of incident light, while in concentrating systems, especially low profile ones with small f-number, a wide angle cone of light is generated. The light rays with angles deviated from the design angle have a blue shifted transmission/reflection curve [33, 18]. The sensitivity of the system performance to this parameter is of primary importance, whether it is a hybrid or multi-junction PV receiver.

These filters are generally fabricated from non-absorbing materials such as metal oxides. However even a small amount of optical absorption can be problematic under high level of illumination, such as in dish concentrators or central receivers. For example, TiO_2 [32] or Si in amorphous SiN [34] show strong absorption in the short wavelength UV region. Minimising UV absorption in a multilayer structure, may compromise the refractive index contrast between them.

A high refractive index contrast between the materials in thin film filters help to reduce the number of layers and the filter thickness which consequently may reduce the cost and improve filter durability. For example, the refractive index contrast of SiO_2/TiO_2 pair is 1.46/2.7 [17]which is higher than 1.46/2.16 refractive index contrast of SiO_2/Ta_2O_5 , which has less absorption in UV region.

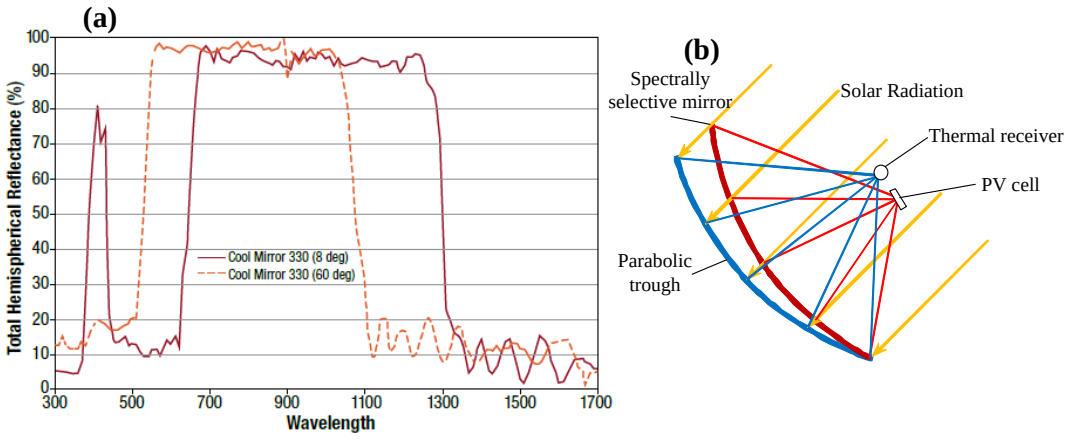

Fig. 1.4 (a) The spectral reflectance of 3M cool mirror film designed for Si PV cells at 8 and 60 degrees of angle of incidence [35] (b) Spectrally splitting hybrid PV-T configuration using polymer reflective films based on the design introduced

In order to overcome the high cost associated with wave interference filters, polymer based spectrally selective reflective films can be applied provided a suitable optical configuration of the whole system is designed. In 2011, 3M introduced Cool Mirror Film 330 [35], which at approximately 20 $\$/m^2$ [36](Figure 1.4a) is less expensive than traditional dichroic mirrors (in the order of 1000 $\$/m^2$). Although this reflective film is very durable under UV exposure, it is not a suitable material to be used under concentrated light due to its inability to withstand heat.

A possible approach that benefits from such reflectors is the design introduced by Vincenzi et al. [37].They suggested using two dish concentrators overlapping each other as shown in Figure 1.4b; one of mirrors is just slightly tilted to have a focal point spatially separated from the focal point of the first dish. The inner dish is covered with a spectrally selective reflective mirror. The mirror behind it reflects all the light transmitting through the inner mirror onto the second focal point. A similar combination may be suitable for hybrid receivers in point focusing and linear concentrators. For example a normal parabolic trough overlapped by another transparent parabolic element covered by spectrally selective film that is slightly tilted can focus different spectral bands of the light on two different focal lines. However it should be taken into account that in single axis trackers the incidence angle on the main mirror can vary significantly either seasonally or daily and reflective films such as the one introduced above show a significant blue shift due to angle of incidence variation.

1.2.2 Diffractive grating modules

Diffractive optical elements, DOEs, are principally based on light diffraction by grating surfaces or volumes. For example, a surface with series of parallel slits steers the light into different directions determined by the size of the slits, wavelength of the light, and AOI of the ray. These elements are capable of carrying out the concentration and spectral beam splitting processes concurrently (Figure 1.5a). By carefully designing the grating structure, different spectral band of the impinging light can be directed and focused onto spatially separate focal lines (Figure 1.5b) or points [38].

These elements can be fabricated using lithography which can be an option for cost effective large area production [39]. They can be designed in two-dimensions to act as a point focusing system but would require two-axis tracking. One dimensional DOEs can also be equipped with a secondary concentrator such as a CPC to achieve point focusing or at least add a degree of concentration in the orthogonal dimension (Figure 1.5c). However, since DOEs are sensitive to the angle of incidence, they should be preferably located prior to the optical concentrator. Hence the spectral separation occurs concurrently with the first stage of the

concentration and then the one-dimensionally concentrated cone of light can be concentrated in the other dimension [40].

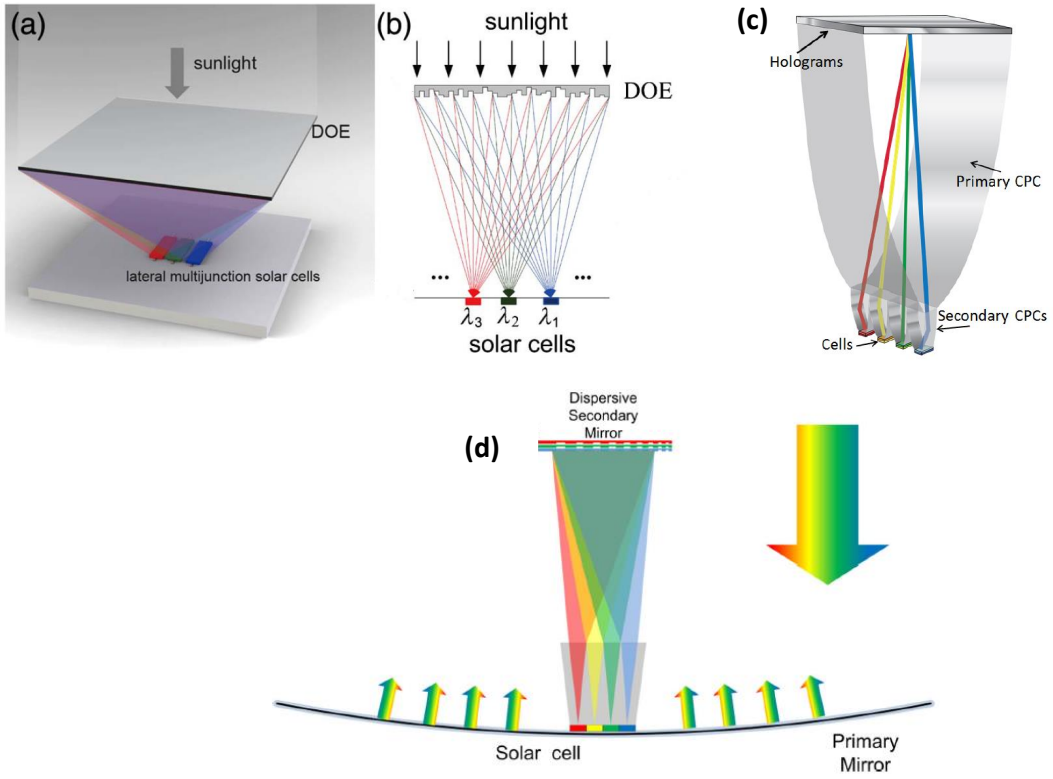

Fig. 1.5 (a) A point focusing DOE for lateral multi junction PV receiver [39] (b) A one-dimensional DOE [39] (c) A One-dimensional DOE accompanied with CPC secondary concentrators [40] (d) Applying DOE close to the focal region of a linear or dish concentrator under concentrated wide angle illumination [41]

Should the aberration from the primary solar concentrator be taken into account, the diffraction element might be applied after the concentrator resulting in less DOE area required (Figure 1.5d). In such a case the spatial and angular profile of the concentrated light on the DOE close to the focal region of the primary solar concentrator should be determined. Yao et al. [41] showed the possibility of using multi-layer sub wavelength diffractive elements at the focal region of solar concentrators. The sub wavelength nature of these elements allows the spectral band of the sunlight within the reflection band of the DOE to be reflected while the rest of the spectrum transmits to the next layer with minimal attenuation. Such multi-layer structure can cover most of the solar spectrum using simple DOEs as its layers. By adjusting

the diffraction angle of the elements, spectral sub bands of the light are concentrated on spatially separated focal points. So far the published work has focused on the proof of concept simulations and measurements without any practical-scale outdoor implementations.

1.2.3 Refractive methods

Unlike diffractive elements, refractive devices operate based on the spectral dependent refractive properties, i.e. dispersion characteristics, of transparent materials. In such devices, the collimated light is refracted through a set of prisms that are arranged in a specific geometrical configuration. The arrangement should be in such a way that it concentrates the refracted light onto a focal line or point [42] (Figure 1.6a). By choosing a refractive material with suitable dispersion properties, different spectral bands can be directed towards spatially separated focal regions [43, 44] (Figure 1.6b). The research in this field is so far limited to multi-junction PV receivers but it can be also a suitable low cost approach for hybrid linear collectors.

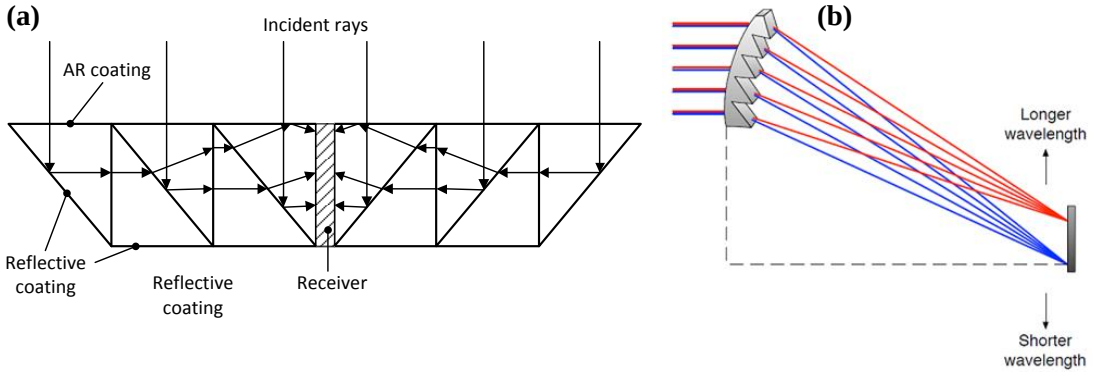

Fig. 1.6 Refractive approach in light management [42]. (a) A refractive wave-guide concentrator (b) A refractive concentrator/spectral separator[44]

The surface quality of such optical devices should be high enough to prevent light scattering. Such qualities are readily achievable using diamond machining of the molds or the optical material itself [45]. Injection molding with such quality molds could be a promising option for large scale low cost production. The separated spectral bands in these refractors may show an overlap between the bands leading to efficiency losses.
Stephancich et al. [46] suggested a two-dimensional concentrator that uses an array of prisms

with varying apex angle on a curvilinear configuration. In order to achieve a spectral separation effect, they proposed using polycarbonate as the lens material, which has a high level of transmittance in the 400-1,300nm range. Polycarbonate has a high chromatic dispersion coefficient which helps to separate different spectral bands of light and focus them on separate regions. By tuning the geometry of the lens, suitable spectral splitting can be achieved for PV receivers. They recently [47] considered the same concept for a point focusing configuration by tilting one face of the prism to add another dimension to the concentration effect.
The potential of this method is not limited to PV receivers. The linear two-dimensional lens can be also applied for hybrid receivers. The fabricated two-dimensional lens presented the capability to concentrate light but a significant level of spectral overlap was observed [46].

1.2.4 Luminescent solar concentrators

Luminescent solar concentrators (LSCs) are generally made of a wave-guide such as a flat transparent slab doped with tiny absorbing/re-emitting elements called chromophores. These elements can be quantum dots [48] or dye particles [49]. These chromophores absorb diffuse and beam radiation entering the slab and diffusely re-emit it. The re-emitted light propagates towards the top and bottom faces of the slab. A portion of the re-emitted light that strikes the surfaces at angles larger than the critical angle are confined within the slab by total internal reflection and directed towards the perimeter of it. Since the edge area can be significantly smaller than the aperture are of the slab, light concentration can be achieved.
A main advantage of these devices is eliminating the necessity of tracking to achieve concentration. They can capture the sunlight striking their aperture at any angle, and partially direct it towards the receivers at their edges. This gives them the capability to collect the diffuse component of the light which standard optical concentrators cannot.
Although there hasn't been any successful efficient LSC mass produced for solar energy applications, there is still significant potential for this idea to be applied in spectral splitting receivers. The chromophores within the LSC generally absorb a specific band of light and ideally emit at a different band. This absorption/emission spectral variation is called Stokes shift. By combining one type of LSC with another one with a different absorption spectrum, different bands of light can be collected and directed to various receivers; these receivers can be PV or thermal. LSCs optical efficiency is affected by some loss mechanisms such as [50]:

1. non-perfect total internal reflection at the front and back side

2. less than 100% absorption efficiency of chromophores in LSC

3. quantum efficiency of the chromophores (how many photons are emitted per the photon absorbed)

4. the energy loss due to stokes shift, i.e. the photon will lose a portion of its energy when it is red shifted

5. the absorption by the wave-guide

6. re-absorption of the emitted light due to non-ideal stokes shift

1.2.5 PV assisted natural spectral splitting

Using this terminology, we refer to the idea of applying the intrinsic properties of PV cell semiconductor materials as the quantum converter and spectral splitter simultaneously. In this method, the PV cell equipped with a quality back reflector is exposed to the sunlight, either concentrated or non-concentrated [51] (Figure 1.7). The spectral band within the absorption region of the PV semiconductor material is naturally absorbed and converted into electricity by the cell. The remainder of the spectrum transmits through the cell and is reflected by the back reflector towards an adjacent complementary receiver, i.e. another PV cell with a narrower band-gap or a thermal receiver.
One of the initially proposed systems that uses PV cells in the mirror structure of a concentrator is the work done by Barber et al. [52] which uses TiO_2 dye-sensitised solar cells (DSSC) covered by a dichroic filter as concentrating mirrors of a Fresnel structure (see Figure 1.7a and b). The incident light on these reflector elements is partially reflected to a Si cell at the focal line of the system. Since the DSSC cell used in this design suffers from low transmission beyond its band-gap, instead of a back reflector, a dichroic mirror in front of the TiO_2 DSSC was used. By employing a more suitable cell that has a higher transmission in sub band-gap wavelengths, the necessity for the dichroic mirror can be eliminated.
More expensive highly efficient cells such as GaAs are also considered for natural spectral splitting. However their applicability may remain limited to designs such as the one presented in Figure 1.7c and d. In such configurations, the secondary concentrator can be made of a mid-band-gap cell such as GaAs as the spectral splitter and reflector towards a thermal receiver [53]. In this proposed configuration the GaAs covered mirror along with the thermal receiver is located inside an evacuated tube. The tube is expected to reach 400°C but due to the presence of vacuum the heat transfer phenomena from the tube to the cells is radiation only. This radiative flux along with the absorbed concentrated light by the cells creates significant heat load on it and since there is not any strong passive cell cooling mechanism, an active heat removal method, such as a liquid micro channel attached to the cells, is required

[54]. Since the cell is located at the focal region, it will not collect the diffuse component and the system will lose the capability to operate under cloudy condition.

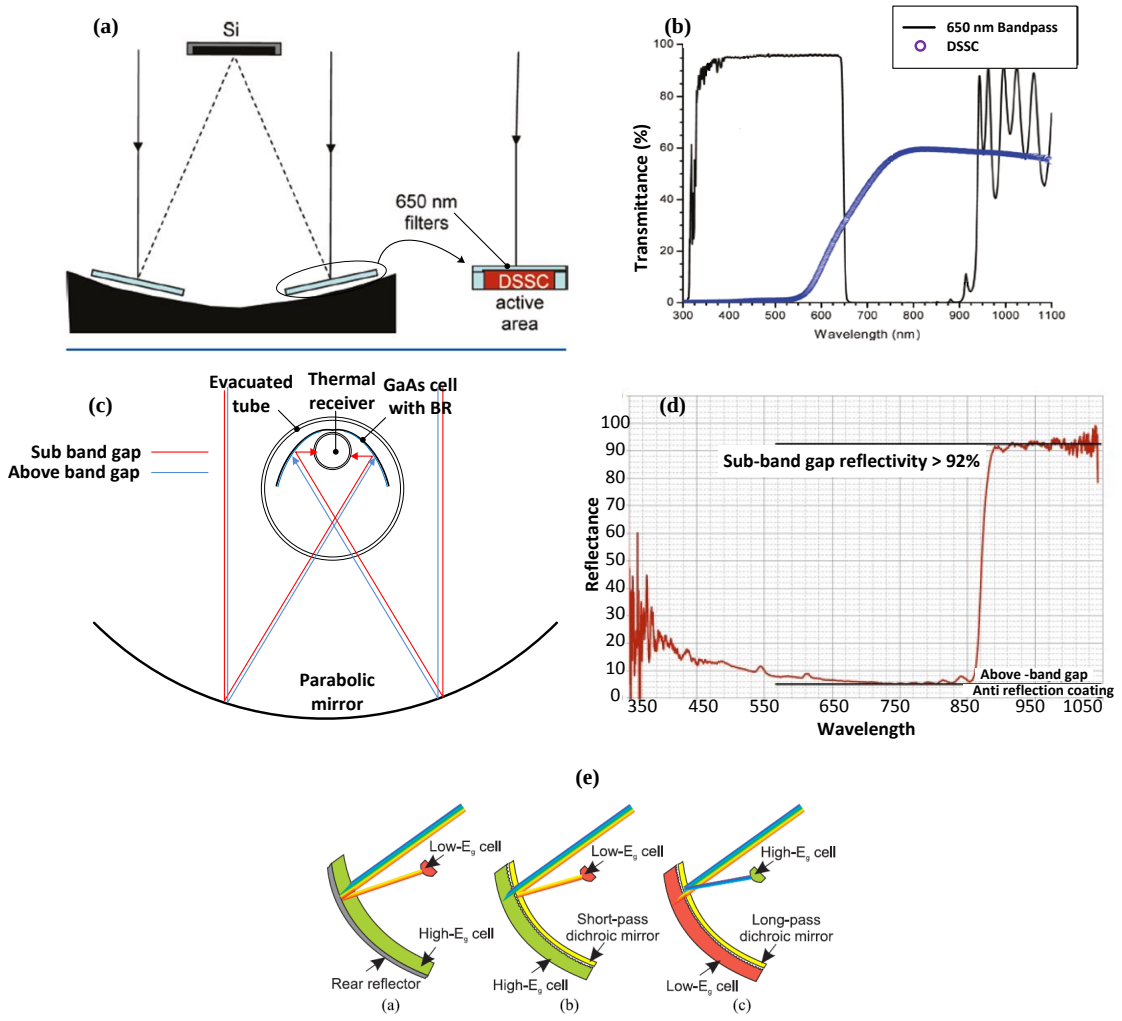

Fig. 1.7 (a) Using PV cells in the structure of concentrating mirrors; the cell is covered by dichroic reflectors [52] (b) The spectral transmission of the components in figure a [52] (c) Using GaAs thin film PV cells in front of a secondary reflector in a concentrating hybrid PV-T system [53] (d) The reflectance of the back reflector GaAs cell used in figure c [53] (e) Using low cost thin film PV cell as a coating of linear concentrators [36]

The PV cell can be deposited on the main concentrating mirror to allow the system to collect and convert the diffuse component of the light as well. Recently, Zhengshun et al. [36] theoretically studied this concept by investigating a hypothetical parabolic mirror made of $Cd_{0.5}Zn_{0.5}Te$ for a PV-PV and PV-T receiver. In these configurations, the cells should form

a curved structure to accommodate the necessary parabolic shape for linear concentrators. In case of using thin film cells, the semiconductor material can be deposited on surfaces such as a curved glass or existing parabolic mirrors. To use silicon cells as the cover of the concentrating surface, sliver silicon cells [55] could be a suitable candidate due to their structural flexibility.

Such cells can also be located in parabolic troughs but covered with a dichroic reflector, preferably low cost polymer films, without any back reflector. In that case the light suitable for the low cost PV can transmit though the film to the cells and the remainder of the spectrum can be reflected to the thermal receiver or secondary more expensive PV material at the focal region of the concentrator. Semiconductors made of $CdTe$ alloys with Mg, Zn, or Mn can have a band-gap in the range of 1.48eV to 3.5eV and are suitable candidates covering the main mirror.

The important advantage of such PV assisted concentrators is their capability to collect the diffuse component of the sunlight which is mostly missed in traditional concentrators. About 80% of the AM1.5 diffuse component is in the 300-800nm range which can be collected effectively by such high band-gap cells. More research is required to identify the suitable low-cost high-band-gap solar cells for this purpose [56].

A combination of these two methods (main mirror covered by low-cost high-band-gap cells and a secondary concentrator made of mid band-gap cell such as $GaAs$) is also envisioned to overcome this drawback and benefit from spectral splitting. The diffuse component of the light can then be collected by the cell on the primary mirror. The beam component can be reflected to the secondary concentrator to generate more electricity while the sub band-gap wavelengths end up being absorbed by a high temperature thermal receiver. The current literature review suggests that such systems haven't been studied or tested yet.

1.2.6 Emerging spectral splitting methods

Nano-fluid based optical filtering has significant potential in spectrally splitting hybrid receivers as they can simultaneously operate as the heat transfer fluid and the spectral splitting device. These filters can be made of a sustainable suspension of one or more nano-particles in liquids such as synthetic oil, water, and glycols for direct absorption of the sunlight [57]. Nano-particles depending on their geometry, size, and materials can show plasmonic absorption in certain spectral bands. The base liquids also can be selected wisely to absorb long wavelengths with a cut-off in near IR range [58, 59]. Although this is a promising option, more research is required to address some challenges such as:

1. Producing nano-particles with a tight size distribution at low cost; size variation leads to absorption at different wavelength resulting in smooth transition from transmitting to absorption state
2. Small core shell sizes less than 50nm [59]
3. Stable suspensions without particle conglomerating [59]
4. Designing transparent thermal insulation for the aperture of volumetric receivers to suppress heat loss
5. Stable nano-particle optical properties at higher temperatures; thermalisation of the nano-particles changes their geometry, aspect ratio or shell size, which consequently alters their optical properties [60]

Recently, Crisostomo et al. [61] reported an outdoor measurement results of a spectral splitting linear hybrid receiver based on silver/silica core shell nano-discs suspended in water. The <5 nm silica shell of the particles is expected to prevent thermal and UV degradation. This nano-fluid shows strong absorption in short wavelengths below 700nm. The size variation of the nano-particles from the nominal values still reduces the sharpness of the filter cut-off. The base liquid, water, has strong absorption in IR range and the resultant nano-fluid presents a band pass filter with a window of about 700-1,100nm range.
Suitable strong absorption by nano-particles in the IR range together with high transmission in short wavelengths (for example for GaAs cells) is difficult to achieve by spherical particles. Nano-rods with tunable aspect ratios and triangular nano-plates with tunable thickness and diameter show potential to be applied in such cases [60].
Reaching high temperatures with water based nano-fluids in direct absorption receivers is challenging. More research and engineering work is required to design transparent receivers that can be pressurised effectively to prevent boiling. Another option to overcome the boiling problem is replacing water with a low vapour pressure liquid. The heat transfer, electrical, chemical, and optical properties of a range of liquids have been examined for this purpose [62]. Although there is adequate knowledge about the thermal aspects of these liquids, their optical properties haven't been studied in detail.
Glycols such as propylene glycol and ethylene glycol have suitable IR absorption [58] which is due to the $O-H$ bond in their molecular structure. Their boiling point is about 197°C and 188 °C respectively. By switching to other liquids such as mineral and silicon oil, the IR absorption vanishes [63] which is not suitable for most of the solar cells including Si. However enhancing IR absorption in such liquids using nano-particles may improve their applicability for hybrid PV-T receivers.

Two-dimensional materials such as transition metal dichalcogenides (TMDCs) are also being considered for selective light absorption due to their band-gap tunability [64]. These materials have a formula of MX_2 where M is a transition metal from group IV, V, or VI and X is a chalcogen (S, Se, or Te). By changing the number of layers or introducing interlayer dopants, the band-gap of these materials vary. For example, mono-layer MoS_2 shows a band-gap energy of 1.82 eV which reduces to 1.65 eV and 1.35 eV in two-layered and three-layers structures [65].

1.3 Spectral splitting in PV receivers

This section reviews the design and performance of spectral splitting for PV receivers. Most, but not all, of such systems have been designed for concentrated radiation. These designs can be classified into two categories: proof of concept and integrated designs. At the proof of concept stage, concentrating devices are not "optimally" combined with the beam splitting and/or receiver components. The main aim of such research is to evaluate the effect of spectral splitting on the efficiency of PV cells. Thus, this research feeds into and helps to improve the performance of the second category - integrated designs. The designs in the latter category are aimed at configurations with more manufacturability and/or less cost.

1.3.1 Proof of concept designs

The configuration of a typical concentrating spectral splitting PV system consists of a concentrating device such as a lens or a dish [66] combined with a spectral splitter close to the focal region of the concentrator. The splitter acts as a selective mirror to create two different focal points. The splitter may have a curved surface rather than a flat one to address the effects associated with non-collimated rays on the wave interference filters [18]. An advantage of using curved mirrors is shifting the focal point of the concentrating system to provide a suitable geometry for locating the receivers [67–71]; otherwise, the receivers could cause shading and thus optical losses.

In theory, dividing the spectrum into many bands and directing each band to a matched cell can achieve very high solar conversion efficiencies. In order to verify this, Zhao and Sheng divided the spectrum into three [73] (excluding the monolithic separation of light in the tandem cell) and five bands [75] as shown in Figure 1.8b and Figure 1.8d respectively using consecutive wave interference mirrors. Their systems achieved 38% and 35.6% efficiencies at 2.8X concentration in three and five band systems, respectively. Presumably, the added complexity of increasing the number of sub-bands resulted in a lower total practical effi-

ciency.

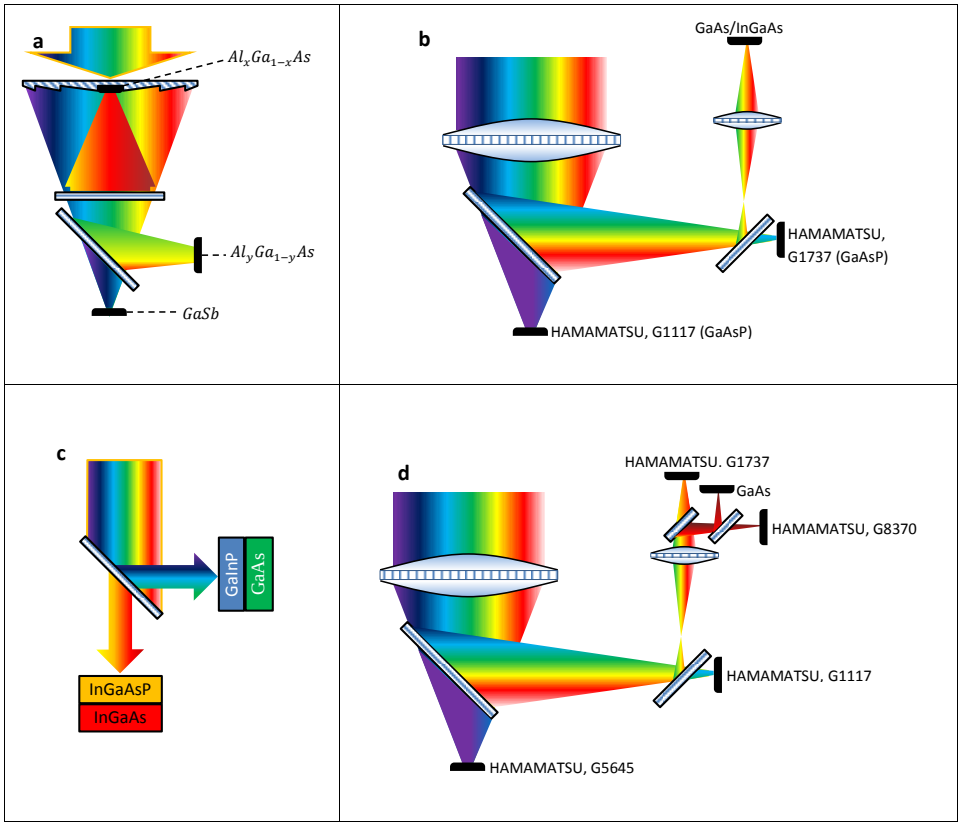

Fig. 1.8 Spectral splitting for PV conversion of sunlight. (a) A concentrating PV system enhanced by two dichroic mirrors dividing the spectrum into 3 bands; $0.3 < x < 0.35$ and $0 < y < 1$ [72]. (b) A concentrating PV system utilising two dichroic mirrors and one tandem cell dividing the spectrum into four bands [73]. (c) A non-concentrating PV receiver with one dichroic mirror that splits the sunlight into two bands which are monolithically separated again in the tandem cells resulting in conversion of light in four separate bands [74]. (d) A concentrating PV system utilising four dichroic mirrors dividing the spectrum into five bands [75].

Xiong et al. [74] suggested that to achieve high efficiencies through practical systems, the solar spectrum should not be divided into too many bands because the splitting losses will affect the total efficiency of the system. Spectral splitting losses include sloped transition from reflection to transmission, non-ideal cut-off wavelengths, and reflection losses of the mirrors. For example, the efficiency of the system shown in Figure 1.8c can decrease by 3%

if the transition range (the spectral range between highly transmissive to highly reflective regions) of the filter increases from 10 nm to 100 nm [74]. In addition to the splitting effects, different p-n junction arrangements in the systems similar to Figure 1.8 can significantly change the total efficiency. For example, Morki et al. [76] used an arrangement similar to Figure 1.8c with a Si/Ge dual junction cell and a GaAs single junction cell showing that different p-n arrangements of the cells can theoretically result in a 2.76% efficiency change. Non-ideal cut-off can occur because of the effect of the light incident angle on the filter, the limited number of deposited layers, and manufacturing inaccuracies in filter fabrication process [20]. Figure 1.8 shows that the incident angle on the spectral splitter in concentrating configurations can vary significantly. Hence, the geometrical configuration should be optimised to minimise or account for such incident angle variation.

Some researchers have attempted to combine light trapping with spectral beam splitting to decrease the reflection losses of the optical devices in spectrally splitting systems. For example, Mitchell et al. [77] proposed the configuration shown in Figure 1.9a. In this system, the reflection losses can be minimised because any light reflected from the surface of a beam splitter or a cell will be captured by another one. Although the figure shows the configuration under non-concentrated sunlight, the receiver can be optimised to work under concentration as well.

Unlike the configuration presented in Figure 1.9a, the design in Figure 1.9b [51] is capable of collecting light from a large aperture area. Here, total internal reflection is used to trap the light inside the optical receiver and just one type of dichroic mirror is used to split the light between high and low band-gap PV cells. When light strikes the long pass filter, the long wavelength range of the spectrum is transmitted through the filter and absorbed by the low band-gap cell. The short wavelength range is reflected to the high band-gap cell. On the other hand when light reaches the high band-gap cell, the short wavelength range is absorbed by the cell and the longer range is transmitted through that and reflected by the highly reflective mirror at the back of the cell to the low band-gap cell.

In order to take advantage of concentrated illumination in light trapping, Goetzberger et al. [78] suggested configurations as presented in Figure 1.9c. The light is concentrated by the lenses and then sent through a tiny opening into the trap. The radiation inside the trap is transformed into diffuse light using randomising Lambertian (diffuse) reflectors. Each solar cell inside the trap is covered by a band pass mirror which transmits the optimised wavelengths associated with its band-gap and reflects the rest of the spectrum. All other surfaces inside the trap are highly reflective.

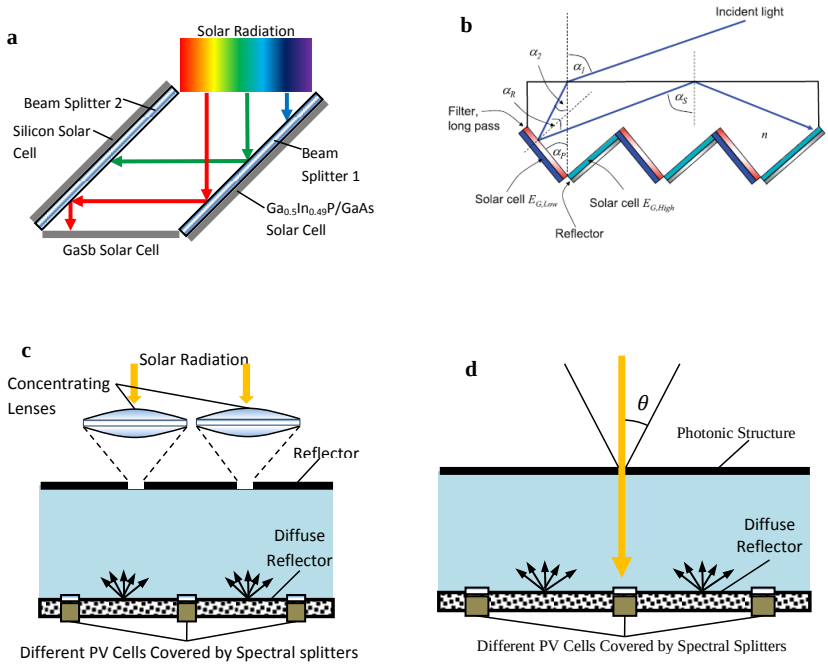

Fig. 1.9 Spectral splitting in light trapping PV receivers. (a) A light trap enhanced by two dichroic mirrors and three different solar cells in a 45°parallelepiped form [77]; beam splitter 1 and 2 transmit the wavelengths shorter than 850 nm and 1080 nm respectively and reflect the rest. (b) A light trapping receiver using total internal reflection; just one type of dichroic mirror is required for this configuration (shown by the red rectangle); long wavelengths passing through the high band-gap cells are reflected by the simple mirror at the back of them [51]. (c) Spectral Splitting for PV conversion using a set of concentrating lenses, a light trap, and small spectral mirrors [78]. (d) A light trapping receiver with a photonic structure with acceptance angle of θ replacing the concentrating lenses and the top reflector of the design in c [78].

A photonic structure with angular selectivity of not less than 0.27°(which is the angle subtended by the sun) can replace the top reflector and the concentrating lenses (Figure 1.9d). In this case all radiation inside the cone with the above angle will enter the light trap and be reflected by the diffuse reflector. Since the acceptance angle of the photonic structure is very small, the major part of the reflected light will be trapped inside the structure resulting in concentration of sunlight without the need for lenses. However, this method does require two-axis tracking.

Another option to decrease the optical losses is to concentrate and split the light in a single stage using a single device. The advantage of this arrangement is that it decreases the number of interfaces and consequently the reflection losses. Such a device can be made of a set of

prisms implemented on a curved surface [46] (Figure 1.6b) or dichroic concentrating mirrors (Figure 1.4b) to produce spectral splitting and concentrating effects at the same time.

1.3.2 Integrated designs

Incorporating concentrators, wave-guides, and various receivers in a practical compact system can be challenging. The external design should aim at reducing wind loads, increasing light acceptance, and providing satisfying aesthetics. Moving parts should be minimised as much as possible. A possible solution to address these challenges is using planar concentrators [79–82] or an array of small concentrating devices combined with spectral splitters [83–86] (Figure 1.10).

In a compact configuration, eliminating the shading problems from components is essential in achieving high efficiencies [87]. The arrangement shown in Figure 1.10a could suffer from shading effects induced by the top cell and the splitter, while the arrangements shown in Figure 1.10b and c addresses this problem.

A project to build a planar spectral splitting concentrated PV system with over 50% conversion efficiency was proposed by Barnett et al. [29, 88] in 2006. The preliminary design of the system is shown in Figure 1.10c. The total efficiency of such configurations is equal to the product of the optical and cell modules efficiencies [89–92]. The system achieved a maximum total efficiency of 39.1% at 30X concentration.

By changing the type of Si cells used in the system to UNSW's ZT-1-4E (PERL) Si cells, the efficiency of the cell (not the total efficiency) was shown [93] to be increased to $43.0 \pm 1.9\%$ because of better spectral match of the cells and higher conversion efficiency of the PERL cells. Moreover, options for improving the optical efficiency were proposed which would increase the total efficiency further. These options included using efficient anti-reflection (AR) coatings on the concentrating surfaces, optimising the dichroic mirror, decreasing the reflection losses from the dichroic mirror, and decreasing the reflections from different interfaces by immersing all components in silicone [30].

A significant portion of sunlight is missed in concentrating devices since they are not able to capture the diffuse component. A non-concentrating planar receiver as shown in Figure 1.11a [56] can collect the global radiation. A novel method to help capture diffuse radiation in concentrating systems is to use selective mirrors to concentrate the sunlight [52]. Such mirrors can be short-pass mirrors and since the diffuse component contains mainly the shorter wavelengths it can transmit through the mirror and be absorbed by a high band-gap cell at the back of the mirror (Figure 1.11b). The design proposed in this figure is an example of configurations that combine spectral splitting and concentration of sunlight into a single stage

[37] (however the diffuse component is not concentrated).

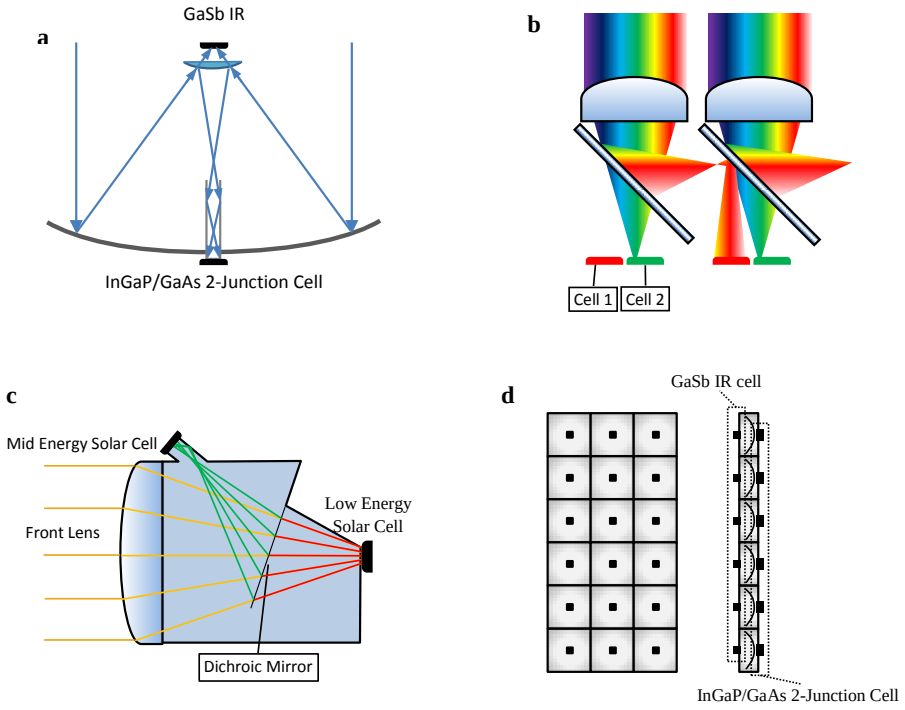

Fig. 1.10 Planar concentrating spectrally splitting PV systems. (a) A concentrating PV system using a Cassegrainian concentrator, dichroic hyperbolic mirror, and a light guide [94]. (b) A compact spectral splitting concentrating PV system consists of 2 types of cells which can be packed into larger compound planar collectors; each module consists of a concentrating lens which is integrated with a dichroic reflector [95]. (c) A concentrating PV configuration with less optical losses; the mirror has been located at an angle of 24°with respect to the optical axis of the front lens to address the shadowing problem of the Mid-E cells [30]; the whole optical component has been made of the same material to reduce optical discontinuities and alternatively Fresnel losses (d) a planar collector comprised of an array of the small modules mentioned in a. Modules similar to those mentioned in b and c can also be packed into the same array.

Table 1.1 summarises some of the important results of the outcomes of different papers. It should be mentioned that some papers have not reported any measured value for their designs and have relied on mainly theoretical predictions. Also not all papers presenting measured efficiencies have explained their measurement procedures in detail. Hence, some uncertainties are expected in some of these values. For research that has included optical losses in its reported efficiency, the total efficiency has been cited.

Table 1.1 Summary of selected beam splitting devices in the literature; "Number of Bands" refers to the bands that are created by the spectral splitting filter. This may be different to the number of PV receivers because, for example, in some cases multi-junction PV cells are used to capture a band.

Ref	System Type	Cell Type	# of Bands	Calculated Eff.	Measured Eff.
39	Concentrated	AlGaAs/Si, InGaAsP/InGaAs	2	26.8%	Not-Tested
40	Concentrated	Ge, AlGaAs	2	18.7%	Not-Tested
41, 42	Concentrated	GaAs/Ge, Si	2	25.71%	Not-Tested
45	Concentrated	GaAsP1, GaAsP2, GaAs/InGaAs	3	-	38%
46	Concentrated	GaAsP(470 nm), GaAsP(600 nm), GaAsP(700 nm), GaAs, InGaAs	5	42.7%	35.6%
47	Non-Concentrated	GaInP/GaAs, InGaAsP/InGaAs	2	31.8%	29.2%
38	Concentrated	AlGaAs, GaAs, GaSb	3	49.4%	39.6%
93	Concentrated	GaInP/GaAs, GaSb IR	2	32.4%	32.9%
95	Concentrated	GaInP/GaAs, Si, GaInAsP/GaInAs	2	Not Provided	42.7% $\pm$ 2.5%
68	Concentrated	GaInP/GaAs, GaInAsP/GaInAs	2	Not Provided	39.1%
69	Concentrated	GaInP/GaAs, Si (PERL), GaInAsP/GaInAs	2	43%	Not-Tested
96	Concentrated		2	39%	38.5% $\pm$ 1.9%
71	Non-Concentrated	Pc-Si, GaInP	2	18.4%	Not-Tested
72	Concentrated	Si, Dye-Sensitized Cells	2	20%	Not-Tested
73	Concentrated	Si, GaInP	2	29.5%	Not-Tested
49	Non-Concentrated	GaInP/GaAs, Si, GaSb	3	Not Provided	34.3%

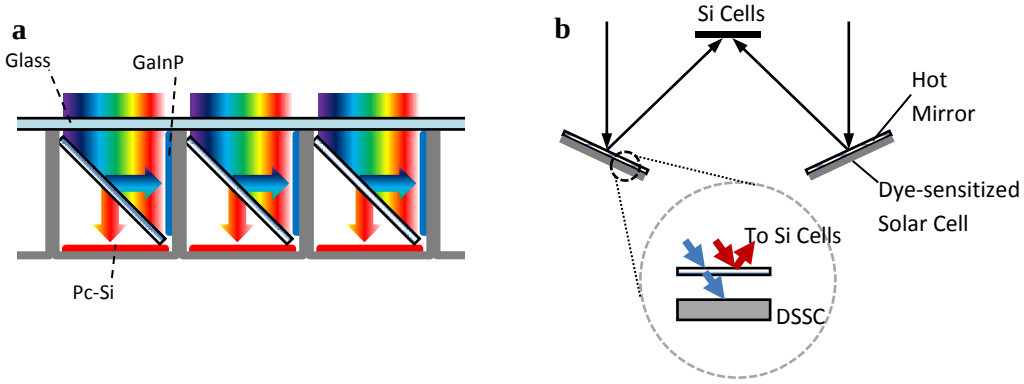

Fig. 1.11 Spectral splitting devices capable of capturing the global (diffuse and direct) radiation. (a) A non-concentrating PV receiver; the mirror was made of 48 layers of TiO_2 and SiO_2 with cut-off wavelength at 675 nm [56]. (b) The hot mirrors reflect the long band to Si cells and transmit the short one to DSSC (Dye-Sensitised solar cell) [52]

1.4 Spectral splitting in hybrid receivers

In spectral beam splitting hybrid PV-T receivers, the aim is to send only some of the spectrum to the PV cells while the rest is sent to a thermal receiver to produce heat. For example, Maghanga et al. [98] introduced a cut-off mirror made of a layer of $TiO_2 : Nb$ and a layer of Al_2O_3 deposited on a substrate of aluminium. This mirror reflects 75.6% and 28% of sunlight below and above 1100 nm (near the band-gap of Si), respectively. The non-reflected radiation can be absorbed and delivered as useful heat. Segal et al. [96] investigated the feasibility of implementing spectral splitting in solar power towers to co-generate electricity and heat through separate PV and thermal receivers (Figure 1.12a).

A challenge associated with wave interference splitters in solar power towers is the effect of significant variation of angle of incidence on the receiver due to the large area of heliostat field (Figure 1.12b). A potential solution for addressing this problem is dividing the beam splitter into small segments and optimising each one according to the weighted mean angle of incidence [19, 24, 99].

Spectral splitting can also be implemented in parabolic troughs. For example, Jiang et al. [100, 101] used Nb_2O_5 and SiO_2 to fabricate a spectral splitter to produce electricity through PV cells and a high quality thermal output with temperature in the range of 250 to 400°C in a hybrid parabolic trough; however they have not reported the expected electrical output from the PV cells.

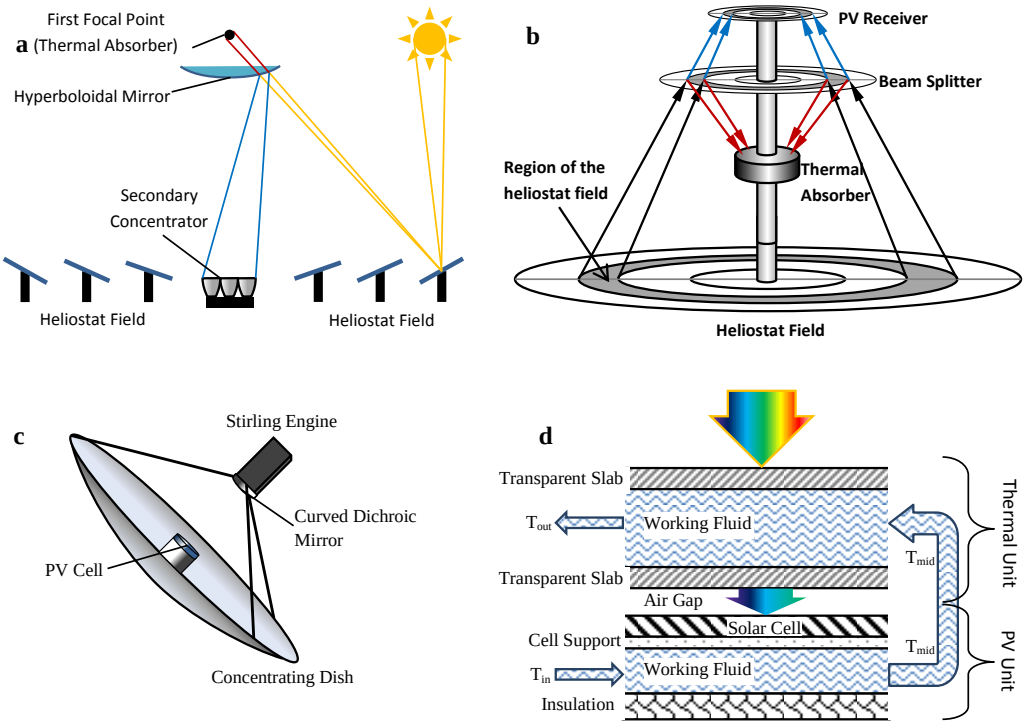

Fig. 1.12 Spectral splitting in hybrid receivers. (a) Spectral splitting in solar power towers using a hyperboloidal mirror with a radius of 23.8m; 70% of the radiation can be captured effectively [96]. (b) Hybrid solar power tower enhanced by a flat dichroic mirror optimised for the effect of incident angle on the beam splitter [24]. (c) Hybrid collector consisting of a dish concentrator, PV cell, and a Stirling engine; the filter was made of 78 layers of TiO_2 and SiO_2 to provide a reflective window from 600 nm to 1050 nm; a combined efficiency of 28% at about 600 suns concentration level can be achieved [97]. (d) Schematic of a hybrid solar collector using a selective absorbing/transmitting fluid; T_{in} and T_{mid} are inlet and outlet temperatures of the solar cell cooling channel; T_{out} is the outlet temperature of the hybrid collector

Similar to heliostats, dish concentrators can provide high concentration ratios but on smaller scales – up to 100s of kW. This makes them suitable for hybrid devices which are required to deliver high temperature output [102]. For example, Shou et al. [97] developed a spectrally splitting hybrid dish concentrating system which combines Si cells with a Stirling cycle to produce electricity (Figure 1.12c). A major shortcoming of such hybrid systems is the slow response of the engine to transient conditions. This can be addressed by replacing the engine with a thermoelectric generator (TEG) [31]. However, current TEGs have very low efficiencies compared to other electric generators such as a thermal engine.

Ju et al. [103] developed a method based on a 1-D heat transfer model to include the influence of concentration ratio and PV cell temperature in hybrid PV-TEG systems. Since the spectral response of TEG devices is relatively constant across the solar spectrum, the cut-off wavelength of such hybrid systems is driven by the PV cell module only [104]. Implementing TEG devices in solar receivers will be competitive when the figure-of-merit of TEG devices reaches about 3 [105].

The last hybrid collector method presented here uses a selective transmission/absorption medium (Figure 1.12d). In such systems, a filter (which can be a liquid or solid layer) which is transparent to wavelengths suitable for PV cells and highly absorbing in the rest of the spectrum is used to filter out the light. If a liquid is used, it can also act as the heat transfer fluid.

Chendo et al. [9] originally proposed the concept of selective absorption by heat transfer liquids for hybrid solar collectors in 1986. Recently, Zhao et al. [106] and Otanicar et al. [107] presented a numerical one-dimensional heat transfer and radiation model to optimise the optical properties (absorption characteristics) of a semitransparent heat transfer fluid suitable for a direct, selective absorbing hybrid solar collector.

A major shortcoming of such systems is the lack of available liquids with suitable optical properties. However, nano-fluid-based heat transfer liquids which incorporate nano-particles to achieve tunable optical properties have shown potential in addressing this issue [59, 108]. Such nano-fluids can be produced at low nano-particle volume fractions (e.g. much less than 0.1%), which indicates that it may be possible to design-low cost nano-fluid filters as discussed in section 1.2.6.

The possibility of employing spectral splitting in producing bio-fuel has been studied conceptually by Redwood et al. [109]. For this potential application, spectral splitting of sunlight can be implemented to overcome the problem of co-culturing different organisms which are sensitive to different wavelengths of sunlight. For example, spectral ranges suitable for green algae and purple bacteria are complementary. However, co-culturing these two organisms is not practical since photosynthesis by green algae captures CO_2 to produce oxygen, whereas

photosynthesis by purple bacteria is inhibited by oxygen. A beam splitter can divide the spectrum and direct each band to the separate containers of these bio-reactors to culture them in a more compact system.

1.5 Summary

Many exciting proof of concept designs have been demonstrated in recent years which have considerably raised the bar for high energy conversion efficiencies (regardless of manufacturability and cost). At the same time, recent work has focused on introducing designs which show promise as commercial products. In the future, it is expected that there will be many cases where the outcomes of these two groups can merge into successful commercial spectrally splitting solar collectors. In addition to the findings from the literature mentioned in the previous sections, some important tips in designing spectral splitting receivers have been acquired from the published literature and are listed here. Designing an efficient spectral splitting receiver requires these issues to be addressed:

- Concentrating devices such as dish and parabolic concentrators miss the diffuse component of global radiation. This incurs a significant loss which occurs especially in the short, high energy wavelengths.

- Non-ideal spectral splitting can cause some photons to be sent to the inappropriate receiver and reduce the total efficiency. The cost of fabricating quality splitters with tight optical tolerances should be balanced with the efficiency gain of the system.

- Dividing the spectrum into many bands can increase the splitting losses due to non-ideal behaviour of the filters.

- Concentrating spectral splitting systems create a distribution of incidence angles on the wave interference filter. This can result in deviated reflection/transmission characteristics.

- Reflection losses from the concentrating lenses could be minimised through efficient AR coatings.

- The number of transparent interfaces along optical paths should be minimised in order to keep the total Fresnel losses low.

- Short wavelength receivers are more sensitive to the daily and seasonal variation of spectrum. Hence the spectrum should be split in such a way that takes the time varying spectrum into account.

- Optimum integration of the concentrator, splitter, and receivers into an engineered package can result in a more compact, thinner receiver which could prove advantageous during manufacture and operation.

- Using direct selective absorption as a spectral splitting method in hybrid receivers could also help to avoid difficulties related to the manufacturing cost and operation. Initial research has identified some promising materials (solid and liquid) for this approach.

In any spectral splitting solar receiver, the splitter is the most critical component of the system. Most of these systems studied by other researchers are only PV systems. In PV systems, the splitter should be normally non-absorbing optical component because all the spectrum is to be utilised by different PV cells. However, for PV-T receivers this is different. In such systems, the spectral splitter component can be a selective absorbing part provided it is a part of the thermal absorber because the absorbed band can be delivered as a thermal output. This opens the opportunity to consider selective absorbing spectral splitters.
In this thesis, the applicability of direct absorption light filtering in a spectrally splitting hybrid PV-T receiver for linear solar concentrators such as parabolic troughs and Fresnel mirrors has been explored. Using this method can potentially result in lower cost of spectral beam splitting component and a more compact design for a practical product which minimises reflection losses and sensitivity of the system to the variations of the angle of incidence on the receiver. This is investigated and explained in more details in the next chapters.

Chapter 2

Thermal analysis of concentrating Si cells in spectral splitting PV-T receivers

---

The content of this chapter has been published as a conference proceedings in IHTC-15: Ahmad Mojiri, Cameron Stanley, Elizabeth Thomsen, Vernie Everett, Andrew Blakers, and Gary Rosengarten. "A heat transfer model for concentrating silicon solar cells in a spectrally splitting hybrid receiver". In: *Proceedings of the 15th International Heat Transfer Conference/IHTC-15*(Tokyo, Japan, vol.10, 2014)

In spectral splitting PV-T receivers, the heat load on the PV cells under elevated illumination levels is reduced by directing a specific band of light to them. However cell cooling is still required because the impinging light on the cells is converted into electricity with an efficiency less than 1. Managing the cell heat load and removing the heat from the cells is crucial for efficient operation of the cells. This can present a number of technical difficulties particularly for back contact solar cells, where the thermal pass-way is limited to the electrical contacts.

Back contact Si solar cells are optimised to achieve high conversion efficiencies under high illumination levels [110, 111]. These cells are modified Si cells that have low series resistances and shading losses to handle higher electrical current densities under concentrated light. This is achieved by locating both the p and n contacts of the cell at the non-illuminated side of the cell [110] (unlike conventional cells that usually have their n contacts at the front side of the cell). This eliminates the shading effect and allows for thicker contacts with reduced electrical resistance, which is desirable for the high electrical current generated in concentrating photovoltaic cells.

The cell contacts should be separately wired to a circuit board to collect the generated

electricity without shunting, whilst dissipating heat to a heat sink. This restricts the thermal flow through the solder bumps connecting the contacts to the board and adds complexity to the heat transfer process.
This problem is similar to heat transfer in electronic packages which has had a high level of interest in recent decades due to increased heat flux that needs to be dissipated [112]. It has been shown that voids within the structure of the solder material, created during the deposition of the solder layer, increases the thermal resistance of the structure and elevates the temperature of the chip (in electronic packages) [113] or the cell (in PV systems) [114].
This chapter presents a heat transfer analysis of back contact silicon cells under concentrated solar radiation with spectral beam splitting. For this purpose, the electrical behaviour of the cell was modelled using approximate well-known equations for PV cell performance as function of temperature and illumination level. The effect of the solder joints on the heat transmission has been included using the best available data within the literature. After providing an average model for the cell-sink configuration, the effect of spectral beam splitting on the temperature of the cell junction is presented to help design beam splitting PV-T systems.

2.1 Problem description

The schematic of the PV cell investigated in this research is presented in Figure 2.1a. This cell has been optimised for a concentrating spectrally splitting hybrid receiver by the Centre for Sustainable Energy Systems at the Australian National University. A layer of optical grade transparent silicone has been applied on the top side of the Si cell to optically match the cell to the surrounding and encapsulate it. The cover glass protects the silicone layer.
The heat generated in the cell junction is intended to be transported through the back of the cell to a heat sink that is located at the bottom of the steel layer. This heat can be absorbed and delivered as useful low grade thermal energy. For this reason it is highly desirable to minimise the heat loss from the top side of the cell to the ambient.
The thermal circuit used to model the heat transfer through this assembly is shown in Figure 2.1b. As discussed, two thermal pathways are considered, downwards to the heat sink and upwards to the ambient. The air gap in the downward direction is due to the presence of a gap created by the solder bumps. Some dimensions of the geometry have been slightly modified for the sake of simplification.
The spectral distribution and the concentration level of the incoming light was varied in the simulation. The generated heat in the cell is transported through the electrical pass-way to

the circuit board and then conducted to the heat sink wall. This heat sink can be a water cooled channel that removes heat by forced convection. Narrow thermal pass-ways and presence of voids in the solder bumps are expected to affect the heat transfer performance of the configuration.

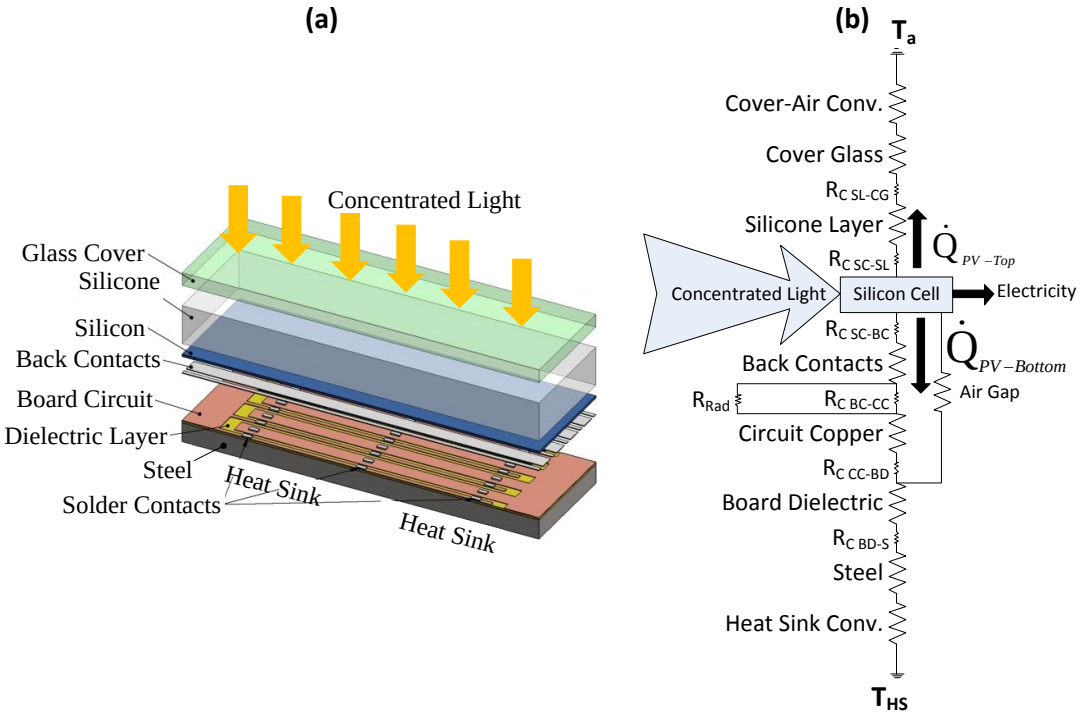

Fig. 2.1 (a) The exploded schematic of the back contact cell under concentrated light; (b) The thermal circuit of the same cell structure; R_C corresponds to contact resistance between two adjacent layers; SL: silicone layer, CG: cover glass, SC: solar cell, BC: back contact, CC: copper circuit, BD: board dielectric, S: steel

2.2 Modelling

The efficiency of a PV cell is a function of its temperature which in-turn is a function of the generated heat in the cell, and the heat transfer performance of the cell encapsulation system. This means that under illumination, the cell heats up, deteriorates in efficiency, and produces more heat. Hence the method for estimating the cell efficiency in such systems uses an iterative solution for estimating the cell temperature. A block diagram indicating this

iterative solution process is shown in Figure 2.2. The system considered here consists of an electrical model for the PV cell and a thermal circuit for the heat transfer process. The method used to model each of these subsystems is described in the following sections.

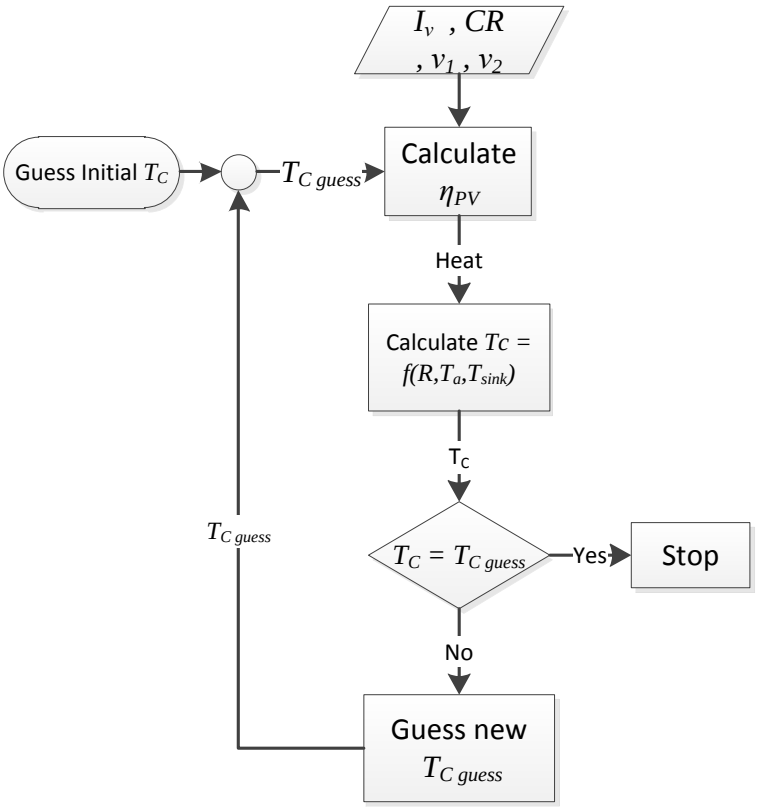

Fig. 2.2 Iterative solution procedure for determining the cell temperature, T_C; R: thermal resistance; T_a: ambient temperature; T_{sink}: heat sink temperature; Heat: the absorbed heat by the cell; I_v: spectral irradiation on the cell; CR: Concentration ratio; ν_1 and ν_2: the spectral band determined by the beam splitter.

2.2.1 PV model

The efficiency of concentrating silicon solar cells was modelled using well known relationships between their electrical properties such as open circuit voltage (V_{OC}), short circuit current density (J_{SC}), and the fill factor (FF). For a given cell, these parameters vary with

temperature, CR and spectral distribution of the light impinging upon the cell. Singh and Ravindra [115] have studied the performance of different types of solar cells as a function of temperature. Their equations were updated here to include the effect of light intensity and spectral selectivity. The effects of ohmic and optical losses, which alter the performance of solar cells, are not considered in these equations. The modelling method introduced here is not a unique method for calculating these parameters; however it is widely used by researchers to model the efficiency of single junction solar cells such as Si cells for the purpose of thermal analysis. The efficiency of a PV cell, η_{PV}, is given by:

$$\eta_{PV} = f_{(FF,\, I_{SC},\, V_{OC})} = \frac{J_{SC}\, V_{OC}\, FF}{E_{PV}}, \tag{2.1}$$

where E_{PV} is the radiative flux (W/m^2) striking the front surface of the cell. J_{SC} (A/m^2) is short circuit current density that varies linearly with concentration ratio and slightly increases with temperature due to the band-gap reduction of the cell. Hence, the short circuit current density at a certain temperature for a specific range of solar spectrum (ν_1 to ν_2) with concentration ratio of CR is

$$J_{SC(CR,\, T)}^{\nu_1-\nu_2} = q \int_{\nu_1}^{\nu_2} \phi_n\, CR\, u(\nu - \frac{E_{g(T)}}{h})\, \mathrm{d}\nu. \tag{2.2}$$

In this equation, q is the charge of electron, ν is frequency, ϕ_n is photon flux density at a specific ν, $E_{g(T)}$ is silicon band-gap energy as a function of temperature, h is Plank's constant, and $u(x)$ is unit step function. This step function term is for determining whether the photon energy is higher than the band-gap energy of the cell or not. This equation assumes that the external quantum efficiency is 100% at frequencies higher than the band-gap frequency. In practice this is not entirely true because optical and recombination losses affect the quantum efficiency of the cell.

The reduction in band-gap energy of a semiconductor as a function of temperature (T) can be approximated using the following Equation [116]:

$$E_g(T) = E_{g0} - \frac{\alpha T^2}{T + \beta} \tag{2.3}$$

In this equation, $E_g(T)$ is the band-gap energy of the semiconductor at temperature T, E_{g0} is its value at $T \approx 0K$; α, and β are constants. For silicon these constants are $1.557(eV)$, $7.021 \times 10^{-4}(V/K)$, and $1108(K)$ respectively for E_{g0}, α, and β. Higher cell temperature results in a slightly higher generated current because a wider spectral band of light will be collected by the cell (due to band-gap reduction). However, another important parameter that

significantly affects the efficiency of a solar cell is the reverse saturation current density, I_0, which increases with temperature. Its main effect is to reduce the open circuit voltage of the cell. Singh and Ravindra [115] have investigated different approximate correlations for I_0 and suggested that using the following equation gives the best agreement with experimental results for Si cells:

$$I_0(T) = Ae^{\frac{-E_g(T)}{KT}} \tag{2.4}$$

where A is $1.5 \times 10^9 (A/m^2)$ and k_B is Boltzmann's constant $(1.380 \times 10^{-23} (J/K)$. Having I_0 determined, the value of V_{OC} can be approximated as below to include the effect of temperature and concentration ratio:

$$V_{OC} = \frac{(nk_BT)}{q} \ln\left(\frac{J_L}{J_0} + 1\right) = \frac{nk_BT}{q} \ln\left(\frac{J_{SC(CR,T)}^{\nu_1 - \nu_2}}{J_0(T)} + 1\right) \tag{2.5}$$

In the above equation, J_L is the light generated current density that can be assumed to be approximately equal to the short circuit current density [115]. The last parameter required for calculating the efficiency of the cell is the fill factor. Equation 2.6 shows the empirical equation for FF where the shunt and series resistances effects are negligible proposed by Green [117]:

$$FF = \frac{v_{OC} - \ln(v_{OC} + 0.72)}{v_{OC} + 1} \tag{2.6}$$

In this equation, v_{OC} is normalised open circuit voltage defined in Equation 2.7:

$$v_{OC} = \frac{V_{OC}}{(nk_BT)/q} \tag{2.7}$$

Unlike front contact cells where shading effects limit the size of the contacts, in back contact solar cells a large portion of the back side of the cell can be covered by metallic contacts to minimise the series resistance of the cell [111]. However, shunting effects can be compromised by the quality of the ohmic contacts that is driven by the doping level. Since the effect of shunt resistance is more significant for low currents it will be negligible for this case because the cells are being considered under concentrated illumination (i.e. high currents). The equations listed above have been used to develop a MATLAB code which allows the efficiency of a Si cell to be estimated for different CRs, spectral bands, and temperatures. The model also determines the quantity of heat generated in the cell that needs to be dissipated to a heat sink.

2.2.2 Heat transfer model

The thermal circuit considered for this model is based on conductive and radiative heat transfer. The air gap in the cell structure is of the order of 0.1mm thick, which keeps the Rayleigh number very small and indicates that the heat transfer is dominated by conduction rather than natural convection. The radiative heat transfer coefficient between the back contacts and the circuit board has been calculated using radiation equation between two parallel large plates (since the gap is small compared to the contacts width). For the sake of simplicity, the radiative heat transfer resistance was linearised as below:

$$R_{RAD} = \frac{2-\varepsilon}{4A\sigma\varepsilon T^3} \tag{2.8}$$

In this equation, ε is the emissivity of the contacts and the circuit board (both made of copper with infra-red emissivity of 0.15), A is the area of the contacts minus the soldered area, σ is Stephan-Boltzmann constant, and T is the arithmetic mean temperature of the circuit board and the contacts surface. Since the cell temperature is to be kept below 100°C and the emissivity of copper in infra-red is low this radiative heat transfer is significantly smaller than the conduction heat transfer through the solder joints. Despite this fact, the radiative heat transfer was considered in the thermal modelling of the cell structure.

Near field radiative heat transfer can increase the heat transfer coefficient by several orders of magnitude. Since the temperature of the surfaces is in the range of 25-100°C and the gap size is about 100 μm, radiative heat transfer process is dominated by the propagating radiation rather than the evanescent near field waves [118].

The effect of potential porous voids in the solder layer plays a key role in the thermal resistance of the system. Baricordi et al. [114] studied the effect of solder layer void content on the heat transfer and electrical performance of concentrating silicon cells. The structure of the cell that they investigated was a double face contacted cell (DFC cell). Unlike back contact cells, in DFC cells the whole back area of the cell can be used for soldering to improve the heat transfer performance. Their analysis showed that a solder void content of 36.6% resulted in an 8.8% increase in the thermal resistance of the system. Despite this increase, the temperature distribution across the cell surface didn't show any significant variation (less than 1K) under 100 suns concentration.

Vaillon et al. [119] presented a coupled electrical and thermal analysis for Si cells. They concluded that the temperature gradient across the thickness of Si cells is insignificant (e.g. less than 0.01K) which is mainly due to the relatively low thickness and high thermal conductivity of Si cells. Considering the above explanations, temperature gradients in the cells have been neglected in this model and a uniform cell temperature has been assumed.

Table 2.1 The values considered in the heat transfer model; the parameters have been defined in the previous sections and figures

Element	Area ($\times 10^{-6} m^2$)	Thickness ($\times 10^{-3} m$)	Thermal Conductivity (W/mK)
Cover Glass	228.25	2	1.05
$R_{C\ SL-CG}$	228.25	(-)	Variable
Silicone Encapsulant	228.25	10	0.21
$R_{C\ SC-SL}$	228.25	(-)	Variable
$R_{C\ SC-BC}$	162.25	(-)	Variable
Back Contact	162.25	0.042	400
Air Gap	228.25-Solder Area	0.177	0.024
Solder	Variable	0.1	35
Circuit Copper	176.76	0.035	401
$R_{C\ CC-BD}$	176.76	(-)	Variable
Board Dielectric	228.25	0.15	3
$R_{C\ BD-S}$	228.25	(-)	Variable
Steel	228.25	1.5	43

The first step of the process was to investigate the temperature rise of the cell junction due to only its internal thermal circuit. This means that the external heat removal performance (convective heat transfer from the bottom and radiative/convective heat loss from the top faces) has not been considered. This solution provides useful information on the importance of the solder layer properties. Following this, an average value of convective heat transfer coefficient (1000 W/m^2K) is added to the heat sink side of the model (bottom of the steel layer) to estimate the total temperature rise of the cell in a real world condition. This model has been used to investigate the effect of spectral splitting. Material properties and geometric dimensions of the heat transfer model are presented in Table 2.1.

Table 2.2 Thermal conductivity of typical Pb-free solders [13]

Solder Composition	Thermal Conductivity (W/mK)	Temperature (°C)
Bi-42Sn	21	85
In-48Sn	34	85
Sn-3.5Ag	33	85
Sn-3.5Ag	54.3	24
Sn-3.5Ag-1Zn	33	85
Sn-20In-2.8Ag	53.5	30

The thermal conductivity of a number of lead free solders is presented in Table 2.2 . The typical value at room temperature is about 55 (W/mK) however this value decreases for elevated temperatures. A value of 30 (W/mK) was used in this study as the typical value of

the thermal conductivity at 85°C. This represents the worst case scenario in which the cell is operating at high temperatures i.e. above 85°C.

Effect of solder voids

The heat transfer performance of solder layers in electronic packages depends significantly on their void content and void geometry [113, 120]. Minimising the void formation is a considerable challenge, and completely removing them is extremely difficult. Vacuum soldering can help to reduce the void content significantly at the cost of increased soldering process complexity.
Diehm et al. [121] suggested that starting the soldering process in excessive pressure and finishing it in atmospheric pressure can take advantage of the same pressure difference as applying a vacuum but at a lower cost. In most practical applications, voids are the inevitable left overs of the soldering process. Tiny voids can propagate like cracks in the solder structure and create large contiguous voids. One reason for void propagation is fatigue due to thermal cycling which is particularly relevant for concentrating solar cells.
At present, the heat transfer characteristics of voids in solder have not been thoroughly investigated and remain poorly understood. The work done by Fleischer et al. [113] is one of the few studies in this field. They showed that the trend of the solder thermal resistance variation of a certain chip package considered in their study is a function of the void geometry. Increasing the total void content to 73% was shown to increase the thermal resistance of the whole system linearly by 30% for random small void geometries and exponentially by 200% for contiguous large void geometries. Since the presence of contiguous voids raises the resistance more dramatically [113, 120], this case has been considered as the worst case scenario in this study. The expression for solder resistance as a function of void content has been determined by slight modification of those presented by Fleischer et al. [113], as below:

$$R_s(V) = R_S(0) \times 41e^{1.427V} - 40 \tag{2.9}$$

In the above equations, $R_s(V)$, $R_s(0)$ are solder thermal resistance with and without void respectively, and V is the void content. The value of $R_s(0)$ is calculated as below:

$$R_s(0) = \frac{t}{kA} \tag{2.10}$$

Here, t is the average thickness of the solder layer, k is the thermal conductivity of the solder material without voids, and A is the solder area. In this chapter, the solder area fraction is

defined as the ratio of the solder area to the back contacts area which it cannot exceed. This parameter determines how much of the back contact area is covered by the solder layer. Assuming that contact resistances arise due to the tiny voids at the interface of two materials, no contact resistance is being considered for the solder without void. The thickness of the solder remains constant but by changing the soldered area, the sensitivity of the total thermal resistance with respect to solder geometry and void contents is studied.

Finite element steady-state thermal model

To complement the MATLAB model described above, a steady-state thermal analysis was conducted using commercial multi-physics code ANSYS, version 14.5. The geometry model was that of the concentrating cell structure presented in Figure 2.1a. Material properties and boundary conditions matched those within the heat transfer model described above.
Outputs from the model were used to verify the veracity of the 1D assumption of the heat transfer model described above. Under concentration ratio of 100 suns the temperature variation within the Si cell was investigated for various solder area fractions. The effect of solder void content on the heat transfer was explored by defining an equivalent contact resistance at the interface of the solder bumps and the back contacts, and the solder bumps and the circuit copper.
Geometrical symmetry in the lateral direction meant that only half the n and p back contacts were required to be modelled. On the left side of the cell (which is the edge of the cell and a non-symmetry plane), an adiabatic thermal boundary condition was used, as heat transfer from one cell to the adjacent cell in a linear cell packaging is not expected. The external surface of the cover glass was given a heat transfer coefficient of $3(W/m^2K)$ and the ambient conditions were modelled as 25°C. At the base of the steel layer a constant sink temperature of 25°C (infinite heat sink) was applied. The thermal contact resistance of $79,527(W/m^2K)$ was applied to the top and bottom faces of the solder bumps to represent the resistance due to the presence of solder voids, assumed to occupy 25% of the solder by volume.
Figure 2.3a shows contours of temperature within the back contact cell structure for a solar concentration of 100 suns. The pass-way of heat from the cell to the dielectric board, and the influence of the air gaps between the back contacts can be seen in Figure 2.3b. Under these conditions results demonstrate a sink-cell temperature of 13.5°C. Figure 2.3c shows the contours of temperature within the Si cell and reveals temperature non-uniformities of 0.3°C throughout the cross-section.

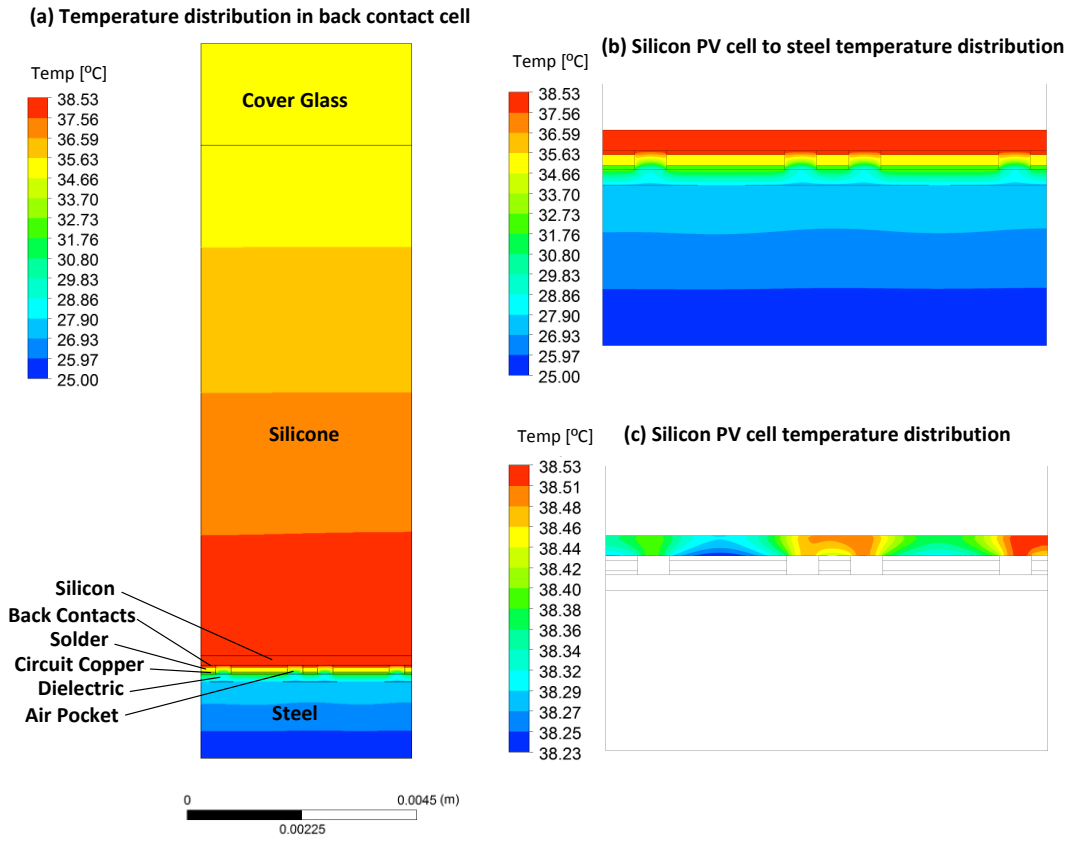

Fig. 2.3 Contours of temperature through the back contact cell under 100 suns concentration for (a) the entire geometry, (b) the Si cell and elements below and (c) within the Si cell. A thermal contact resistance of the voided solder layer (25% by volume) of 79,527 (W/m^2K) was applied.

These results illustrate the largely 1-dimensional nature of the heat transfer from the Si layer to the sink. Given the very minimal temperature distribution within Si layer the simplifying assumption of 1-dimensional heat transfer for the development of the MATLAB heat transfer model appears justified.

2.3 Modelling results

Initially the sensitivity of the cell temperature to the contact resistances between different components in the absence of solder voids was investigated. The thermal contact resistance between surfaces is a function of surface finish, the coupling pressure, and the fluid trapped

in the interface layer. Here, it has been assumed that there is no thermal contact resistance between the back contacts and the cell ($R_{C\ SC-BC} = 0$) since the contacts are deposited on the cell, which helps to achieve a continuous interface between these two materials.
$R_{C\ BC-CC}$ is modelled as a part of the voided solder resistance as explained in the previous section. The sensitivity of the system thermal resistance with respect to $R_{C\ CC-BD}$ and $R_{C\ BD-S}$ is shown in Figure 2.4. Noting that the contact area corresponding to these two resistances are different, it can be seen that the total resistance of the cell structure increases linearly with contact resistances. Assuming that the contact resistance per unit area, $r_C(Km^2/W)$, at copper-dielectric and steel-dielectric interfaces are identical (the red line denoted by $R_{C\ BD-S}$ and $R_{C\ CC-BD}$, we see that cell-sink temperature difference increases at a rate of:

$$\frac{dT_{Cell-Sink}}{dr_c} = 1.53 \times 10^5 (W/m^2) \tag{2.11}$$

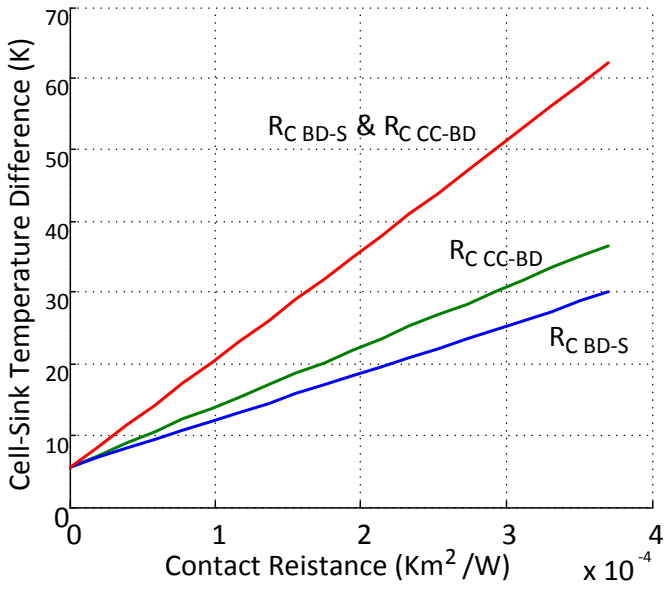

Fig. 2.4 The variation of cell-to-heat-sink temperature difference with respect to dielectric layer contact resistances $CR = 100$; solder area fraction = 50%. In the combined case (red line), the contact resistance per unit area at both sides of the dielectric layer are assumed to be the same.

The graph in Figure 2.4 doesn't include the contact thermal resistances of the solder layer that has been shown to be a function of void content. The effect of the solder voids on the cell performance, measured by cell – sink temperature difference, total resistance, heat generated

and PV efficiency, is presented in Figure 2.5. In this analysis the CR has been assumed to be 100 suns, and no other contact resistances between the layers in Figure 2.1 have been included to investigate just the effect of voids. As expected, the sensitivity of all parameters to the degree of void content increases as the solder area fraction is reduced.

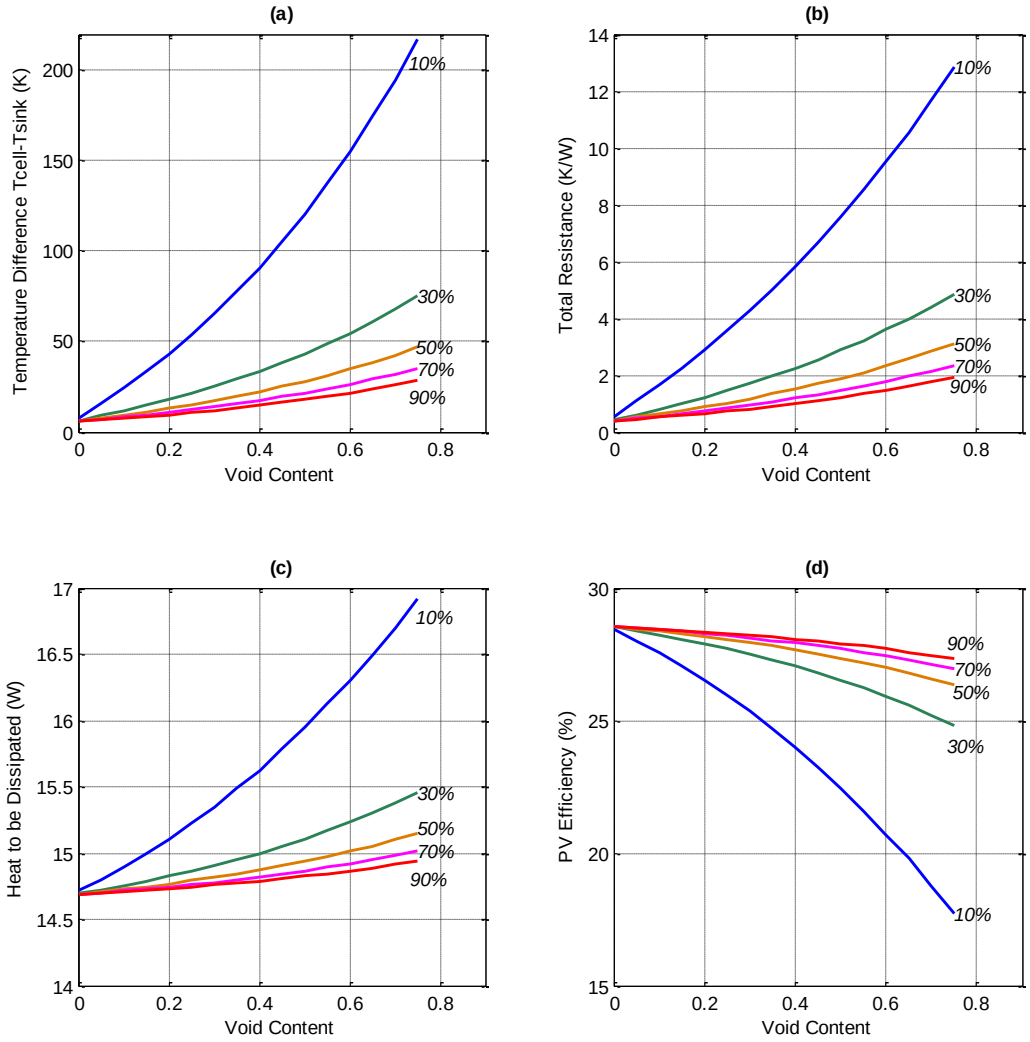

Fig. 2.5 The variation of different parameters of the model as function of void content. Different lines in each figure represents different solder area fraction (i.e. 10%, 30%, 50%, 70%, 90%); CR: 100 suns

Figure 2.5a shows the temperature difference between the cell junction and the lower face of the steel layer which is in contact with the heat sink. The temperature of this face has

been assumed to be 25°C. Figure 2.5b shows the increase in total thermal resistance of the network with increase in void content. The trend shows the exponential relationship of Equation 2.9. The amount of heat to be dissipated in Figure 2.5c slightly increases because the conversion efficiency of the PV cell, shown in Figure 2.5d, decreases when the cell temperature increases.

In most electronic applications, the maximum allowed void content is restricted to 25%. At this level the cell-heat sink temperature increases to 54°C under 100 suns of concentration (10% solder area fraction). Relevant values for this void content have been tabulated in Table 2.3.

Table 2.3 The variation of different model parameters considering a void content of 25% and CR of 100 suns

Solder area fraction	Tcell−Tsink (°C)	Total resistance (K/W)	Heat to be dissipated (W)	PV cell efficiency (%)
10%	54	3.55	15.22	25.95
30%	21.5	1.45	14.9	27.71
50%	15	1.02	14.8	28.05
70%	12.5	0.84	14.8	28.2
90%	10.75	0.75	14.7	28.3

As an average model of a cell structure, the performance of the configuration outlined below has been studied at different CRs and heat sink convection coefficients. Royne et al. [54] provided a review on different cooling mechanisms of concentrating cells, reporting that the typical convective heat transfer resistance of water channel cooling systems for concentrated PV is in the range of 2.3×10^{-4} to $1 \times 10^{-3} (Km^2/W)$. Again the highest value has been considered here as the worst case scenario. All other dimensional parameters are as mentioned in the previous sections.

The effect of spectral beam splitting has also been considered. An ideal band pass filter has been assumed to split the original radiation and direct the wavelengths between λ_1 and λ_2 to Si cells. λ_2 is determined by the band-gap of the cell. As discussed previously, the wavelength corresponding to the band-gap increases with temperature. Such variation has been presented in Figure 2.6. Since the aim of applying spectral beam splitting and the cooling channel is to keep the cells at temperatures below 60°C, λ_2 is set at 1,125nm (see Figure 2.6). It should be noted that the spectral response of real Si cells drops before this wavelength because Si is an indirect band-gap semiconductor without an absorption edge as sharp as direct band-gap semiconductors. However, for the sake of simplicity this fact has been ignored, without significant changes in the results. This cut-off wavelength prevents

wavelengths longer than λ_{Eg}, that don't generate electron-hole pairs, from reaching the cell.

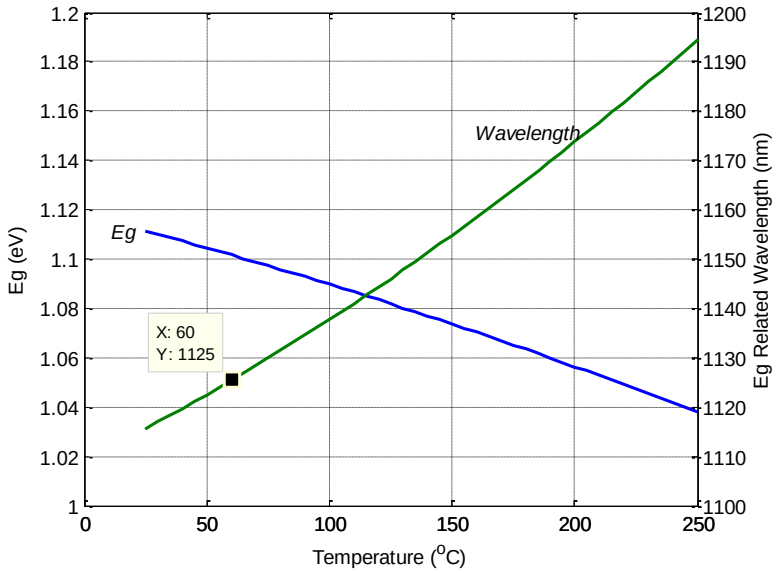

Fig. 2.6 The variation of Si band-gap as a function of temperature calculated by Equation 2.3

The lower cut-off wavelength, λ_1 , has been kept as a variable to examine the effect of spectral band width on the cell parameters. The influence of this parameter on a number of cell performance parameters is presented in Figure 2.7. The transmitted spectral band directed to the cell is shown in Figure 2.7a. Figure 2.7b shows the variation in cell temperature as a function of cut-off wavelength, λ_1 for various values of CR. It can be seen that the effect of spectral beam splitting is more considerable in higher CRs. For CRs of up to 40 suns, the cell temperature remains under 60°C for all values of λ_1; whereas for CRs of 60, 80, and 100 suns, λ_1 should be 500nm, 620nm, 680nm respectively in order to maintain a cell temperature below 60°C.

To limit the cell maximum operating temperature, different cut-off wavelengths (λ_1) are required for different concentration ratios. This value also depends on the convection coefficient of the heat sink and the internal structure of the cell mounting which is driven by the void content and the geometrical dimensions.The conversion efficiency of the cell as a function of λ_1 and CR has been presented in Figure 2.7c. This conversion efficiency is based on the radiation energy impinging upon the cell i.e. after being filtered by the spectral splitter.

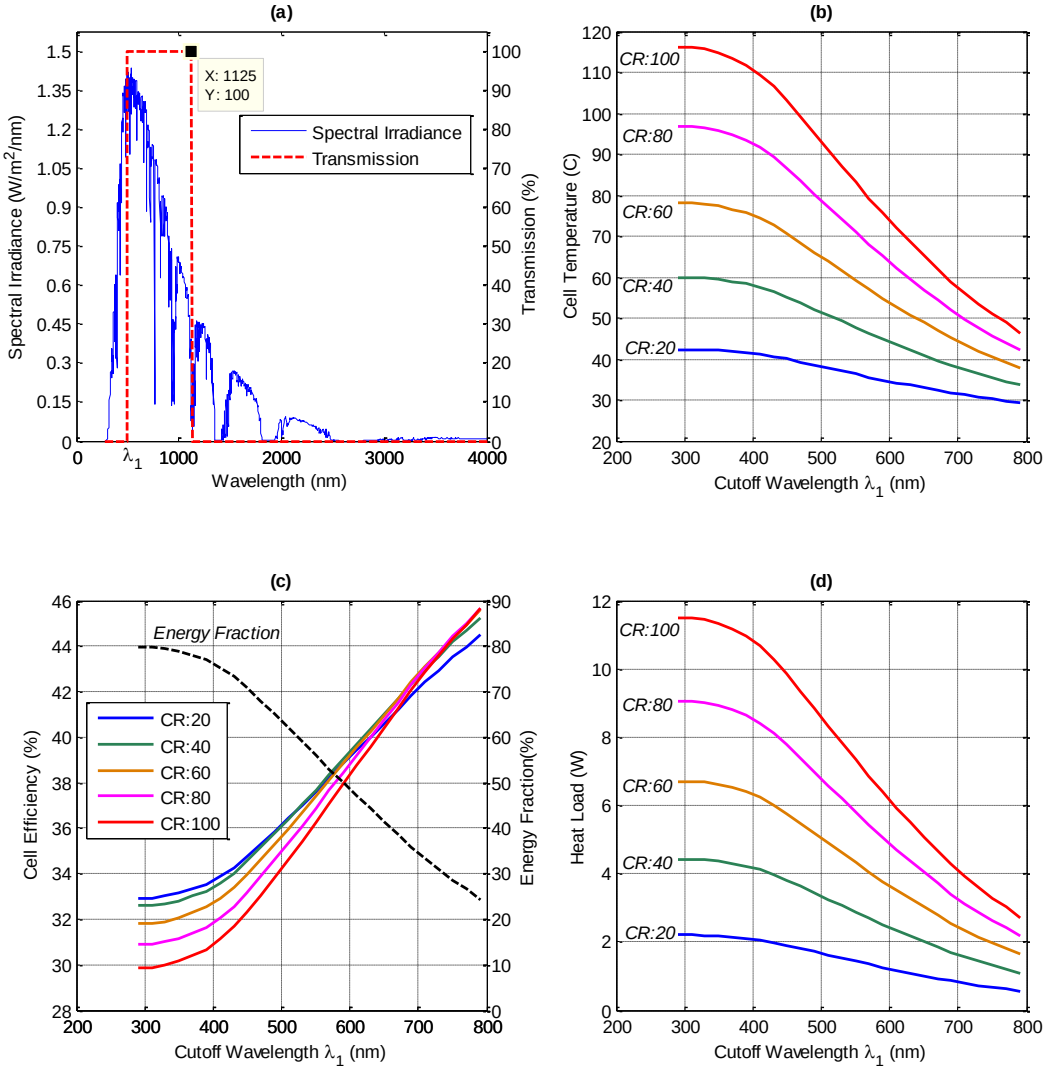

Fig. 2.7 The variation of different cell parameters vs. spectral band width for different CRs; $V = 25\%$, heat sink convection coefficient = $1000W/m^2$; $T_{heatsink} = 25°$ C, cell area $= 8.3 \times 27.5mm^2$ (a) The spectral irradiation corresponds to AM 1.5 direct beam [122]; the right edge of the band (λ_2) is fixed at the band-gap related wavelength of the cell; (b) Cell temperature as a function of λ_1; (c) Cell electrical conversion efficiency as a function of λ_1; (d) The heat generated on the cell that must be dissipated from the cell. Energy Fraction: the fraction of the total available energy that is directed to the PV cell by the splitter

The power is determined by λ_1 as is calculated using Equation 2.1. In this equation, E_{PV} is calculated as shown in Equation 2.12:

$$E_{PV} = \int_{\lambda_1}^{1125} A\, I_\lambda \, \mathrm{d}\lambda \tag{2.12}$$

Here, A is the cell area and I_λ is the spectral irradiation of direct and circum-solar components of the sunlight. The black dashed line shows the ratio of the flux lying in $\lambda_1 - 1125$nm band to the total flux of the whole solar spectrum. So the total electrical conversion efficiency of the cell with respect to the whole spectrum is equal to the product of the cell efficiency and the energy fraction in Figure 2.7c.
For small values of λ_1, the effect of temperature is significant on the cell efficiency. Hence there are distinguishable differences between the lines with different CRs; the cells with lower CR have higher conversion efficiencies. By increasing λ_1, i.e. narrowing the spectral band, the heat load on the cell reduces (Figure 2.7d) followed by the cell's operating temperature. Gradually, the concentration ratio dominates the effect of temperature increasing the efficiency of the cells. At λ_1 just below 700nm, the efficiencies of the cells with higher CRs exceed the low concentration ratio cells' efficiencies.

Table 2.4 The minimum value of λ_1 to maintain the cell operating temperature below 40, 60, 80°C for different concentration ratios; void content: 25%, heat sink convection coefficient: 1000 (W/m^2); $T_{heatsink}$: 25°C. Note: SS = spectral splitting.

Maximum Cell Temperature (°C)	CR (Suns)	Cut-off Wavelength λ_1 (nm)
40	20	450
	40	670
	60	750
	80	> 800
	100	> 800
60	20	SS not required
	40	SS not required
	60	550
	80	630
	100	670
80	20	SS not required
	40	SS not required
	60	SS not required
	80	490
	100	570

For CRs of higher than 80 suns, and λ_1 smaller than 800nm, T_{cell} remains always above 40°C.

On the other hand, for CRs of up to 40 and 60, T_{cell} remains always below 60°C and 80°C respectively. However the convection coefficient of the heat sink and the structural resistance of the cell mounting will change these values.

2.4 Summary

It has been shown that the void content in the solder area in addition to the convection heat transfer coefficient of the heat sink can have a significant effect on the operating temperature of the cell junction and reduce its efficiency. Assuming a certain value of convection heat transfer coefficient for the heat sink, the cell temperature can exceed the maximum limit at high enough concentration ratios. For such cases, spectral beam splitting can be applied to reduce the heat load on the cell and maintain the cell temperature within the acceptable range, while allowing higher temperature thermal harvesting.
This chapter presented a design consideration for sizing the cell heat sink and determining the cut-off wavelengths of the spectral splitter from thermal management point of view. Such analysis should be carried out for PV-T spectral splitting systems to assure that the heat generated on the cells is not affecting the overall performance of the systems. In next sections, the system is investigated from optical performance point of view. Chapter 3 introduces a method to measure the spatial distribution of light at the focal region of solar concentrators which is essential to geometrically size the spectral splitting receiver.

Chapter 3

Radiometry on flat surfaces for receiver sizing

The content of this chapter has been published as a journal article:
Ahmad Mojiri, Cameron Stanley, and Gary Rosengarten. “Close range radiometry for quantifying the spatial distribution of illumination on flat surfaces”. In: *Solar Energy 122*(2015): 429-439

Sizing the receiver is an important step in designing concentrating solar devices. The size of the receiver should be carefully specified to prevent missing concentrated light. On the other hand, over-sizing the receiver can add extra cost, shading, higher heat loss in thermal systems and decreases the concentration ratio. Hence there is a need for accurate methods for measuring the illumination profile. So far, different methods such as radiometric flux mapping and light scanning have been used to measure the irradiance. A combination of photo-grammetry and ray tracing is also used to predict the illumination profile of concentrators [123].
In this chapter, the necessary tools for measuring the spatial distribution of the irradiance (non-dimensional) which is the relative magnitude of the irradiance over a flat target surface is introduced. In order to measure the absolute value of irradiance (W/m^2) on the surface, one should use a complimentary method such as radiometry of a known irradiance profile or calorimetry on the target to correlate the relative irradiance distribution values to the absolute irradiance values.
Radiometric flux mapping uses photographic pixelated images to extract the illumination pattern on surfaces. The advantage of this method is that it requires simple hardware and allows the irradiance distribution to be determined in a more straight-forward manner compared to photo-grammetry-ray tracing and light scanning techniques. In this method the flux pattern

on a diffuse reflector target is photographed using a digital camera. The grey-scale value of the image pixels is associated with the irradiance of light impinging upon the corresponding points on the reflector.
Rectification to correct for optical and perspective distortions allows the distribution of the irradiance to be mapped from the image to the real world coordinates system and vice versa. However, the accuracy of this method is dependent on proper calibration of the camera set-up. A diffuse reflector as the target is necessary to record the illumination data, but a Lambertian diffuse reflector can simplify the data analysis significantly.
Radiometric flux mapping has been developed and tested for long range applications where either the camera is far away from the target such as solar power towers or the spot size is small such as dish concentrators. Blackmon [124] outlined the design and operational characteristics of a long range radiometry system for monitoring the performance of heliostat mirrors. He used a video camera to capture an analogue image which was digitised in a post-processing stage. Similar method has been used for flux measurement of dish concentrators [125, 126], parabolic troughs [127–129], solar simulators [130], and solar furnaces [131, 132]. In order to circumvent the excessive heat at high levels of illumination, such as in solar furnaces, Schubnell et al. [133] used lunar light to illuminate the target and study the illumination profile of a solar furnace.
In these cases, due to the long distance of the camera from the target, the effect of camera objective such as the $\cos^4$ law may be negligible depending on the spot size, which simplifies the required calculations and technical challenges. However in some cases, due to spatial constraints or a requirement for higher resolution, close range radiometry measurements are desirable.
Here, a photographic radiometry method is presented to perform close range flux mapping where the spatial size of the illuminated area is in the order of the camera-target distance. This requires accommodation for the effect of lens distortion and a precise method to extract the geometrical configuration of the set-up. The lens distortion effects are addressed by the radiometry theory that is explained in the next section. The required radiometry equations are reconsidered and a camera calibration method is applied to extract the necessary geometrical data for close range radiometry.

3.1 Radiometry theory

A digital camera sensor, CMOS or CCD type, comprises of a dense array of tiny pixels that convert the radiant energy (J) on each pixel into a digital number in a grey-scale image. In

the case of an RGB camera, the image should be converted into a grey-scale image in order to account for all radiant energy on a pixel over the total spectral band of the sensor sensitivity. The energy received by a pixel is proportional to the product of the radiant flux (W) and the exposure time (s). Since the exposure time for all pixels is almost the same (i.e. ignoring the transient motion of the physical shutter in front of the sensor) the sensor pixel response can be considered as a function of the radiant flux as $PV = \psi(F_{px})$, where, PV is the pixel grey value in a grey-scale digital image and F_{px} is the radiant flux (W) on the pixel. By comparing the PV corresponding to different pixels on the image, the distribution of the radiant flux on the camera sensor can be extracted. The aim of radiometry is transforming this distribution to the irradiance distribution on the real surface in the object space.

3.1.1 Linearity of the camera sensor

In order to infer the radiant flux on the pixelated sensor of the camera, the response of the camera sensor with respect to it must be known. If the sensor exhibits a linear response then the relative magnitude of grey-scale values reported by two arbitrary pixels will be equal to the relative magnitude of the radiant flux reaching the pixels. If the response is not linear, the corresponding radiant flux should be modified in accordance with the sensor response function. For a non-linear sensor with a response function of ψ:

$$\frac{F_{px_1}}{F_{px_2}} = \frac{\psi^{-1}(PV_1)}{\psi^{-1}(PV_2)} \tag{3.1}$$

where, subscripts 1 and 2 correspond to two arbitrary pixels (px) and ψ^{-1} is the inverse of ψ. For a linear sensor, the relation is simpler:

$$\frac{F_{px_1}}{F_{px_2}} = \frac{PV_1}{PV_2} \tag{3.2}$$

The next step to extract the irradiance distribution on the target of the camera (the diffuse reflector) is correlating the value of F on the pixel to the value of radiance, $B(W/m^2/sr)$, on the reflector. Radiometry employs imaging optics principles to map the radiant flux of the object space to the radiant flux of the image space in an imaging optical configuration such as a camera lens system.

3.1.2 Radiometry in reflection mode

To analyse the distribution of light in the object space, either a diffuse reflector (in reflection method) or a diffuse transparent medium (in transmission method) can be employed. In this work, the former method was used, however the fundamentals of both methods are similar [134]. The general principles of geometrical radiometry can be found in various imaging optics text books, e.g. [135], and for the sake of brevity will not be repeated here. In this section, the necessary equations for radiometry using a digital camera for reflection mode are introduced. In such a case, the size of the illumination spot is significant compared to the camera-target distance i.e. close range radiometry.
In such an experiment, the data analysis process will be significantly simplified if a Lambertian diffuse reflector is located at the focal region of the concentrator to capture the flux image. The reflected radiant intensity (W/sr) of a small element on such reflectors reduces by the factor of $\cos(\theta)$, the cosine of the angle between the surface normal and the reflection direction at the element. However the radiance, B, leaving the surface is constant in all directions. Having the reflected radiance form the surface element, the impinging irradiance (W/m^2) upon the element can be calculated.

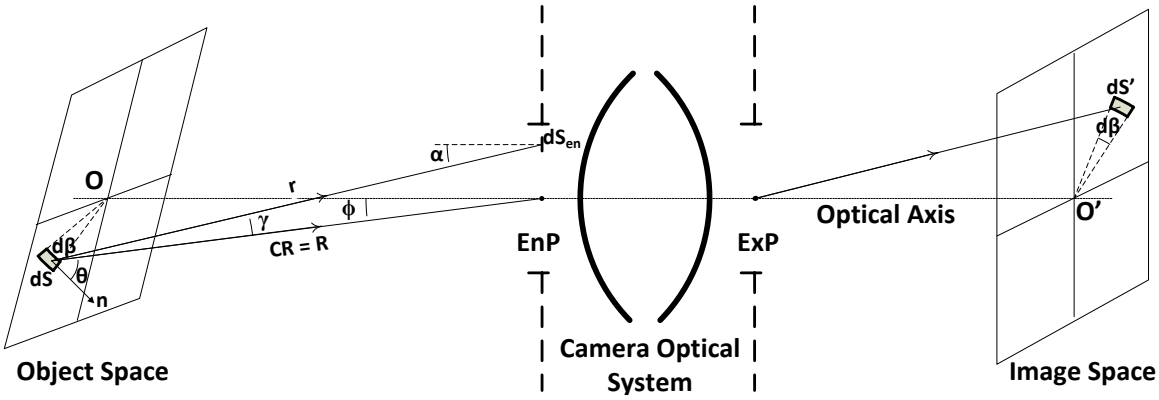

Fig. 3.1 The geometrical configuration of the imaging optics in a lens system; the object has a flat surface which is not necessarily perpendicular to the optical axis; the image plane is perpendicular to the optical axis; aperture stop is inside the camera optical system. *CR* is the chief ray.

Clifford and Khalsa [136] introduced the corresponding equations for the irradiance on the CCD pixel of a camera targeting a diffuse reflector, however they assumed the angle between the camera axis and the object-camera line, R in Figure 3.1, is negligible i.e. long range radiometry. This is true unless the size of the flux region to be mapped is significant compared to R which for example is the case in mapping the irradiance in parabolic troughs

from a short distance. In the geometric radiometry formulation introduced here, the size of the spot has been considered to be comparable with the camera-target distance. So ϕ, see Figure 3.1, is not negligible.
The surface element dS on the object sees the surface element dS_{en} on the entrance pupil through a solid angle subtended by dS_{en} at a distance of R and angle of α,

$$\mathrm{d}\Omega = \frac{\cos(\alpha)\mathrm{d}S_{en}}{r^2} \tag{3.3}$$

The radiant flux leaving dS in the object space and impinging upon dS_{en} is,

$$\mathrm{d}F = B\cos(\theta+\gamma)\,\mathrm{d}S\,\mathrm{d}\Omega = B\cos(\theta+\gamma)\cos(\alpha)\mathrm{d}S\frac{\mathrm{d}S_{en}}{r^2} \tag{3.4}$$

From Figure 3.1, $\alpha = \phi + \gamma$. The size of the entrance pupil is very small compared to r. Hence it can be assumed that γ is negligible and $r = R$; this is not true in microscopic imaging where the object is very close to the pupil but for cameras is a reasonable assumption. Hence by integrating Equation 3.4 over the whole area of the entrance pupil, A_{EnP} (EnP has been denoted in Figure 3.1), the total radiant flux received from dS can be calculated as:

$$F = \int_{A_{EnP}} B\cos(\theta)\cos(\phi)\mathrm{d}S\frac{\mathrm{d}S_{en}}{R^2} \tag{3.5}$$

A set of losses on the camera optical system such as reflection, absorption, and vignetting can affect the amount of light transmitting through the system and absorbed by the sensor. At this stage it is assumed that such losses are not significant and F is entirely received by the image element dS'. dS' is correlated to dS through the magnification value M [135] and the tilt angle θ. This can be expressed as:

$$M = \frac{f}{R\cos(\phi) - f} \tag{3.6}$$

$$\mathrm{d}S' = M^2\cos(\theta)\mathrm{d}S \tag{3.7}$$

In Equation 3.6, f is the focal length of the optical system. These two equations mean that the further the element, the smaller the image will be i.e. the number of pixels in dS' will be less. On the other hand by tilting the element, increasing θ, dS' will decrease and when θ is 90°, its image on the image plane will disappear. By integrating Equation 3.5 over the entrance pupil, the total radiant flux coming from dS into the camera and consequently

absorbed by the sensor can be calculated as:

$$F = B\cos(\theta)\cos(\phi)\mathrm{d}S\frac{A_{EnP}}{R^2} \tag{3.8}$$

This is similar to the “cosine fourth law" in optical radiometry. Note that two cosine terms are $\cos(\theta)$ and $\cos(\phi)$, and there are two extra cosine terms implicit in R^2 if the projection of the element-camera distance on the optical axis instead of R is used. Based on the discussion in the previous section, for a linear response sensor, the total radiant flux on $\mathrm{d}S'$ can be correlated to the pixel values as:

$$F \propto \sum_{\mathrm{d}s'} PV_i \tag{3.9}$$

which means that the total radiant flux on $\mathrm{d}S'$ is linearly proportional to the sum of the response values of the pixels on $\mathrm{d}S'$. Note that

1. by doubling R and keeping other parameters constant in Equation 3.8, the radiant flux reaching $\mathrm{d}S'$ will decrease by R^2; on the other hand for $R \gg f$, $M \approx \frac{f}{R\cos\phi}$ which decreases by R. This means that S' and alternatively the number of pixels in it will decrease by R^2 meaning that the mean pixel value on $\mathrm{d}S'$ will remain invariant. This is an important characteristic of imaging optics that the radiance of the in-focus image is invariant with the object distance.

2. by tilting the surface element i.e. increasing θ in a Lambertian surface, the radiant flux F reaching $\mathrm{d}S'$ decreases by $\cos(\theta)$. On the other hand $\mathrm{d}S'$ and alternatively the number of pixels in it decreases by $\cos(\theta)$ which means that the mean pixel value on $\mathrm{d}S'$ will remain invariant. This is the second important characteristic that the brightness of the image of a Lamberitan surface is invariant with the view angle.

By combining equations 3.8 and 3.9,

$$B \propto \frac{R^2}{A_{EnP}\cos(\theta)\cos(\phi)\mathrm{d}S}\sum_{\mathrm{d}S'} PV_i \tag{3.10}$$

For two equal element areas on the object surface,

$$\frac{B_1}{B_2} \propto \frac{R_1^2\cos(\theta_2)\cos(\phi_2)\sum_{\mathrm{d}S'_1} PV_i}{R_2^2\cos(\theta_1)\cos(\phi_1)\sum_{\mathrm{d}S'_2} PV_i} \tag{3.11}$$

Note that A_{EnP} and $\mathrm{d}S$ are the same for the two elements. In order to complete this method, B must be correlated to the impinging irradiance, $I(W/m^2)$, on the surface. For a Lambertian

reflector, this can be carried out by an energy balance between the irradiance on and radiance of the surface,

$$\rho I = \int_0^{2\pi} \int_0^{\pi/2} B\cos(\omega)\sin(\omega)\mathrm{d}\omega\mathrm{d}\phi \tag{3.12}$$

$$\Rightarrow B = \frac{\rho I}{\pi} \tag{3.13}$$

where, I is the irradiance (W/m^2) on the surface element, ρ is the surface reflectance, ω and ϕ are the polar and azimuthal angles in spherical coordinate system. For Lambertian reflectors, the ratio of radiance for two arbitrary points on the surface is identical to the ratio of their irradiance.

So far the radiometric equations for quantifying the irradiance on a Lambertian reflector have been presented. These equations address the lens distortion effects by taking the geometrical relationships between each element on the target surface and the camera lens into account. In order to use this method practically, the values of R, θ, ϕ, $\mathrm{d}S'$, together with the pixels corresponding to $\mathrm{d}S'$ on the digital image (the position of $\mathrm{d}S'$ in image space) must be known. A proper image processing routine such as a camera calibration code can accurately determine these values. This will be covered in section 3.1.3 however it is important to discuss the method to implement the above calculations using the calibration toolbox in Matlab here.

The toolbox can be used to determine the pixels on the sensor that correspond to $\mathrm{d}S$. Assuming that the pixel sizes are uniform, by counting the pixels, the area of $\mathrm{d}S'$ can be determined in pixels unit. By dividing the $\sum_{\mathrm{d}S'} PV_i$ by the number of pixels on $\mathrm{d}S'$, the effect of magnification and tilting are already taken into account. Hence, Equation 3.11 can be simplified as below:

$$\frac{B_1}{B_2} \propto \frac{n_2^2\cos(\phi_2)^3 \sum_{\mathrm{d}S'_1} PV_i}{n_1^2\cos(\phi_1)^3 \sum_{\mathrm{d}S'_2} PV_i} \tag{3.14}$$

where n_i is the number of pixels associated with $\mathrm{d}S'_i$. Note that a $\cos(\phi)^2$ term is the remnant of the omitted R^2 term since the magnification factor is a function of the projection of R on the optical axis. This equation has been used in the experimental results in this section.

Vignetting effect

In simple terms, vignetting, sometimes called light fall-off, is the drop in light collection efficiency closer to the edges of an image. Sometimes the pupil distortion introduced in the last section is considered a component of vignetting but here, vignetting refers to mechanical and pixel vignetting. In mechanical vignetting, light is intercepted by some physical obstacles

such as the front rim or the internal side wall of the optical system, the camera lens.
In pixel vignetting the quantum efficiency and photon collection of the pixels is reduced from a maximum value when the light impinges upon them obliquely. For example, in a CMOS sensor, there is distance between the chip surface and the photo-diode; the light travels through a tunnel to reach the photo-diode. Hence if the incident angle of the light ray on the pixel is shallow, some fraction of the light will be blocked by the tunnel walls. For more detailed explanation on different causes of vignetting, the reader is referred to imaging optics text books such as [135, 137, 138]. Quantifying the contribution of each cause individually can be a difficult task. Mechanical vignetting depends on the camera lens geometry whereas pixel vignetting depends on the physical and geometrical micro structure of the sensor [138].

3.1.3 Image rectifying

Extracting the true illumination data using the photographic method requires correction of the perspective effects and image distortion. Parretta et al. [134] introduced an analytical method to do this. The method introduced by them requires the geometry of the experimental set-up, such as the relative position and orientation of the camera and the reflector, to be known. This can be very difficult to achieve in practice due to assembling inaccuracies. Additionally, the measurement of these dimensions after setting up the camera can suffer from significant inaccuracies. In order to overcome these difficulties, a camera calibration method can be used to precisely and more readily extract all necessary geometrical dimensions.
The camera calibration method uses the image of an object or texture, such as a black and white check board, with known dimensions to calculate the extrinsic (location and orientation) and intrinsic (focal length, distortions, ...) characteristics of the camera set-up. An open source camera calibration toolbox for MATLAB has been developed by Jean-Yves Bouguet [139].
Such a calibrator also correlates a position in the world coordinate system (in mm) to the image coordinate system (in pixel units). Figure 3.2 shows an example of the camera calibration using this toolbox. The size of each square in Figure 3.2a is 20mm$\times$20mm which is used as the reference dimension for correlating the coordinates system on the check board (object space) to the coordinate system on the image (image space). After calibration, the location of the camera and its orientation is accurately determined in the world coordinate systems. The world coordinate system is attached to the surface of the check board and the small red axis corresponds to its origin.

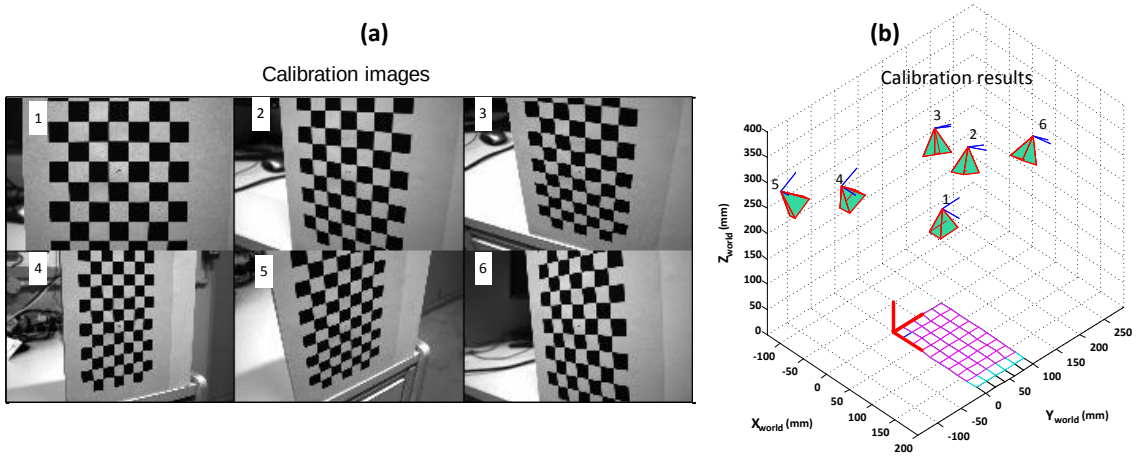

Fig. 3.2 Camera calibration to extract the camera parameters (a) Various images of a check board with 20mm×20mm squares; (b) The location of the camera corresponding to the images from which the orientation of the camera is determined (the normal to the base of the pyramid corresponds to the direction the camera is facing and the tip is its position

Using the transformation from the world coordinates to the image coordinates and also the position and orientation of the camera, the pixels corresponding to a specific area element on the Lambertian target together with the angle between the camera axis and the camera-element line (ϕ) can be easily determined. Let's assume $P(x,y,z)$ is a location in the object space in the world coordinates system. We can say that:

$$\cos(\phi) = \frac{x_n(x-x_c)+y_n(y-y_c)+z_n(z-z_c)}{(\sqrt{(x-x_c)^2+(y-y_c)^2+(z-z_c)^2} \times \sqrt{x_n^2+y_n^2+z_n^2}} \tag{3.15}$$

In the above equation, (x_n, y_n, z_n) is the camera orientation vector (camera axis) and (x_c, y_c, z_c) is the camera location vector. Both these vectors are in the world coordinate system and are acquired from the calibration results. Considering the fact that the surface normal vector at the element in world coordinate system is $(0,0,1)$, θ can be determined in a similar way as below,

$$\cos(\theta) = \frac{(z_c - z)}{\sqrt{(x-x_c)^2+(y-y_c)^2+(z-z_c)^2}} \tag{3.16}$$

The transformation from the world to image coordinate system is as below:

$$\begin{pmatrix} X \\ Y \\ Z \end{pmatrix} = R_m \times \begin{pmatrix} x \\ y \\ z \end{pmatrix} + T_m \tag{3.17}$$

In this equation, (x,y,z) is the central point of the element in the world coordinate system and (X,Y,Z) is the corresponding point in the image coordinate system (in pixels unit). R_m and T_m are the rotation and translation matrices that are calculated by the camera calibration toolbox. This technique is used in the following experimental procedure.

3.2 Experiment and data analysis

3.2.1 Verifying the linearity of the CMOS sensor

It is important to note that commercial digital camera manufacturers apply a non-linear transformation to the original sensor data to prepare the results for photographic application. However in order to perform radiometric measurements using these cameras the raw image data, prior to the non-linear transformation, is required.
A Canon EOS 450D camera with a CMOS sensor was used in this experiment.This camera was used because it is an easily accessible consumer camera. However one can use cameras with an optional gamma correction feature. In that case, the raw output of the camera can be directly used in the radiometric calculations. In case of using a consumer camera such as the one that was used in this work, the user must be cautious about the gamma encoding that the manufacturer implements internally in the camera. The linearity of the sensor was investigated by exposing it to a diffuse white surface illuminated by faint light at various shutter speeds. It was assumed that by halving the shutter speed (doubling the exposure time) the number of photons reaching any pixel on the sensor will double. This is equivalent to doubling the irradiance level on the surface keeping the shutter speed constant. By averaging the pixel grey scale values of a small window ($300px$ by $300px$) on the image, the sensor response was calculated. The result has been presented in Figure 3.3, with the pixel grey scale values reported in 16-bit format (maximum value = 65,535).
As it is seen in this graph, the sensor shows high level of linearity up to 5.3×10^4 of pixel grey value in 16-bit depth. The equation of the linear regression with 95% confidence level of the coefficients is as below:

$$PV = 1.749 \times 10^5 (ExposureTime) - 43.9 \tag{3.18}$$

The value of the intercept is insignificant in comparison to the pixel grey scale values in 16-bits. Throughout the measurements, the pixel grey scale values were kept below 5.3×10^4 to maintain the linearity of the measurements.

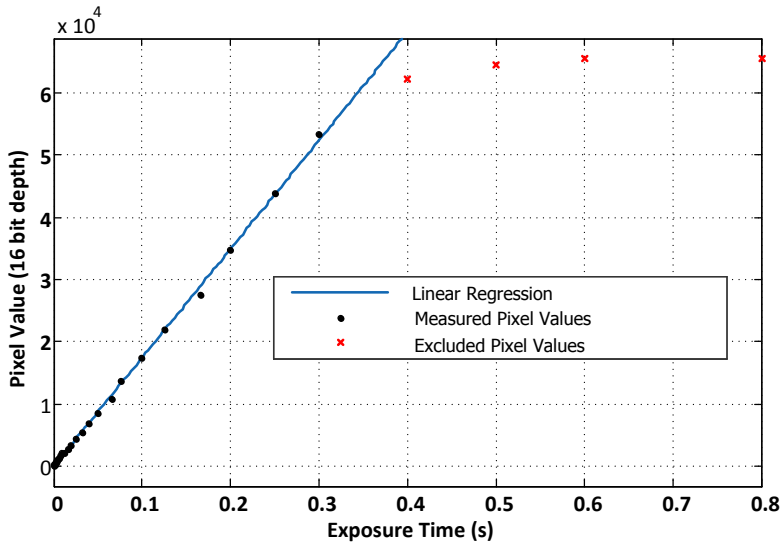

Fig. 3.3 Pixel grey scale value of Canon EOS 450D (raw data) vs. exposure time. The points denoted by ($\times$) are excluded from regression because they are either saturated or close to saturation; $R^2 = 0.9952$.

3.2.2 The experiment set-up

A 0.5 mm-thick Gore® diffuse reflector was used as the reflector target. This material is highly Lambertian with reflectance of over 96% for the spectral range of up to near infra red. The variation of its spectral reflectance is less than 3% for 400-750nm spectral range which is compatible with the photographic cameras' sensor sensitivity range and the solar spectrum. Insignificant degradation under thermal exposure, extremely low absorption, non-flammability, UV stability, and continuous operating temperature of up to 288°C makes this material suitable for flux measurement targets [140].

A VOLPI Intralux 5100 light source that has a halogen lamp with a colour temperature of 3433 K was used to illuminate the target. The power of the source was adjusted to avoid sensor saturation. The location of the reflector and the light source were kept fixed. In order to avoid shading, the camera was located always out of the rays' path. Since the spectrum of this source is different from the solar spectrum, the camera can not be calibrated for the absolute solar irradiance values using this lamp.

A check board pattern with square sizes of 20mm$\times$20mm printed on A4 paper was located in front of the reflector. Six images with constant focal distances, f, from arbitrary locations were taken to calibrate the intrinsic properties of the camera (see Figure 3.2a). After calibrating the intrinsic parameters, the camera was fixed at a location and an image of the check board was taken under normal light (see Figure 3.4a and c). The check board was then

removed and an image of the diffuse reflector under the illumination generated by just the light source was acquired (see Figure 3.4b and d). Since the check board paper thickness is insignificant, it can be assumed that the reflector and check board surfaces are co-planar. The corresponding dark image at very low light (dark room) was captured and subtracted from the illumination image. In outdoor measurement where there is less control on environmental light, the dark image has a more significant effect. The check board image is used to extract the location (coordinates) of each point on the target and relate its radiance to the values read from the grey-scale diffuse target image.

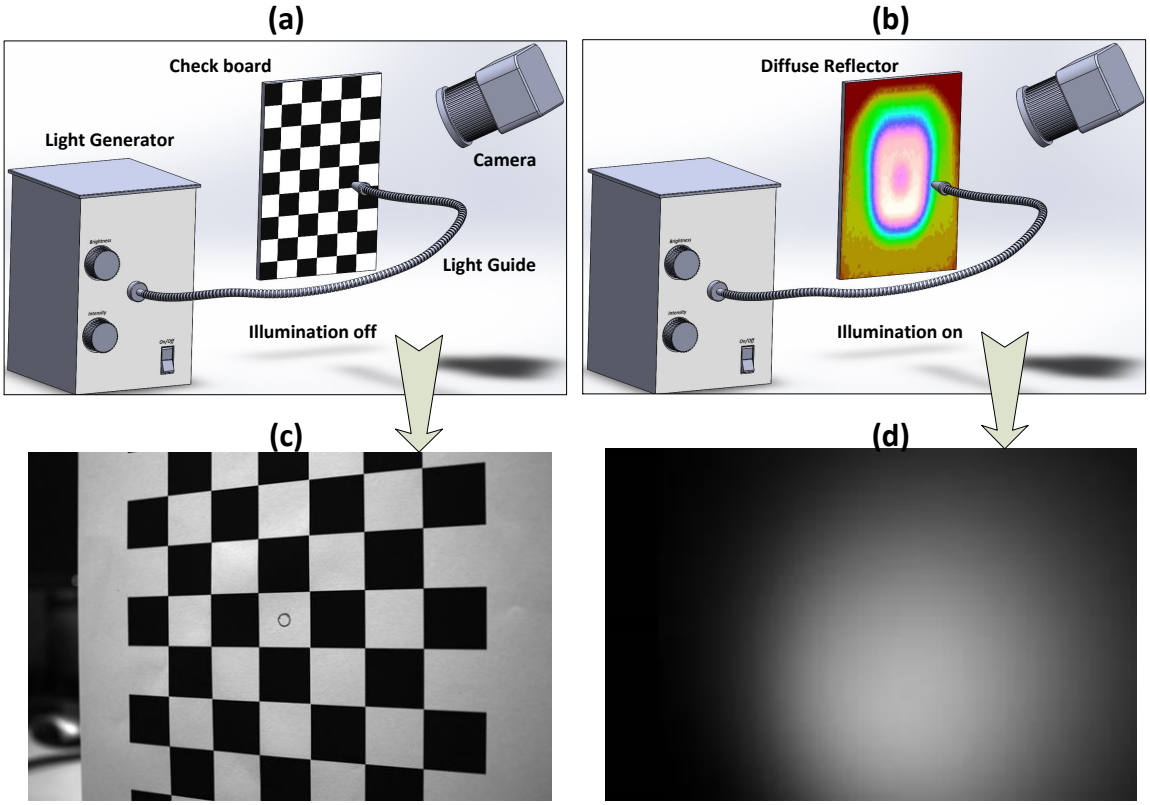

Fig. 3.4 The experiment procedure. (a) Imaging the check board pattern under ambient light. (b) Imaging the diffuse target without ambient light but with source illumination. (c) The captured check board pattern. (d) Illumination distribution on diffuse reflector for set-up shown in (b)

3.2.3 Verifying the Lambertian reflection

It is well known that the radiance of an ideal Lambertian surface is invariant with respect to its distance and angle to a digital camera. This property was used to verify the "Lambertian-ness" of the Gore diffuse reflector. A 20mm×20mm piece of the reflector was imaged from a set of arbitrary locations. In all of these images the camera was targeted directly to the centre of the small reflector to make sure that the pixel values are not affected by optical and pixel vignetting effects. For each camera location, the angle θ was calculated based on the method explained in section 3.1.3. The value of ϕ is zero because the camera is directly oriented toward the centre of the area element which means that the element is on the optical axis of the camera. The results are presented in Figure 3.5.

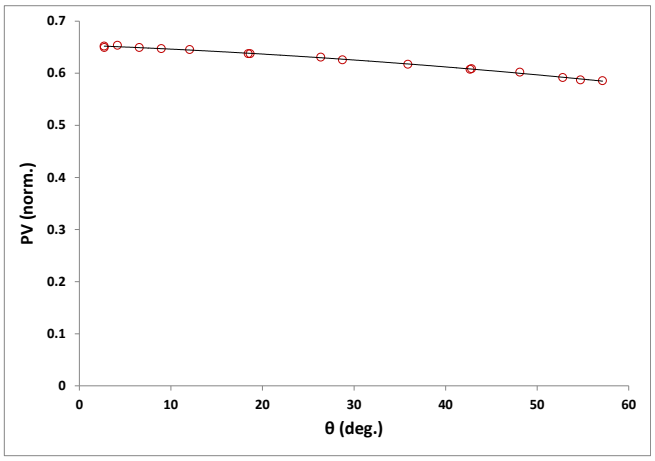

Fig. 3.5 The normalised pixel grey scale value of a fixed small element on Gore diffuse reflector from different view angles under invariant illumination

Different regression methods were examined including a cosine function; however the best results were obtained using a second order polynomial regression:

$$PV(\theta) = -0.0312\theta^2 - 0.038\theta + 0.6539 \tag{3.19}$$

where θ is in radians and R^2 value of the fitting is 0.997. The final radiometric results were adjusted using a corrective coefficient:

$$C(\theta) = \frac{0.6539}{-0.0312\theta^2 - 0.038\theta + 0.6539} \tag{3.20}$$

3.2.4 Data analysis

After acquiring the images from the check board and the illuminated target, the transformation between the world coordinates (attached to the target in mm) and the image coordinates (attached to the image plane in pixels) were calculated using the method explained in section 3.1.3. Using this transformation, the group of pixels that correspond to a square area element (2mm×2mm) on the target were determined. The sum of the pixel grey scale values correlated to these pixels was calculated. The values of ϕ, θ, R for each element as well as the camera location and camera normal vector were computed using a MATLAB code. The B value corresponding to each element was calculated using Equation 3.10. By repeating this process for the entire target area, the relative distribution of irradiance on the target is extracted with 2mm resolution. However, this resolution can be refined further until the image of the element is smaller than one pixel on the camera sensor.

3.3 Results and discussion

Using the camera calibrator, the focal length of the camera was calculated to be 24.6±0.1mm. The locations of the camera with respect to the target are shown in Figure 3.6. The maximum and minimum distances between the camera and the centre of the target were 253.1mm and 188.3mm respectively. The area on the reflector scanned by the camera was larger than 160mm by 220mm.

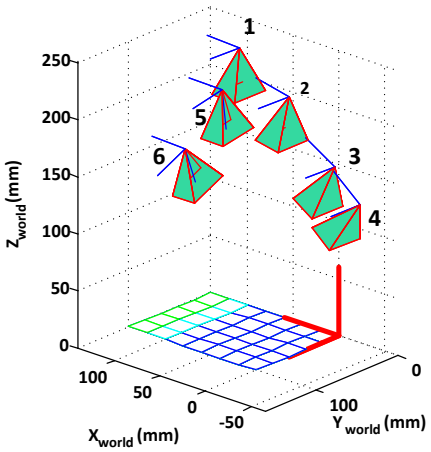

Fig. 3.6 The location of the camera for 6 different arbitrary cases; the red lines indicate the origin defined arbitrarily

In the work presented by [134] the distance between the camera and the centre of the target was about 350mm scanning an area of 20mm by 20mm. By defining a proximity factor as $P = \sqrt{a^2+b^2}/Z$ where Z is the camera-target distance, measured from the camera to the centre of the target, and a and b are the half width and half height of the scanned area in the world coordinate system respectively. A high P value means that the camera has a short distance relative to the size of the spot and provides an indication of the extent to which the surface elements are off-axis. In the current experimental set-up P is larger than 0.54, compared to 0.004 in the experimental set-up of [134]. This makes the impact of cosine laws significant in the current measurement.

The surface of the target can be mapped by any spatial resolution limited by the resolution of the camera sensor. In this work, resolutions of 5mm×5mm and 2mm×2mm were used to sample the surface. The distribution of the irradiance for the 6 configurations presented in Figure 3.6 has been presented in Figure 3.7. For the sake of clarity in the figures, 5mm resolution was used for plotting, but the data analysis in this section is based on 2mm resolution.

The angle between the camera optical axis and the surface normal for the element at the

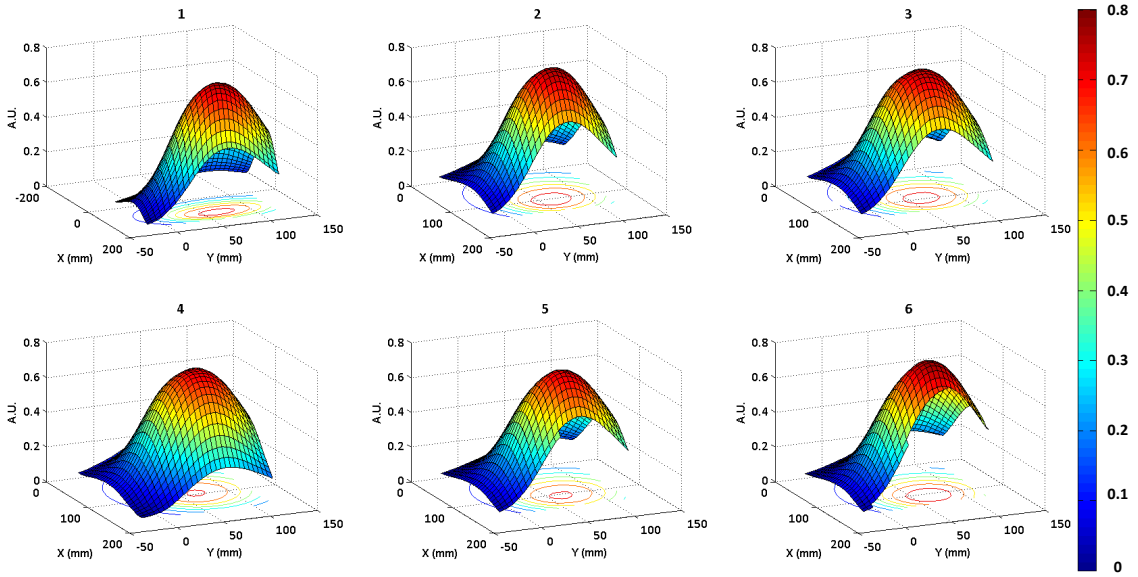

Fig. 3.7 The distribution of irradiance (W/m^2) on the target for the same illumination pattern from different close range view points; the surface has been meshed by 5mm square elements; X and Y are in mm and in world coordinate system; all figures are normalised uniformly hence the z-values of the sub-plots are comparable

coincident point of the optical axis, OO' and the target is equal to θ. This value is an indication of the“oblique-ness" of the view angle and has been listed in Table 3.1. In this

table, the camera target distance is the distance between the camera and point O (see Figure 3.1). The loci of the maximum irradiance was determined to be at (100.6, 64.4)±(4.4mm, 3.6mm). The area scanned by the camera changes by varying its location and orientation. Hence, in order to compare irradiance distributions obtained at each location a common region to all images was determined; in this case a rectangle with opposite corners at (x,y) coordinates of $(15,-20)$ and $(130,120)$.

Table 3.1 Camera-target geometry as determined using the camera calibration method.

Position	camera location (mm) (x,y,z)	θ (degree)	camera-target distance (mm)
1	(64.2, 48.5, 253)	1.36	253.1
2	(10.9, 48.2, 223.1)	9.96	226.5
3	(-39.2, 47, 174.1)	27.15	195.7
4	(-66.4, 46.8, 148)	38.2	188.3
5	(49.7, 87, 230.4)	9.12	233.3
6	(51.89, 129.8, 190.7)	22.7	206.7

The mean value of irradiance at location (x,y) within this region was calculated as

$$\bar{I}_i(x,y) = \frac{1}{n}\sum_{1}^{n} I_i(x,y) \tag{3.21}$$

where $I_i(x,y)$ is the estimated irradiance at location (x,y) and n is the number of measurements used, which was 6 in this work.
The standard error in the mean value of irradiance at location (x,y) was calculated as

$$SE_{(\bar{x},\bar{y})} = \frac{s(x,y)}{\sqrt{n}} \tag{3.22}$$

where $s(x,y)$ is the standard deviation of the 6 calculated irradiance values. Using this standard error, a 95% confidence interval (CI) for the estimate of mean irradiance can be determined by applying the Student's t-distribution statistical coverage factor, t, such that

$$I_{95\%CI(x,y)} = \bar{I}_i(x,y) \pm tSE_{(\bar{x},\bar{y})} \tag{3.23}$$

where $t = 2.571$ for a two sided distribution of $n-1 = 5$ degrees of freedom.
The distribution of the irradiance confidence interval upper bound for measurement area is presented in Figure 3.8. The maximum value of the relative error with respect to the mean was $\pm 10\%$, which was found to occur towards the edges of the measurement region.

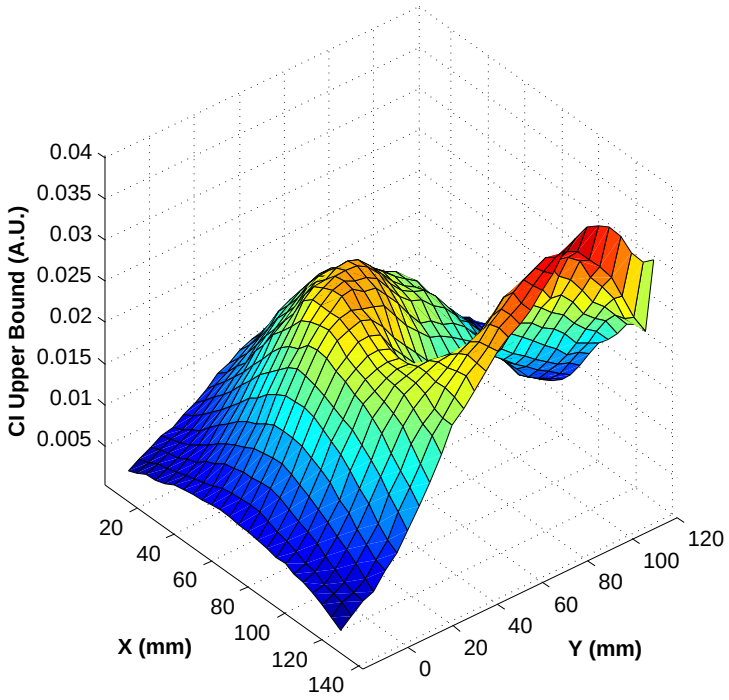

Fig. 3.8 The irradiance 95% confidence level upper bound over the measurement area.

The errors reported here are statistical errors focusing on the variation of measurement from different camera location and orientation. The assumption was that by holding the light source and the target fixed, the measurement should ideally report the same irradiance distribution. Sources of error in the result include, but are not limited to, pixel vignetting, camera lens vignetting, ignoring the Fresnel reflection losses at the surfaces of the lens, spatial variation in reflectance of the target, and also light instability.For example, a total vignetting ratio - the *PV* fall off across the image - of about 35% have been reported for digital cameras[141, 142]. This includes lens and sensor vignetting. In general vignetting increases as focal length decreases which intensifies the vignetting effect in close range radiometry. Several methods such as using multiple images from the same illuminated target at different camera directions can be used to estimate the vignetting ratio at different regions of the image. For the method applied here, it was assumed that the radiance of a point on the surface remains the same, and the PV variation after correcting for lens distortion is due to the vignetting effect of the sensor and camera lens. For more information on these methods the reader is referred to references [142, 143]. However the applicability of these methods must be examined for close range radiometry in solar concentrators and also the accuracy of such methods should be quantified.

Although the Gore reflector is highly Lambertian, variation of its reflection profile with respect to the incident angle of the beam on the surface is unknown. This should not be

mistaken with the angular reflection that was reported in section 3.2.3. In that section, the angular reflectance of the surface at a constant incident angle of light was measured. However a reflectometer with a variable beam incident angle can be used to measure the variation of the reflection profile with respect to the beam angle.
The ray angle at the camera entrance lens affects the reflection losses from the lens. The surface elements at very oblique angles i.e. off-axis elements, experience slightly lower radiant flux transmitting through the lens due to higher Fresnel losses. Simple anti reflection coating reduces reflection losses at their designed incident angle but gradually lose their effectiveness at other angles.
Further work is required to quantify the effect of each of these causes or eliminate them. An interesting approach in quantifying the contribution of these factors is conducting a detailed ray tracing simulation for a known camera set-up and configuration. Such simulation requires the intrinsic camera properties and the structure of the lens at a specific focal length, zooming factor, and aperture to be known. By comparing the ray tracing results to a measured value from a known illumination profile, one may be able to quantify each effect.
Since the target surface is not perpendicular to the optical axis of the camera, off axis elements will be out of focus. This results in a blurring effect in the image which doesn't have significant effect on camera calibration but causes a smoothing effect on the mapped irradiance distribution. In the blurred regions of the image light rays corresponding to an element are captured by the adjacent pixels and image elements. The method introduced in this work has the capability to be developed further to measure the illumination pattern on curved surfaces such as tubes and spheres which has extensive applications in radiative heat transfer.

3.4 Summary

In this section, a measurement method for quantifying the illumination profile on a flat surface using close range radiometry has been outlined. Solving radiometric equations requires precise determination of the experimental set-up including the location of the camera with respect to corresponding target. A camera calibration method using a textured pattern was used to accurately determine these parameters. The reflection from a quasi Lambertian surface at the same location was coupled to the spatial data acquired from the calibration method to quantify the illumination profile. This method can also be developed further to measure the illumination profile on curved surfaces such as tubes and spheres with known

geometrical shape. This method is used in chapter 5 to size the spectral beam spitting receiver for a commercial parabolic trough.

Chapter 4

Spectral beam splitting using direct absorption and wave interference light filtering

---

The content of this chapter has been published as a journal article:
Ahmad Mojiri, Cameron Stanley, Robert A. Taylor, Kourosh Kalantar-zadeh, and Gary Rosengarten. "A spectrally splitting photovoltaic-thermal hybrid receiver utilising direct absorption and wave interference light filtering". In: *Solar Energy Materials and Solar Cells 139*(2015)

Wave interference [18, 34] and selective absorption [9] filters can be used for spectral separation in CPVT systems. Wave interference filters employ a number of high and low refractive index transparent materials (multilayer thin film filters) or a transparent layer with continuously varying refractive index (rugate filters) deposited on a substrate to generate light filtering effect via selective reflection. Selective absorbers use pure liquids, solution mixtures [9, 62], nano-fluids [144, 108], or solid state optical filters to filter out the specific spectral band(s).

Wave interference filters provide more flexibility compared to selective absorbers [18]. Such filters can be broad band-pass which are made of one or two edge filters in combination. These two edge filters (a long and a short pass) can be deposited on either side of a transparent substrate. A concern in such band pass filters is to combine them in such a way that one edge filter does not create transmission peaks in the rejection band of the other [17]. However, they normally consist of a large number of layers to produce an effective broadband filtering effect, but this results in higher fabrication cost.

In this chapter, a hybrid photovoltaic-thermal (CPVT) receiver to be mounted in a linear Fresnel concentrator has been introduced and analysed. The receiver incorporates a selective absorber together with a wave interference filter (a dichroic mirror) to form a band pass filter. A simple filtering structure that is introduced is relatively facile and low cost to manufacture. The proposed configuration takes advantage of direct solar absorption that has been studied by Minradi [145] and Otanicar [57, 58] to simplify the structure of the required dichroic coating. The details of the design are given in the next section where an optical analysis of the whole system is presented and the advantages of using the proposed configuration are discussed.

4.1 Design description

In this chapter, "hybrid collector" term refers to the combination of a rooftop linear micro-concentrator (LMC) and a CPVT receiver installed at its focal axis. This section, briefly introduces the proposed hybrid receiver design and then discusses its applicability in an LMC hybrid collector. The design aims at reducing the complexity of the dichroic filter which is expected to be achieved via combining it with a selective absorption filter. In this case, the necessity of using a band pass dichroic filter which is more complex to fabricate is eliminated. This is discussed below in more details.

4.1.1 The hybrid receiver design

The proposed hybrid receiver consists of a high temperature (above $150°C$) liquid channel optically coupled to high-efficiency back-contact crystalline silicon (Si) cells that have been optimised for concentrating photovoltaic (CPV) applications [146]. The overall configuration of the receiver is shown in Figure 4.1. Concentrated light propagates in the upward direction and enters the receiver through the front glass. It passes through this highly transparent glass and enters the semi-transparent liquid flowing inside the channel. The liquid serves as a heat transfer fluid as well as a spectral filter. Vivar and Everett [62] have provided a review on the optical and heat transfer properties of a range of liquids for such an application. Candidate liquids considered in this work are water, propylene glycol, and ethylene glycol due to the combination of the thermal stability and optical properties. The optical properties of these liquids will be discussed in the following sections.

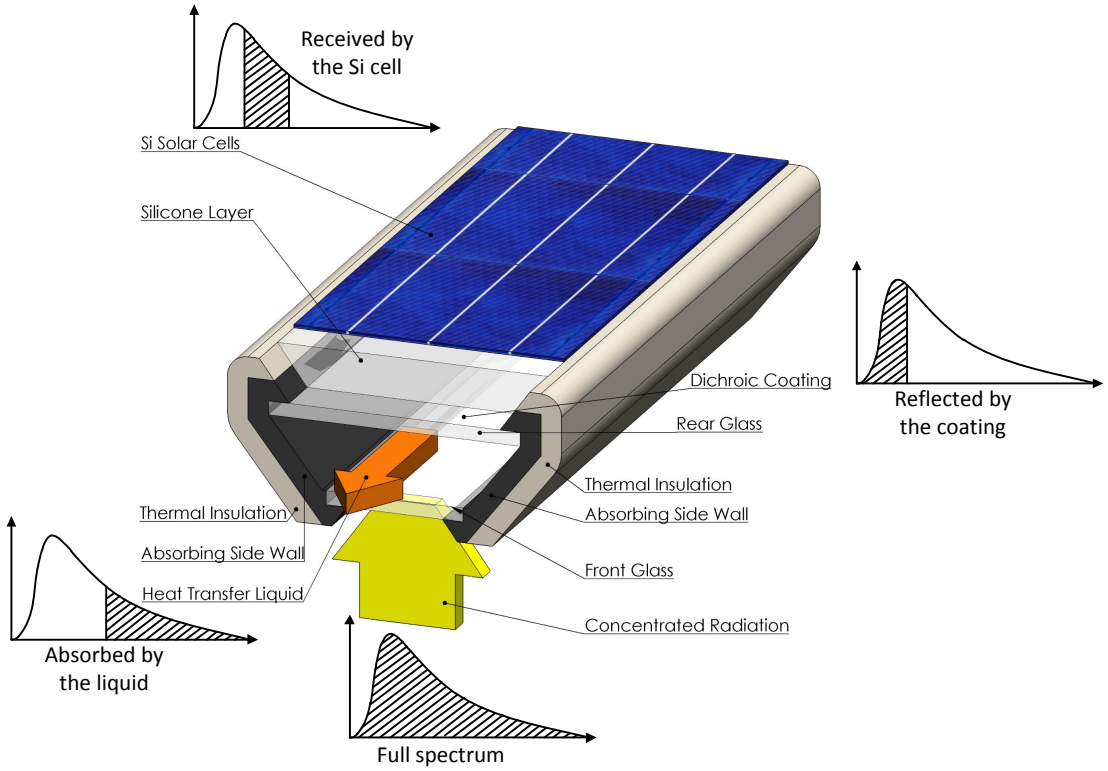

Fig. 4.1 Concentrated light enters the receiver through the front glass and is filtered by the dichroic coating at the top side of the rear glass. The filtered light is sent to the PV cells and the rest is absorbed by the side walls or directly in the fluid.

The liquid channel acts as a short pass filter with a cut-off wavelength at near infra-red, e.g. 1200 nm. Shorter wavelengths first pass through both the liquid and the highly transparent rear glass with negligible attenuation, and then land on the dichroic coating at the top face of the rear glass. This coating acts as a long pass filter, reflecting all wavelengths shorter than 600 nm and transmitting the remainder of the spectrum. The reflected and transmitted rays are absorbed by the absorbing side walls and the PV cells, respectively. The silicone layer between the rear glass and the PV cells is required to achieve a better refractive index match between various layers to minimise the reflection losses. It also provides a high thermal resistance between the hot channel and the PV cells.

The absorbing side walls are made of metal for better heat transfer across the wall with a highly absorbing coating on their surface. It is important to note that this surface does not need to be a selective surface because it is in direct contact with the liquid layer that absorbs all infra-red thermal emission from the hot surface. The outside of the absorbing side walls

are thermally insulated.

4.1.2 The rooftop linear micro-concentrator (LMC)

The LMC is a one-axis solar tracking concentrator developed and commercialised by Chromasun Pty Ltd [147–149]. It comprises of two sets of Fresnel reflectors, each set with 10 curved mirrors, encapsulated inside a glass canopy. The mirrors are controlled by a tracking system to focus the sunlight on a central axis – 25 cm above the mirror plane. The whole collector is 3.3 m long, 1.2 m wide and 0.3 m high. The glass canopy protects the internal components from wind, dust and water. Figure 4.2a and 4.2b show a schematic of the LMC. Figure 4.2c is the cross-sectional view showing ray tracing conducted for the LMC under normal angle of incidence on the canopy. This concentrator has been optimised for high temperature ($100 - 220°C$) thermal applications and has been recently retrofitted for combined heat and power generation by installing highly efficient silicon cells coupled to a cooling channel [150, 151].

The LMC provides the concentrated radiation to the hybrid receiver which transforms it into useful electrical and thermal energy. To estimate the overall performance of the system, the whole configuration has been analysed as an integrated package.
The orientation of the LMC, sun angle, shadows from the structure on the mirrors, and the geometrical arrangement of the mirrors can affect the spatial and angular distribution of light at the focal region. In addition to this, the spectral distribution of the sunlight at the focal region of the LMC is different from the original solar spectrum because the sunlight passes through the cover glass and gets reflected by the Fresnel mirror. Both of these components have wavelength dependant optical properties (reflectivity and transmissivity).

4.2 Methods

4.2.1 Optical modelling of the LMC

Since the LMC has a relatively complicated concentrating mechanism including a set of small mirrors with different curvatures and complicated shading effects, computer aided ray tracing is required. In this study ZEMAX (version 13) [152] software was chosen to study the optical characteristics of the system. To do this, the sun was defined as a radial source at infinity. Since the sun is not a point source (because of its significant size compared to

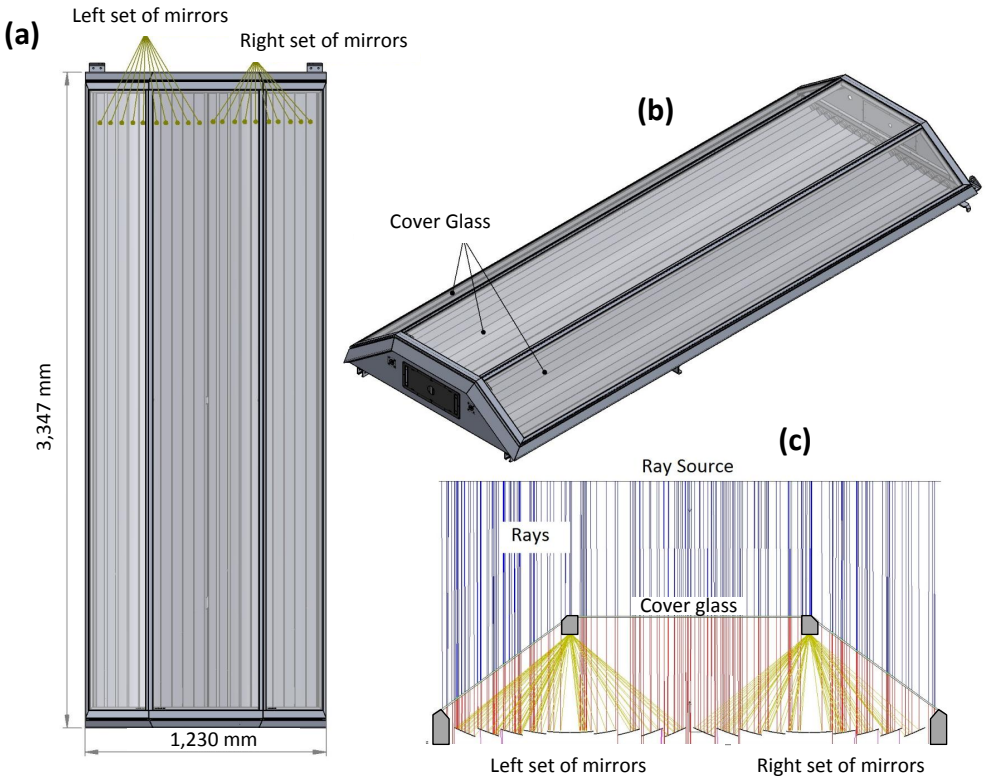

Fig. 4.2 Schematic of the LMC developed by Chromasun Pty Ltd. (a) top view, (b) isometric view, and (c) cross section of the LMC, consisting of 2 sets of narrow curved mirrors focusing sunlight onto two focal lines

its distance from the earth), a sun half angle of 0.27° [100] was incorporated in the model. Accounting for this is important because it can influence the radiation distribution at the focal region of solar concentrators.

In a spectrally splitting receiver, the variation of the spectrum at the focal region plays a key role in determining the system performance. Because the LMC uses Fresnel reflectors to concentrate the light, very little of the diffuse portion of the global radiation reaches the receiver(s). Hence only the spectrum of beam radiation was defined as the ray source in ZEMAX. This data was acquired from the reference air mass 1.5 solar spectrum [153]. Total solar radiation flux is calculated using the data provided by [153] as $I = \int_{280\,nm}^{4000\,nm} I_\lambda \, \mathrm{d}\lambda$, where, I is the irradiance of the light source (W/m^2), I_λ is the direct and circum-solar spectral irradiance of the sunlight, acquired from [153], and λ is wavelength. The above integration was carried out numerically resulting in $900\,W/m^2$ as the source power.

4.2.2 The spatial and angular flux distribution on the receiver

Figure 4.3 shows the distribution of the incoming power on the bottom face of the front glass (i.e. the aperture of the hybrid receiver). In this figure it has been assumed that the tracking system and the surface quality of the mirrors are ideal; any variation in these factors can change the spatial distribution of the flux at the focal point of any solar concentrator. For example, including tracking errors and mirror surface inaccuracies in the optical modelling will cause a wider focal spot (lower solar concentration) as well as a non-symmetrical flux distribution.

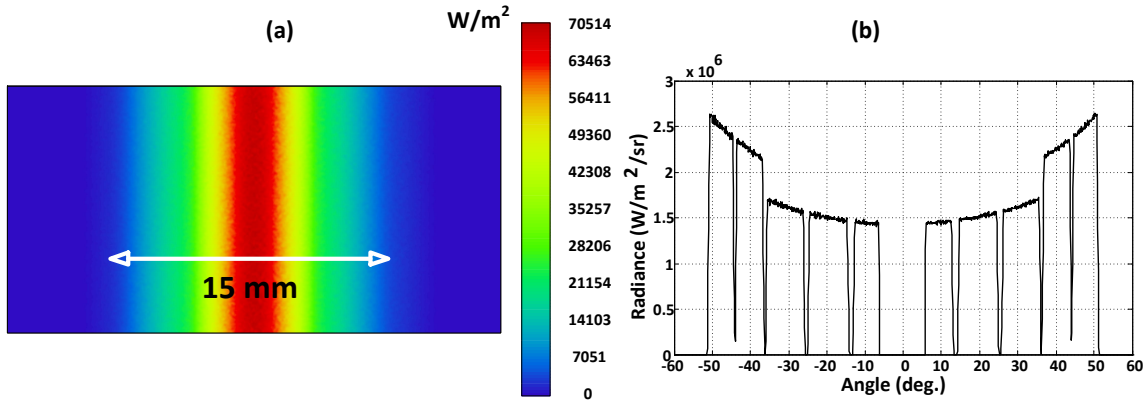

Fig. 4.3 flux distribution at the bottom face of front glass of the LMC. (a) Spatial distribution of irradiance (W/m^2); the width of the spot size is 15 mm containing more than 99% of incoming radiation. (b) Angular distribution of the radiance ($W/m^2/sr$)

Figure 4.3b shows the angular distribution of the incoming flux on the bottom surface of the front glass. This parameter is important in designing the side absorber walls as well as the dichroic coating since this design relies on not having the side walls intercept the rays before they reach the dichroic coating. At the same time, the dichroic coating should be designed based on the weighted mean angle of incidence to optimise the optical performance of the coating, that depends on the angle of incidence [19]. By changing the angle of incidence on thin film interference coatings, the reflection transmission curve deviates from the design point [18].

4.2.3 The weighted mean angle of incidence on the dichroic filter

In the proposed geometry, the thin film coating (dichroic filter) should be designed for non-collimated, concentrated radiation, as shown in Figure 4.3b. Since the reflection-transmission

characteristics of thin film optical filters are sensitive to the incident angle, different approaches such as curved [100] and tapered filters [19] have been suggested. Because these methods require sophisticated fabrication processes, a flat filter was considered here but the effect of incident angle was minimised by optimising the filter for the power weighted mean angle of incidence (*PWMAI*).

The total radiative power (W) to the surface of the dichroic coating is given by Equation 4.1 [154]:

$$I(W) = \int_A \int_{2\pi} \int_0^{\infty} I(\vec{r}, \hat{s}, \lambda) \hat{n}.\hat{s} \, \mathrm{d}\lambda \, \mathrm{d}\Omega \, \mathrm{d}A. \tag{4.1}$$

where, $I(r, \hat{s}, \lambda)$ is spectral directional radiation intensity ($W/m^2/nm/sr$) at a location specified by the position vector of $\vec{r}$, $\hat{n}$ is the unit normal vector of the receiving surface, $\hat{s}$ is the unit vector in the direction of the incoming radiation towards the surface, λ is wavelength (nm), Ω is solid angle, and A is the surface area of the receiver. For a flat surface depicted in Figure 4.4, $\hat{n}$ is a unit vector in Y direction and $\hat{n}.\hat{s}$ describes the cosine effect of the angle of incidence ($\cos\theta$). Noting that $\mathrm{d}\Omega = \sin(\theta)\,\mathrm{d}\theta\,\mathrm{d}\phi$, Equation 4.1 can be described in spherical coordinates to simplify the calculations as shown in Equation 4.2. The coordinate system is defined (with respect to the receiver) in Figure 4.4.

$$I(W) = \int_A \int_0^{2\pi} \int_0^{\frac{\pi}{2}} \int_0^{\infty} I(\vec{r}, \theta, \phi, \lambda) \cos(\theta) \, \sin(\theta) \, \mathrm{d}\lambda \, \mathrm{d}\theta \, \mathrm{d}\phi \, \mathrm{d}A. \tag{4.2}$$

The spectral and spatial integration was carried out based on the ray tracing results. The radiant intensity, $I(\theta, \phi)$ (W/sr) is calculated by ZEMAX, which includes the cosine effect. Hence Equation 4.2 can be simplified as:

$$I(W) = \int_{2\pi} I(\theta, \phi) \, \sin(\theta) \, \mathrm{d}\theta \, \mathrm{d}\phi. \tag{4.3}$$

Since the absolute value of θ drives the optical properties of the dichroic coating, the PWMAI was calculated for half of the incident flux (symmetric about the $Y-Z$ plane). It will be shown that this minimises the standard deviation of the angle of incidence (SDAI) on the dichroic coating. Since the concentrating mirrors have a cylindrical shape, they create an angular distribution only in the $X-Y$ plane.

The PWMAI and SDAI of the angle of incidence on the thin film coating can be calculated using

$$\theta_{mean} = \frac{\int_0^{\pi} \int_0^{\pi/2} \theta I(\theta, \phi) \, \sin(\theta) \, \mathrm{d}\theta \, \mathrm{d}\phi}{\int_0^{\pi} \int_0^{\pi/2} I(\theta, \phi) \, \sin(\theta) \, \mathrm{d}\theta \, \mathrm{d}\phi}, \tag{4.4}$$

$$\sigma = \sqrt{\frac{\int_0^{\pi}\int_0^{\pi/2}(\theta-\theta_{mean})^2 I(\theta,\phi)\,\sin(\theta)\,\mathrm{d}\theta\,\mathrm{d}\phi}{\int_0^{\pi}\int_0^{\pi/2} I(\theta,\phi)\,\sin(\theta)\,\mathrm{d}\theta\,\mathrm{d}\phi}}, \tag{4.5}$$

where, θ_{mean} and σ are PWMAI and SDAI, respectively. Using the above equations, $\theta_{mean} = 18.6^{\circ}$ and $\sigma = 4^{\circ}$. If normal AOI instead of the calculated PWMAI had been used, the standard deviation, σ, would have increased from 4° to 10°. This shows that using θ_{mean} will result in a narrower angle of incidence distribution and more accurate light filtering by the dichroic coating. However, it should be noted that designing the thin film coating according to this mean angle doesn't necessarily minimise the effect of broad angle of incidence on the filter, although it definitely reduces its effect.

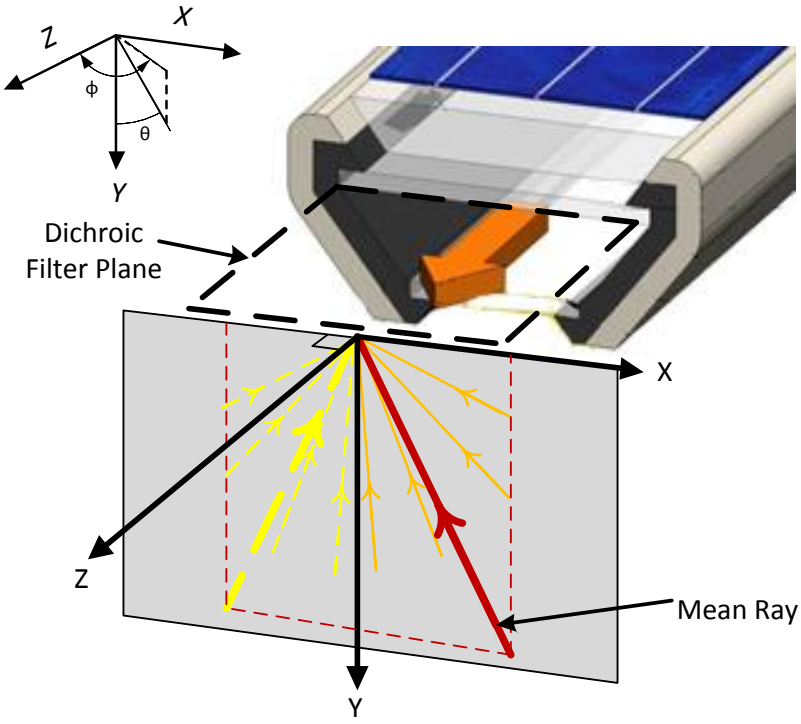

Fig. 4.4 Spherical coordinate system at the location of the thin film filter; Z-axis is along the length of the collector; Y-axis is normal to the dichroic surface; all the rays are in the X-Y plane. The "Mean Ray", depicted by a solid bold arrow (red and yellow) is the power weighted mean average of the rays impinging upon the dichroic filter. The red and yellow arrows corresponds to the mean ray for the set of the incoming rays either side of the Y-Z symmetry plane.

4.2.4 Thin film optical filter design and fabrication

The dichroic filter is a long pass filter with cut-off wavelength at about 600 nm and should be optimised for the PWMAI (18.6°) calculated in the previous section. TiO_2 and SiO_2 were selected as the high and low refractive index materials. For this pair of materials, the use of a $(0.5H\ L\ 0.5H)$ configuration results in a satisfactory performance as a long pass filter on a glass substrate [17], where H and L are quarter wavelength thicknesses of TiO_2 and SiO_2, respectively, at a reference wavelength.

Because the refractive indices of these materials depend on the coating process and their crystal structure, a thin layer of each material was deposited on a silicon wafer using electron beam evaporation employing an "Intlvac Nanochrome Electron Beam Evaporation" system at low substrate temperature in the range of 27 to 60°C. The refractive indices of these layers were then measured using ellipsometry, with the results presented in Figure 4.5. The growth rates of SiO_2 and TiO_2 were $1A/s$ and $0.5A/s$ respectively.

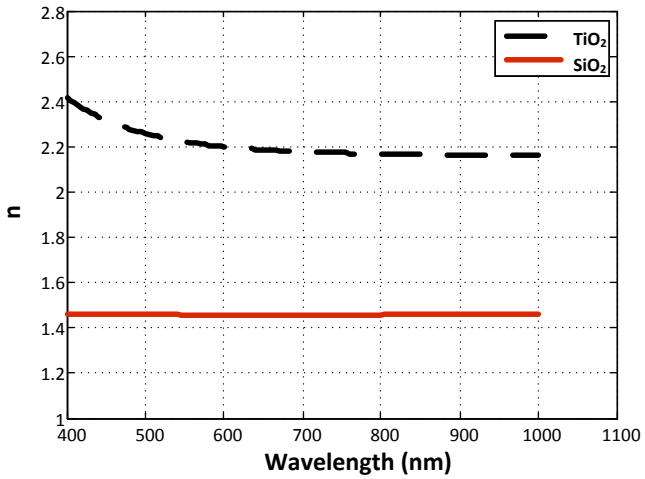

Fig. 4.5 measured refractive indices of TiO_2 and SiO_2 deposited by e-beam evaporation at low substrate temperature

Designing a simple filter with low stack thickness compared to typical commercial ones improves its cost effectiveness as well as its endurance under thermal cycling. Hence, the filter design started with an initial 7 layer-stack formula of $(0.5H\ L\ 0.5H)^3$. The reference wavelength was 500 nm and the refractive indices acquired above were used in the design process. The front and back media were glass and air, respectively. The layers were then refined to match a transmission target. The refinement process was carried out in Openfilters [155], an open source code for designing wave interference filters. The mathematical

procedure of the code has been explained in [156].

In the refined stack, all layers thinner than 10 nm have been eliminated. However this refinement was processed based on an ideal edge filter target, as depicted with the dashed line in Figure 4.6(a), regardless of the solar spectrum. The result is not necessarily the optimum filter because the solar spectrum hasn't been accounted for. Through a second optimisation stage, the filter minima location can be optimised according to the solar spectrum. In this study, this task has been accomplished by a simple optimisation process of the electrical output of the PV cells over the spectral distribution of the transmitted light through the filter. This is explained here.

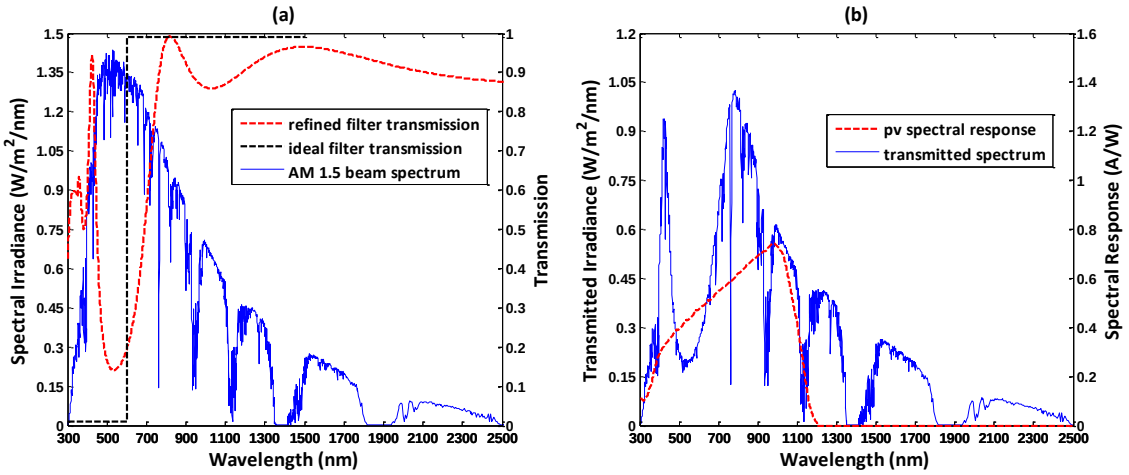

Fig. 4.6 (a) Spectral transmission of the thin film filter vs. the direct beam component of the AM 1.5 solar spectrum. (b) Spectrum of the transmitted radiation through the thin film filter vs. the spectral response of the high efficiency Si solar cell

The equations for calculating the spectral transmission and reflectance of a thin film structure are well known [17]. Here, they are used to optimise the minima loci of the transmission curve according to the solar spectrum and spectral response of the cells. For this purpose the open circuit voltage, V_{OC}, and fill factor, FF, were considered 0.645 and 0.776 respectively at 25°C which are in the typical range of the cells as reported in [157]. The efficiency of the cell for the spectral band corresponding to the filter in the effective spectral band of the filter, i.e. 300-1200 nm, can be approximated as below:

$$\eta_{pv} = \frac{FF\, V_{OC} \int_{300}^{1200} SR\, I_{\lambda}^{T}\, \mathrm{d}\lambda}{\int_{300}^{1200} I_{\lambda}^{T}\, \mathrm{d}\lambda}, \tag{4.6}$$

where I_λ^T and SR are the spectral irradiance of the transmitted radiation and the spectral response of the cell respectively. I_λ^T is calculated as $I_\lambda^T = T_\lambda\, I_\lambda$, where T_λ is the spectral transmissivity of the thin film assembly and can be calculated as [17]:

$$T_\lambda = \frac{4\eta_0 Re(\eta_m)}{(\eta_0 B + C)(\eta_0 B + C)^*}, \tag{4.7}$$

where admittance, η, is calculated as $\eta_p = N\xi / \cos(\nu)$ for p-polarisation and $\eta_s = N\xi \cos(\nu)$ for s-polarization. N is the complex refractive index as $n - ik$ and $\xi = 2.6544 \times 10^{-3}\ s$. η_0 and η_m are the admittance of air and substrate respectively. B and C can be calculated as [17]:

$$\begin{bmatrix} B \\ C \end{bmatrix} = \prod_{r=1}^{q} \begin{bmatrix} \cos(\delta_r) & i\sin(\delta_r)/\eta_r \\ i\eta_r \sin(\delta_r) & \cos(\delta_r) \end{bmatrix} \times \begin{bmatrix} 1 \\ \eta_m \end{bmatrix}, \tag{4.8}$$

where $\delta_r = 2\pi N s d_r \cos(\nu)/\lambda$. The parameter d represents the physical thickness of the r_{th} layer, while ν is the angle of the ray in the film, derived from Snell's law.
In order to move the minima of the transmission curve, the thickness of the layers is multiplied by the same scalar factor, s, to make all layers consistently thicker or thinner. For $s < 1$ and $s > 1$ the transmission curve is shifted towards short and long wavelengths respectively. By maximising η_{pv} in Equation 4.6 over the transmitted spectrum, the optimum filter design and layer thicknesses can be determined.

4.2.5 Optical properties of the heat transfer liquids

As mentioned before, 3 different types of heat transfer liquids were considered for absorbing the IR range of the spectrum. Figure 4.7 presents their absorption indices. The transmission values in Figure 4.7, have been calculated using Beer's law: $T = e^{(-4\pi k d)/\lambda}$, where T is transmission, k is absorption index, d is light path-length, and λ is wavelength.

4.3 Results and discussion

The optimisation of the filter started with the refined stack and ended up with the optimal stack as presented in Table 4.1. Figure 4.8a shows the variation of η_{pv} as a function of s. In this figure, a value of 0.84 for the scalar factor s corresponds to the maximum PV conversion efficiency of approximately 27%, i.e. the optimal stack. It is important to note that this efficiency was calculated based on the transmitted power through the filter as described in

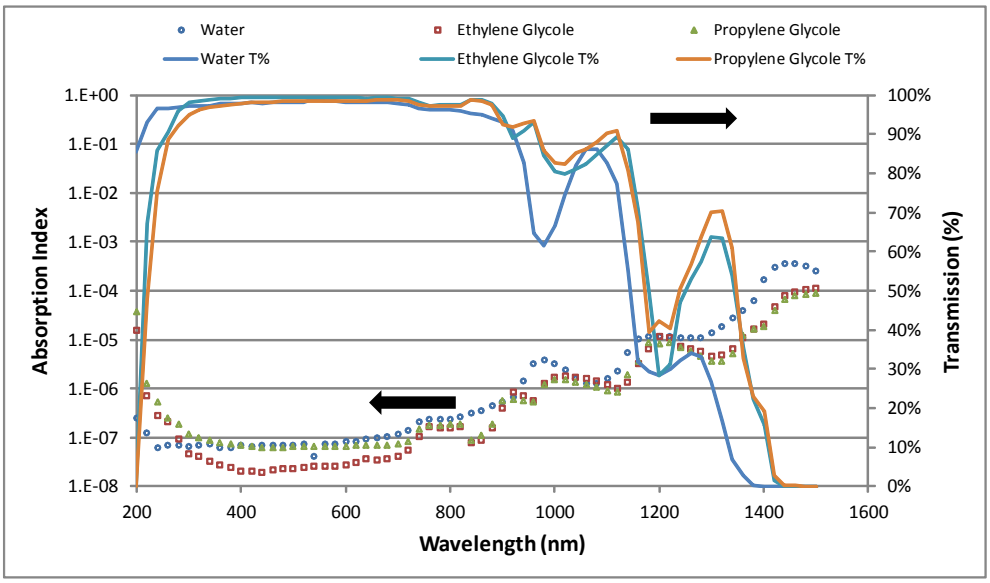

Fig. 4.7 Measured absorptive index of water [158], ethylene glycol, and propylene glycol [58] accompanied with the respective transmission coefficient with a sample thickness of 10mm

Equation 4.6.

Figure 4.8b shows the effect of s on the transmission curves; the optimal and refined stacks transmission curves have been denoted by $s = 0.84$ and $s = 1$, respectively. The minimum transmission of the optimal stack occurs at 460 nm at 18° AOI.

Table 4.1 The structure of the dichroic coating for fabrication

	Refined stack		Optimal stack	
#	Material	Thickness (nm)	Material	Thickness (nm)
1	TiO_2	55	TiO_2	46
2	SiO_2	94	SiO_2	79
3	TiO_2	64	TiO_2	54
4	SiO_2	96	SiO_2	81
5	TiO_2	50	TiO_2	42
	Total	359 nm	Total	302nm

The fabricated filter transmission curve is presented in Figure 4.10a. The measurement results were compared for $AOI = 0°$ for both cases. The "designed 5-layer filter" corresponds to the result of the simulation, and the "fabricated 5-layer filter" corresponds to the result of the optical transmission measurements on the fabricated filter. A very close match is observed

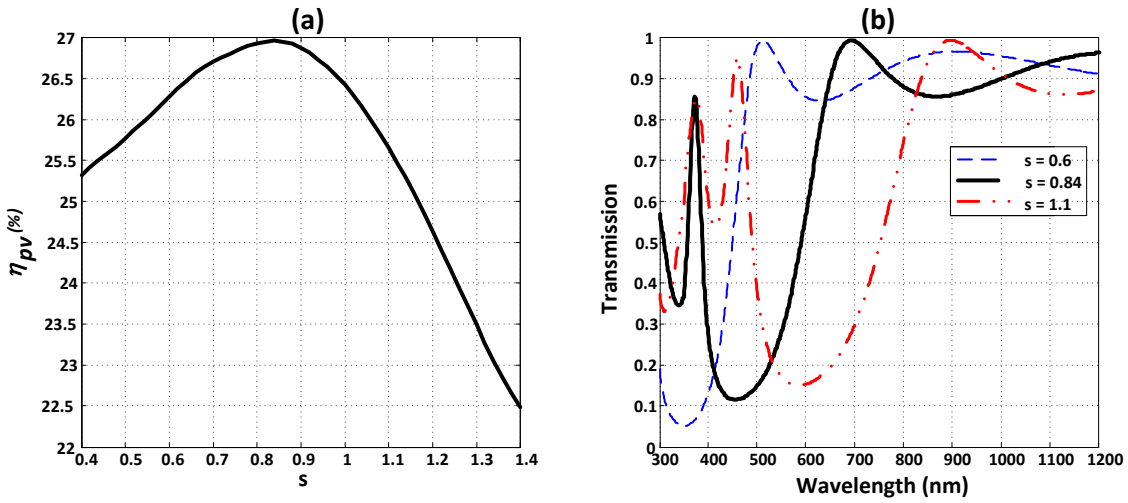

Fig. 4.8 (a) The effect of s on the efficiency of the silicon cells; the efficiency is based on the transmitted light in the range of 300-1200 nm. (b) The effect of s on the transmission curve of the filter; $s = 0.84$ corresponds to the optimum filter with the maximum PV conversion efficiency at 18° AOI.

between the curves. There is a divergence for wavelengths of shorter than 400 nm which is caused by the absorption of TiO_2. In the simulated model, TiO_2 was considered non-absorbing for all wavelengths. However this discrepancy is useful as the short wavelengths are blocked. These two curves are compared against an ideal sharp edge long pass filter that can't be generally achieved by configurations with a small number of layers.

The long pass filter shown in Figure 4.8b was assembled in the proposed receiver configuration to function as a band pass filter. The test assembly is shown in Figure 4.9. The liquid in this measurement was water, which has good optical and heat transfer properties. The optical transmission of the whole assembly, the receiver, is presented in Figure 4.10b, along with the spectrum of AM1.5 and an ideal sharp band pass filter with the cut-off edges at 600 nm and 1125 nm. 1125 nm has been chosen according to the band gap of silicon. The short side of the band can be tuned according to the heat-electricity demand ratio. That is, by moving the short edge towards shorter wavelength the heat to electricity production ratio decreases and vice versa. Thus, tunability can be achieved by scaling the thickness of the layers in the thin film structure.

The transmitted and blocked spectra based on the transmission curve of Figure 4.10b are presented in Figure 4.10c. The transmitted radiation reaches the PV cells and the blocked radiation is either absorbed directly by water or is reflected towards, and absorbed by, the

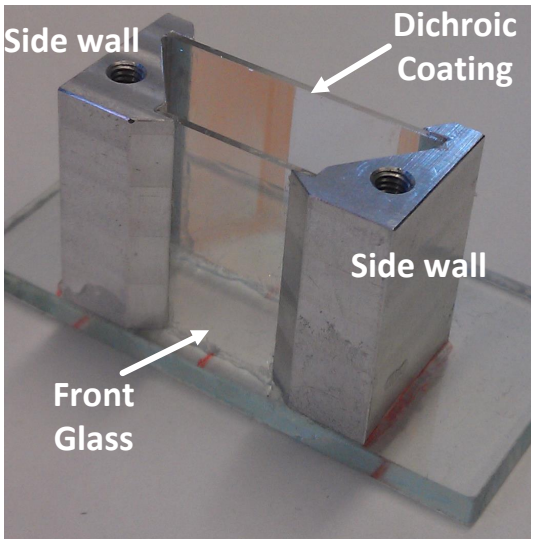

Fig. 4.9 The test sample of the receiver for measuring its optical transmission

side walls and then transferred into water as heat.
The baseline efficiency of the Si cells considered here is about 20.6% at 25°C and a CR of 1 under the full AM1.5 spectrum. However they can convert 26.1% of the transmitted radiation from this filter to electricity. The total PV conversion of the whole system based on the total power reaching the front glass decreases to 12.9% because less light is directed to the cells. It should be noted that these PV conversion values are functions of cell temperature.
The blocked radiative power is converted into heat in the thermal receiver which is now thermally decoupled from the cells and can reach temperatures above the working limit temperature of the cells. The heat transfer characteristics of beam splitting receivers with similar geometry has been studied extensively in [159] showing that the cell temperature increases by approximately 1°C per 8°C rise in the temperature of the thermal receiver.
The sensitivity of the filtering system to the AOI in the short wavelengths, where the thin film structure is driving the optics is presented in Figure 4.10d. By increasing the AOI the transmission curve of the whole receiver shifts towards shorter wavelengths. The minima of the transmission curve moves from 480 nm to 453 nm when the AOI on the front glass changes from 0° to 40°. Slightly more variation is observed in the midpoint of the cut-off edge where the transmission of the filter is 50%. The 50% transmission point moves from 598 nm at $AOI = 0°$ to 550 nm at $AOI = 40°$.

For a more detailed analysis of the receiver optical performance, ray tracing modelling based on the fabricated filter was carried out in ZEMAX. Figure 4.11a shows the light propagating

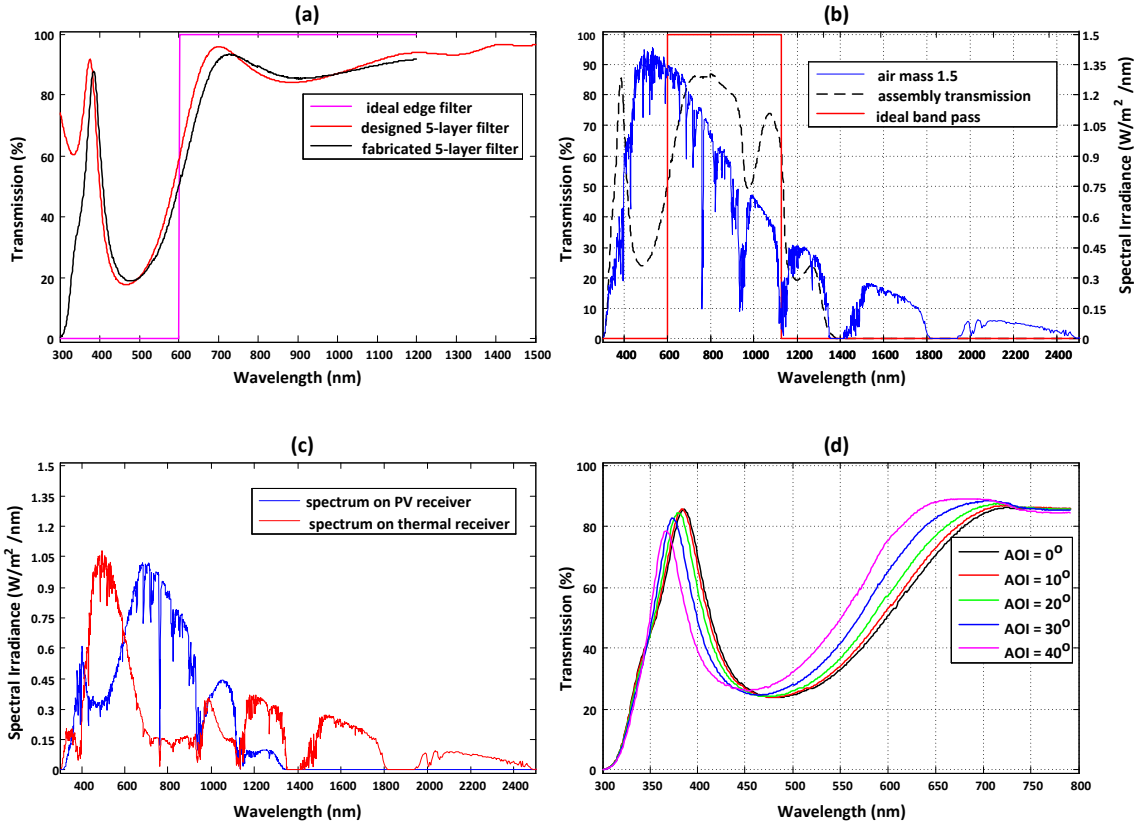

Fig. 4.10 The measurement results for the receiver sample. (a) The ideal edge filter is considered a sharp long pass filter with cut-off wavelength at 600 nm. (b) The transmission of the receiver sample including the thin film filter and water as the liquid filter; the ideal band pass filter has cut-off edges at 600 nm and 1125 nm for Si cells. (c) The comparison between the spectral distribution of the radiation reaching the PV and thermal modules independently. (d) The effect of the angle of incidence on the front glass of the receiver.

in the hybrid receiver. As it is seen in this figure, the highest level of concentration is at the front glass. A part of the incoming radiation is reflected by the rear glass with the dichroic coating at its top face (far from the liquid). While a majority of the reflected light is absorbed by the side walls, 3.9% of that bounces back out of the receiver through the front glass, which combines with 4.3% Fresnel reflection of the front glass-air interface. As shown in Table 4.2, the total reflection loss of the receiver is 8.2%.

As mentioned before, a part of the radiation is absorbed directly by water. Figure 4.11b shows the absorbed power (in Watts) by water in a 40mm long section. Since water is highly absorbing in the infra-red, the majority of absorption takes place in the liquid channel just on top of the front glass. However, in the 1100 - 1400 nm band, water has moderate absorption

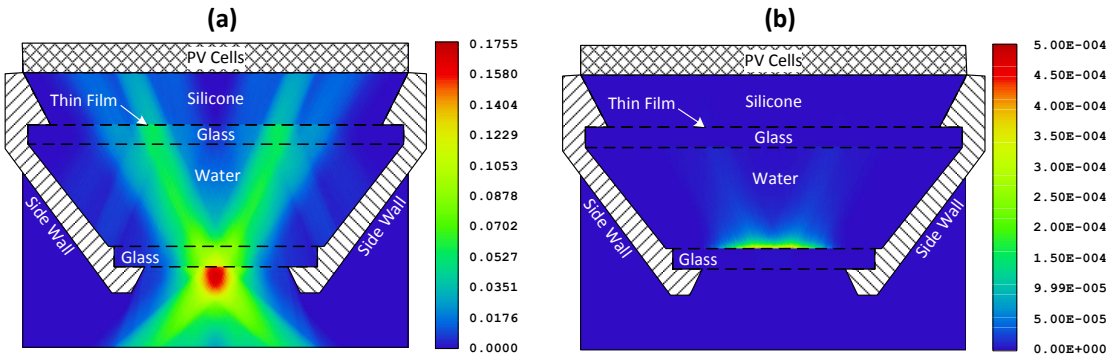

Fig. 4.11 Ray tracing simulation of the hybrid receiver. (a) The incident flux at each point in the receiver. (b) The absorbed flux inside the water volume. The values reported on the colour bars are in Watts showing the amount of power at each point for 40 mm of the receiver length.

Table 4.2 Energy balance of the model; percentage of the energy absorbed by each part of the hybrid receiver with respect to the total energy of light impinging upon the front glass

Items	Percentage
Absorbed by the front glass	0%
Absorbed by water	22.9%
Absorbed by the rear glass	0.00%
Absorbed by the side walls	14.3%
Absorbed by the PV cells	54.5%
Total reflection loss (inc. Fresnel and missed rays)	8.2%

and light rays in this range penetrate deeper into water and are absorbed in deeper regions. It should be noted that in this work, pure water was considered for the volumetric absorption and its scattering effect was ignored.

The graph in Figure 4.12 shows the spectral distribution of different components of radiation in the fabricated receiver. It should be remembered that the aim of the design was to direct the wavelength between 600 nm and 1125 nm to silicon cells; Figure 4.12c shows that the majority of the radiation reaching the PV is in this spectral band. On the other hand the absorbing side walls absorb the radiation below 600 nm that is reflected by the dichroic coating, as seen in Figure 4.12d. The missed reflected rays in Figure 4.12(b) contain wavelengths across the whole solar spectrum range because a portion of this flux is due to Fresnel reflection from the front glass that causes reflection across the whole spectrum striking the glass; however another component of the reflected-missed rays comprises of the wavelengths reflected by the dichroic coating and missed by the side walls . These wavelengths are mainly in 300 - 600 nm range. This is the main reason why the graph in Figure 4.12b has much higher

intensity in this range. The results of numerical integration of the spectral distribution on the PV cells is shown in Table 4.3. It should be noted that in this table the percentage is based on the total amount of energy reaching the PV cells. The ideal percentage assumes an ideal band pass filter with sharp cut-off wavelengths at 600 nm and 1125 nm without any optical losses. Such an ideal filter is 100% transparent within this range and 100% reflective outside it.

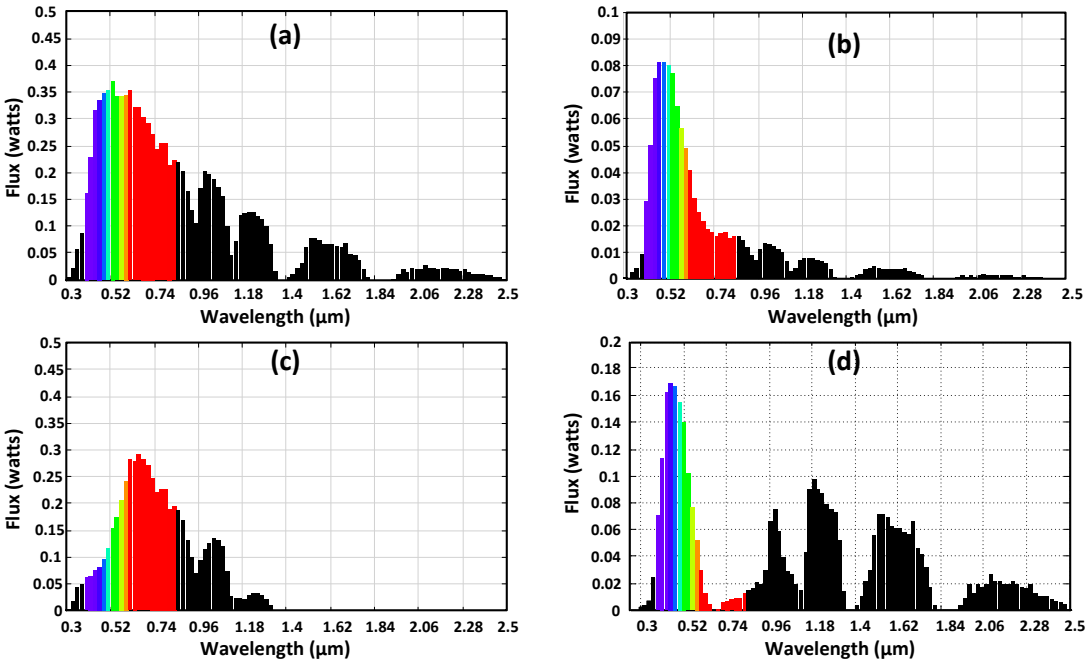

Fig. 4.12 The spectral distribution of the (a) incoming flux, (b) reflected missed flux, (c) absorbed flux by the cells, (d) the radiation absorbed by the thermal components; the vertical axis is in Watts. The black columns are outside the visible range

Table 4.3 The spectral analysis of the radiation reaching the PV cells

Spectral band	Percentage	Ideal Percentage	Comment
$\lambda < 600$ nm	22.6%	0%	undesirable range
600 nm $< \lambda <$1125 nm	73.3%	100%	desirable range
$\lambda >$ 1125 nm	4.1%	0%	undesirable range

The energy absorbed by each component of the receiver was calculated by integrating the respective flux distribution impinging upon each part. Table 4.2 presents the energy balance of the model. The percentage is based on the total energy entering the receiver at the front

glass. It should be noted that the reflection losses include the Fresnel reflection from the front glass and the light reflected back out of the receiver by the dichroic coating.
The analysis shows that by using the current receiver geometry, 54.5% of the radiation hitting the front glass reaches the cells, with 73.3% of this flux within the desired wavelength range. This is comparable to the ideal case in which the power of the AM1.5 spectrum in 600-1125 nm range reaches the cell. For the ideal case, 48.7% of the total AM1.5 power would have been directed to the cells and 100% of that would have been in the desired range.
Two causes for this difference are: (1) non-ideal spectral splitting and (2) reflection losses. Non-ideal filtering can be improved by designing a sharper dichroic filter with more layers at the cost of higher fabrication expense. The reflection losses can also be mitigated by optimising the geometry of the dichroic coating e.g. using a V-shape dichroic filter to direct the rays towards the side walls more effectively. The Fresnel losses from the front glass can be reduced by the use of anti-reflection coatings.
Unlike the PV efficiency, the efficiency of the thermal component of the system is less sensitive to the performance of the dichroic mirror because the absorbing side walls of the receiver can absorb all the wavelengths across the solar spectrum efficiently. In order to verify the worthiness of such a filtering device from an efficiency point of view, the PV conversion efficiency with the measured filter, ideal filter, and without any filtering is presented in Table 4.4.

Table 4.4 PV conversion performance under different conditions and spectral bands

	η_{PV} based on total incoming power	η_{PV} based on power reaching the cells
No filtering	20.6%	20.6%
Ideal filter	14.5%	29.8%
Fabricated filter	12.6%	26.1%

Here, “no filtering" refers to the conversion efficiency of the cells under the full spectrum without any optical losses which occur due to the presence of the filter. Using the “ideal filer" reduces the total PV conversion of the system to 14.5% based on the total power reaching the hybrid receiver; again, this represents the case with no optical losses. The “fabricated filter" takes the optical losses and non-ideal spectral splitting effects into account. Compared to ideal filtering, the total PV conversion and the conversion based on the band of the light reaching the cells are 1.9% and 3.7% lower (in absolute values), respectively. It is well known that the thermal and electrical efficiencies of hybrid solar collectors are typically lower than those of separate thermal and photovoltaic collectors respectively, which is also

the case here.

The solar weighted transmission of the filter accompanied by the transmission values for the liquid channel including the water layer, front and rear glass panels are presented in Table 4.5. As it is observed in this table, the dichroic filter is highly reflective in the spectral band shorter than 600 nm and is highly transparent in the desired band between 600 nm and 1125 nm. The high transmission of the dichroic filter (92.6%) beyond 1125 nm is not an issue as long as the transmission of the liquid channel in the same range is low; the liquid channel has 12.5% transmission in this range. This value is determined by the intrinsic absorption coefficient of the liquid and its thickness.

Table 4.5 The transmission of the dichroic filter and the liquid channel

	Spectral band	Transmission
Dichroic filter		
	300 nm- 600 nm	33%
	600 nm - 1125 nm	72%
	1125 nm- 4000 nm	92.6%
Liquid channel		
	300 nm - 600 nm	98.2%
	600 nm - 1125 nm	91.7%
	1125 nm - 4000 nm	12.5%

Increasing the liquid thickness can suppress the transmission above 1125 nm but it should be noted that it can reduce the transmission in 600 -1125 nm range as well. Lower transmission in this range means lower electrical power. So, the thickness of the liquid layer is optimised in accordance with the desired ratio of electrical to thermal output. Another possible solution for optimising the transmission of the liquid channel at 1125 nm is using other liquids with a better matched spectral absorption index.

As previously mentioned the Fresnel reflection loss from the front glass was 4.3%. This loss occurs mainly due to the reflection from the front face of the glass panel, as the back face is in direct contact with water (smaller difference in the refractive index, $n = 1.33$ for water and $n = 1.5$ for K10 glass).

The other source of reflection loss is the reflected rays from the dichroic coating that miss the receiver side walls. These rays leave the receiver cavity through the front glass. This issue can be addressed by the further geometry optimisation of the receiver; e.g. using a V-shape rear glass to slightly tilt the dichroic mirror and direct the reflected light towards the side absorbers more efficiently. Using this method, one should be careful about the effect of angle

of incidence on dichroic coatings i.e. the dichroic coating should be optimised for the new angular distribution of light that includes the tilt angle of the mirror.

4.4 Summary

This chapter presented the possibility of combining dichroic filters with direct absorbing liquids to achieve spectral splitting of sunlight in a hybrid solar receiver. The receiver geometry was optimised for Chromasun's linear micro concentrator; however it can be optimised for other types of concentrators with different sizes, such as parabolic troughs. The modelling results showed that the receiver is capable of directing 54.5% of the solar spectrum to the PV cells; 73.3% of this energy is in the desired range of 600 -1125 nm band. The vast majority of the remaining solar spectrum is absorbed by the liquid channel and is converted to heat.

Since the results mentioned above are derived from simulations, they can be difficult to achieve from a real-world prototype. It would be a wise decision to follow a theoretical design that shows more promising simulation results because real-world losses and inaccuracies can significantly affect the performance of any system. Although the suggested configuration in this chapter presented the possibility of the idea, its predicted performance was not high enough to be considered to be a real-world prototype. In the next chapter, an alternative design is presented that addresses some of the issues related to the configuration presented here.

Chapter 5

Spectral splitting using direct absorption

The content of this chapter has been published as a journal article:
Ahmad Mojiri, Cameron Stanley, David Rodriquez-Sanchez, Vernie Everett, Andrew Blakers, and Gary Rosengarten. "A spectral-splitting PV-thermal volumetric solar receiver". In: *Applied Energy 169*(2016)

To increase the overall efficiency of spectral beam splitting PV-T receivers, achieving satisfactory spectral splitting accuracy is required. Thin film wave interference filters, as studied in the previous section, can be designed and fabricated to suit a vast range of applications. However, for broad band spectrum they can be costly and complicated to fabricate [24]. This is a particular problem for linear concentrators because, unlike point focusing systems, they need a significant filter area along their entire optical axis because of their optical characteristics.
In this chapter, a volumetric filtering method is introduced that minimises the number of optical interfaces to design a spectrally splitting PV-T receiver for linear solar concentrators. The design aims for simplicity, high spectral splitting accuracy, ease of manufacturing, and low cost. To achieve this, volumetric light filtering with the help of semiconductor doped glass (SDG) filters has been chosen to divide the solar spectrum between a high temperature thermal absorber and silicon photovoltaic cells.

5.1 Volumetric beam splitting receiver design description

The schematic in Figure 5.1, presents the configuration of the PV-T hybrid receiver. It consists of two liquid channels: low and high temperature. The high temperature channel

is made of borosilicate glass to contain the high temperature fluid stream. The size of this tube is dictated by the illumination profile at the focal region of the linear concentrator. This channel also contains a long pass filter as a thermal absorber at its mid-section.

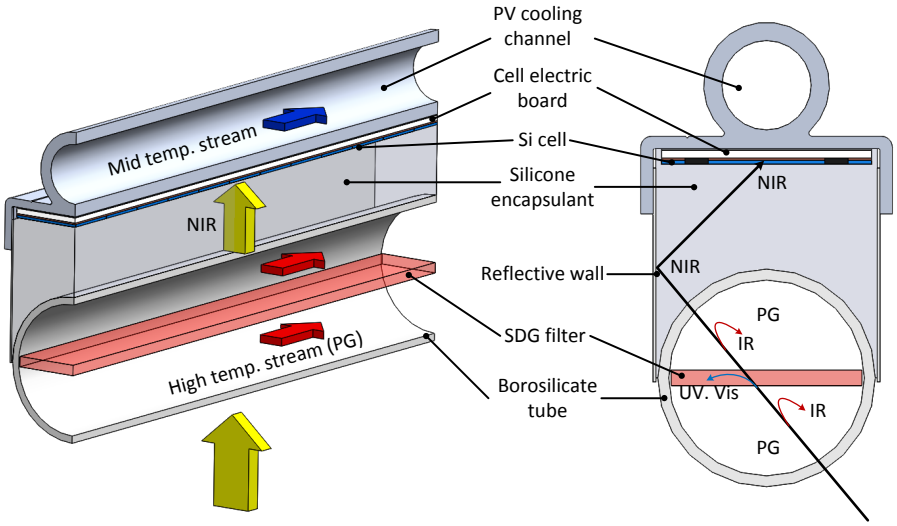

Fig. 5.1 Selective absorption spectral beam splitting photovoltaic-thermal hybrid receiver

The spectral beam splitting mechanism in the receiver should be able to direct the wavelengths between λ_{vis} and $1120nm$ to the silicon cells, and absorb the counterpart as heat, where λ_{vis} is a cut-off wavelength which can be between $\sim 600nm$ and $\sim 750nm$. Tuning this wavelength can provide different ratios of heat to electricity generation from the receiver, which can be selected to match the load requirements. 1120nm is the band-gap wavelength of silicon.

The concentrated light striking the glass tube is spectrally separated into different bands in two stages: (1) much of the infra-red band ($> 1120nm$) is absorbed by the liquid in the channel and (2) the UV-Vis. band shorter than λ_{vis} is absorbed by the long pass filter. The energy absorbed in the long pass filter is transferred into the moving liquid by conduction and convection. Separating the spectral beam splitting process into two stages can potentially lead to lower cost and substantially better integrated configurations.

The light transmitted through the borosilicate tube is guided to the Si cells by two side reflectors which are made of highly reflective (90% solar reflectance) solar grade mirrors. The volume confined by the mirrors, Si cells, and the borosilicate tube is filled with an optical grade silicone encapsulant, serving as an optical coupler. This minimises the reflections from different refractive surfaces which subsequently increases the optical efficiency of

the receiver. It also creates a good optical match for the Si cells, which have AR coating designed for encapsulation. Alternatively, an air gap can be inserted within the bulk of the silicone in order to reduce the transfer of heat from the thermal channel to the solar cells. This introduces additional optical losses by reflection at the two surfaces of the gap, and detailed modelling of particular designs is required to determine the best configuration.
Although photons in the wavelength range $\lambda_{vis} - 1120nm$ are converted into electricity at a relatively high efficiency, there is still significant heat generated in the cells in concentrating systems. This heat is conducted from the cells to the aluminium PV cooling channel and transferred into the low temperature stream.
The PV cooling channel component is similar to traditional hybrid PV-T collectors since it is thermally coupled to the PV cell. By operating the PV cells at temperatures below 80°C, a useful medium temperature thermal output can be acquired from the PV cooling channel without considerable loss of PV performance. However the main thermal output at high temperatures is produced by the long pass filter-liquid combination. This channel is thermally decoupled from the solar cells. All non-illuminated faces of the receiver are insulated to reduce heat loss. The cost effective candidates for the long pass filter and heat transfer fluid are discussed in the next two sections.

5.1.1 Semi-conductor doped glass filter

The spectral filtering method described in this chapter comprises a SDG filter in conjunction with a direct absorption volumetric heat transfer liquid. It is shown here that the combination of these two can act as a band pass filter for Si solar cells.
Incorporating thermally developed micro-crystalline structures (as small as 10 nm) of CdS_xSe_{1-x} and $CdTe$ as dopants in a glass matrix can create edge filters with very sharp cut-off wavelengths in the visible and infra-red range respectively [160]. The concentration of the dopant crystals is usually less than 1 vol.% [160, 161]. This means that the cost of material in these filters is relatively low. The steepness and location of the absorption edge of SDGs can be tuned in the “striking” phase of the fabrication process which is thermal process in which the temperature of the filter is varied in a controlled way during the cooling period.
Spectral filtering of sunlight by selective absorption using volumetric filters has significant advantages over wave interference filters, including:

1. Ease of manufacture and low cost
2. Sharp absorption edge coinciding with the semiconductor band gap

3. No variation in optical properties with angle of incidence

4. High absorption in the short wavelengths that makes them suitable thermal absorbers

The external transmittance of a set of SDG filters with cut-off wavelengths between 600 nm and 720 nm is shown in Figure 5.2. The external transmittance of the measured filters at 800 nm (an indication of IR transmittance) is between 88.5% and 91.7% which includes reflection losses. Since the refractive index of silicate glass matrix is 1.52, the internal transmittance of the filters can be as high as 98%. This is an important consideration because by employing optical coupling between the SDG filter and the other components in the receiver, the reflection losses from the SDG filter can be reduced. In this way, high transmission in infra-red wavelengths can be expected.

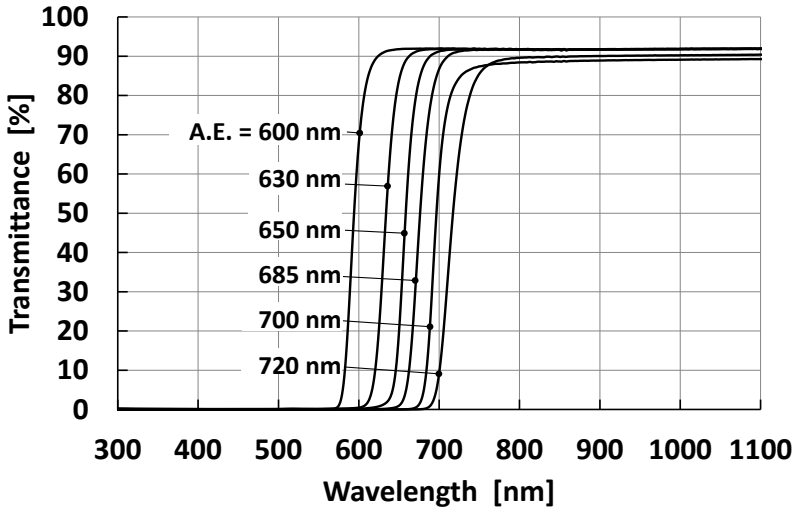

Fig. 5.2 The external spectral transmittance of 2 mm thick SDG filters in air with different absorption edges (A.E.); measured by Lambda 1050 UV-Vis-NIR spectrophotometer

The optical non-linearity and the sharpness of the absorption edge of SDGs are mainly due to the band filling phenomena in the semiconductor dopant (CdS_xSe_{1-x} or $CdTe$). Since these filters are considered for selective optical-thermal absorption in this research, it is important to investigate the luminescence, darkening, and absorption saturation effects on their spectral transmission characteristics.

Luminescence: Two types of luminescence peaks have been observed in SDGs: one at about the band gap energy of the semiconductor which is actually the absorption band of the SDG

and the other at a lower energy in the transparent spectral region, with wavelength longer than the absorption edge. The luminescence efficiency of a SDG with an absorption edge of 570 nm (OG 570) was estimated to be as low as $\sim 1\%$ [162]. This value decreases as the absorption edge moves to longer wavelengths, mainly because of strong absorption in the filter [160]. Since the required cut-off wavelength for Si cells is between 600 nm and 750 nm, it seems that this effect is not problematic.

Absorption saturation: In the case of absorption saturation ("filter bleaching"), photons with wavelengths shorter than the absorption edge of the original filter can transmit to the Si cells, which is undesirable. SDGs show a "bleaching" effect at high illumination intensities. This means that at very high intensities, they are incapable of effectively absorbing all the photons in their absorption spectral region. At high illumination intensities, some photons will transmit through the filter, whereas they would have been absorbed at lower intensities. This can be described by band filling in the semiconductor. This is not significant until intensities reach levels as high as $1 MW/cm^2$ [162]. This is several orders of magnitude higher than the intensity levels in any solar concentrators.

Photo darkening: Unlike absorption saturation, photo darkening reduces the transmission of the filter for wavelengths longer than the absorption edge. Exposing SDG filters to high intensity beams reduces their transmission in their transparent spectral band. This prevents the wavelengths of interest for Si cells from reaching the cells. Photo darkening has been observed for very high intensities close to the saturation level. Hence, it seems that, similar to absorption saturation, this cannot be problematic for either linear or point focus solar concentrators.

Absorption edge shift: The absorption edge of SDG's shifts toward longer wavelengths with temperature. This is due to the decrease in the band gap energy of the semiconductor. On the basis of the data sheet provided by Schott [163], the temperature coefficients of filters with cut-off wavelengths in the range of 515 nm and 715 nm are 0.11 - 0.18 nm/K. Hence, in the design stage of the receiver, the filter should be selected based on the steady state operation temperature.

5.1.2 Selective absorption heat transfer fluid

Choosing a suitable fluid for the described receiver is a challenging task. Three candidates of chapter 4 have been considered here again but there might be other suitable fluids. Although there is abundant information on the physical and thermal properties of commercial heat transfer fluids, there is a shortage of knowledge about their optical properties. Physical and thermal properties of a range of such fluids have been provided in [62, 63]. Among

these fluids, water (H_2O), ethylene glycol (EG) ($C_2H_6O_2$), and propane-1, 2-diol (so called propylene glycol (PG): $C_3H_8O_2$) show suitable heat transfer and optical properties. Their optical and thermal properties are discussed here in relatively more details compared to the previous chapter.

Optical properties: as discussed in the previous chapter, the O-H bond in the molecular structure of these liquids give rise to strong absorption bands in the near infra-red which is desirable for absorbing the long wavelengths of the solar spectrum [164]. They show high transmittance in wavelength below 1120 nm and are almost entirely transparent in the visible range. The internal spectral transmittance of these three liquids is shown in Figure 4.7. The transmittance value in this graph is associated with a path length of 10 mm. As previously discussed, a high transmittance is required for wavelengths in the band-pass between 600 nm and 1200 nm.

Water shows a dip in transmission at about 980 nm which is undesirable as it corresponds to the high efficiency band for Si cells. This absorption band is weaker for both PG and EG. However, above 1200 nm water has a higher absorption coefficient; its transmittance peak at 1,260 nm doesn't exceed 34% whereas PG and EG have a peak transmittance of 70% and 64% respectively at about 1300 nm. This causes a loss in the thermal component of the system because a fraction of sunlight within 1200-1400nm band transmits to the cells. These losses will be quantified in the following sections.

Among these fluids, ethylene glycol is relatively toxic and doesn't show any optical advantage over propylene glycol which is non-toxic and is also already being used as a heat transfer fluid. So ethylene glycol was excluded from further consideration.

The refractive index of the same liquids are shown in Figure 5.3 [58]. Propylene glycol and ethylene glycol show higher refractive indices ($n_{glycols} \sim 1.43$) relative to water ($n_{water} \sim 1.33$) which is another advantage of glycols over water in the proposed design. A fluid refractive index close to the refractive index of the borosilicate glass tube ($n_{glass} \sim 1.47$) and SDG filter ($n_{SDG} \sim 1.52$) leads to a better optical coupling between these layers and consequently reduces Fresnel reflection losses.

In the methods section it is explained how the ray tracing and experimental models have been set up to evaluate the theoretical and experimental performance of the proposed design to achieve suitable spectral beam splitting for Si solar cells.

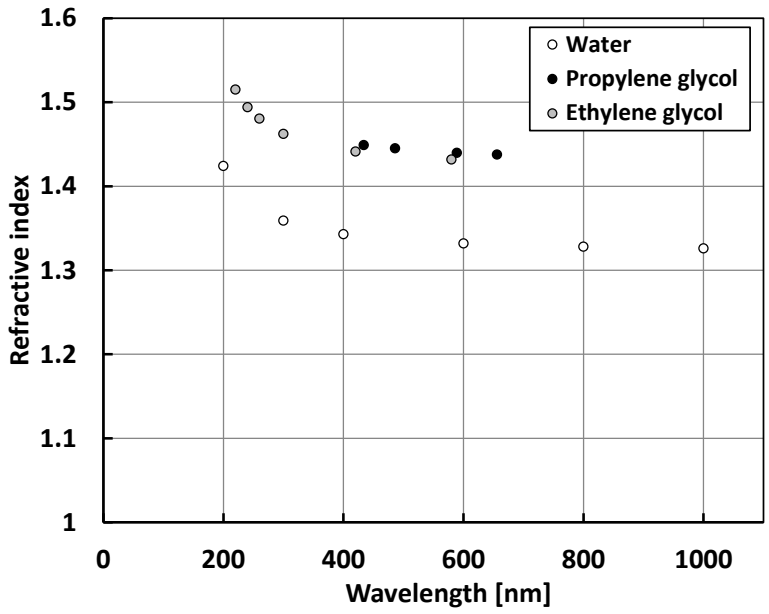

Fig. 5.3 The refractive index of water, propylene glycol, and ethylene glycol

5.2 Methods

The optical performance of the proposed design was investigated using two methods: (1) a detailed ray tracing simulation accompanied by a MATLAB model of the solar cell and (2) an experimental investigation using a sample filter.

5.2.1 Ray Tracing Analysis

Two sets of ray tracing analyses were conducted to study the proposed receiver design. Firstly a rectangular sample beam splitter, described in detail in the following sections, was simulated. Secondly, the actual proposed design that is depicted in Figure 5.1 was modelled. The purpose of modelling the rectangular sample was to test the efficacy of the combination of PG and SDG as an effective method to achieve a band-pass filter to deliver the expected spectrum splitting. The rectangular channel also made it simpler to minimise parasitic losses and unknown optical effects and collect measurement data that could be used to validate the accuracy of the ray tracing model. This model was then used to sim-

ulate the final cylindrical receiver design using the same ray tracing principles and parameters.

Modelling the rectangular channel

A schematic of the rectangular channel set-up is shown in Figure 5.4 in experimental investigation section. Ray-tracing software LightTools was used for this simulation. NBK-7 optical properties for the glass channel and PMMA for the Fresnel lens were defined. The properties of the Fresnel lens modelled in LightTools are tabulated in Table 5.1.
The optical properties of PG and SDG filters with nominal pass frequencies of 600 nm, 650 nm, and 700 nm, labelled HB600, HB650 and HB700 respectively (see section 5.1) were included. Having the spectral power together with the spectral response of the cell, the cell I_{sc} can be determined using Equation 5.1:

$$I_{sc} = \int_0^{4000nm} SR_\lambda \times P_\lambda \, d\lambda \tag{5.1}$$

where λ is wavelength, and SR_λ and P_λ are spectral response and spectral power respectively. Here the integration is performed over the entire solar spectral range of 0- 4000nm to determine the theoretical value of I_{sc}. The theoretical values obtained were compared against experimentally measured values from the identical configuration.

Table 5.1 Details of the Fresnel lens used in the ray tracing model

Focal length	150 mm
Groove pitch	0.3 mm
Aperture	283 mm
Material/thickness	PMMA/2mm
Approx.Spot Size/Width	8-10

Modelling the cylindrical receiver

After investigating the spectral splitting concept using the above method, the cylindrical receiver (Figure 5.1) was modelled in a ray tracing simulation under concentrated light. The concentrated light is supplied by a commercial parabolic trough designed and developed by NEP Solar. This trough has an aperture width of 1200mm and a focal length of about 645mm.

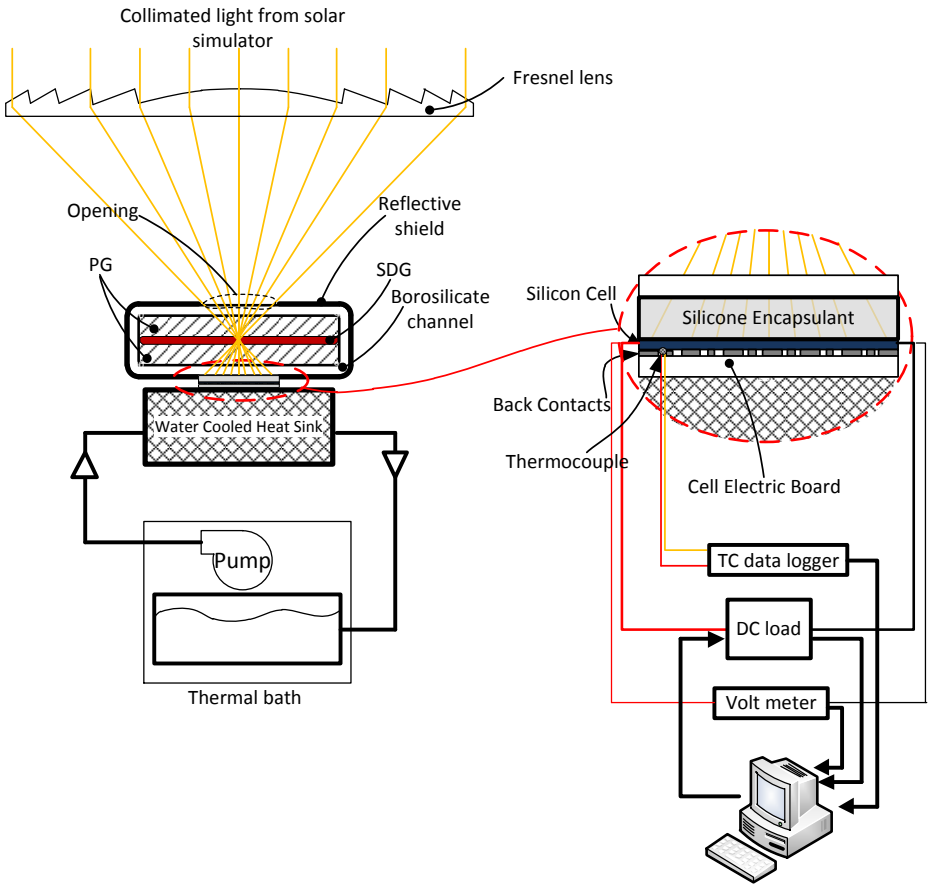

Fig. 5.4 The overall schematic of the experimental set-up to test the effect of different filters on the electrical performance of the PV cells; SDG: semiconductor doped glass; TC: thermocouple; PG: propylene glycol

Experimental investigation

A small sample receiver was prepared to verify the effectiveness of spectral filtering using a heat transfer liquid and SDG filters. A schematic of this experiment is presented in Figure 5.4. A rectangular borosilicate glass tube (ID: 10mm by 40 mm) arranged with the SDG filter suspended across its mid plane and then filled with PG was used. The thickness of the SDG filter was 2 mm, leaving 4 mm of PG on either side of the filter. SDG filters with three different nominal cut-off frequencies of 600 nm, 650 nm and 700 nm were used. The external spectral transmission for these filters were measured using a LAMBDA 1050 UV-Vis-NIR spectrophotometer; the results are shown in Figure 5.2.

The top and side surfaces of the channel were covered with a reflective shield with an opening on the top surface to allow a controlled amount of light to enter the receiver and reach the cell. The channel design allowed the SDG filters to be interchanged without changing the light

distribution on the entrance of the receiver. This is an important consideration as it allowed the cell output to be determined as a function of the filter cut-off wavelength independent of other parameters.

The PV cells were attached to the bottom side of the glass channel without any air gap in between. The cell itself has a silicone encapsulant on the front side. The cell area exposed to the light was 9mm by 24 mm. The cell is a high performance back contact solar cell with all n and p electrodes on the rear surface wired to an electronic board. This board was mounted on a heat sink made of a copper block containing an array of fins cooled by a running water stream. The temperature of the cell was kept at a fixed value for the different filters by using the heat sink. A Fresnel lens, made of PMMA with a focal length of 150 mm, was used to focus the collimated (within 1°cone angle) light generated by a SS150AAA solar simulator onto the receiver. The spectral distribution of the solar simulator is within $\pm 8.4\%$ of the standard ASTM G 173-03 in accordance with ASTM E927-10. A USB2000 spectrometer with a sensitivity of 1dB was used to measure the spectrum of the light before and after the Fresnel lens and verify that the lens had no influence on the spectral distribution of the light. A miniature k-type thermocouple was attached to the back of the silicon junction in the space between the back contacts to directly measure the junction temperature. A NI-9213 data acquisition card sampled and recorded the cell temperature. The aim of the temperature measurement was to ensure that the PV electrical data was measured at the same cell temperature for different SGD filters. The cell I-V curves were measured using a KIKUSUI plz 1004 DC load and a controller created in NI LabView. The DC load swept the current value from the open circuit voltage point to the short circuit point in variable step sizes. At low current, where dI/dV is large, a step size of 0.05 A was used. Close to the maximum power point, where dI/dV becomes smaller, the step size was switched to 1mA. The current values were measured by the DC load and reported to the data logging program. Cell voltage was measured using a 4-wire configuration and recorded with an NI-9207 data acquisition card. The voltage channel resistance of NI-9207 is greater than $1G\Omega$, hence the current flowing through it is less than 0.7 nA, considered here as negligible.

After recording the discrete I-V values, a single diode model was used to fit a curve to the data:

$$I = I_{ph} - I_s(e^{\frac{V+IR_s}{nV_{th}}} - 1) - \frac{V+IR_s}{R_p} \tag{5.2}$$

where, I: cell current (A), V: cell voltage (V), I_{ph}: photon generated current (A), I_s: diode saturation current (A), R_s: cell serries resistance (Ω), R_p: cell parallel resistance (Ω), n: diode ideality factor, V_{th}: thermal voltage. In order to fit this equation to the data, a MATLAB function was developed to find the optimum values for I_{ph}, I_s, R_s, R_p, and n by minimising the sum of the squared errors between the predicted and measured values of I and V. Since

there is uncertainty associated with current and voltage measurement, a Monte Carlo method was used to carry out an uncertainty analysis on the fitted curve. From this analysis the uncertainty in the curve-fit values of current and voltage are as follows:

$$U_I = \pm(0.2\%I_{read} + 0.03) \tag{5.3}$$

$$U_V = (0.52\%V_{read} + 0.0004) \tag{5.4}$$

where, U_I and U_V are current and voltage measurement uncertainties at 95% confidence level. I_{read} and V_{read} are the values displayed by the DC load and the NI-9207. Using these uncertainty intervals a normal distribution was defined for each measured I and V values corresponding to each point. Using these distributions a Monte Carlo analysis was conducted to fit a population of curves. The interception of these curves with the y-axis corresponds to I_{sc}. Hence the uncertainty range of I_{sc} is determined.

5.3 Results

The ray tracing results of the rectangular sample transmitted spectrum is presented in Figure 5.5a. The spectral response of the solar cells that have been employed in our measurements is also shown in Figure 5.5b. In this figure the transmitted energy has been presented for 4 different cases: bare cell without any filtering, and 3 different SDG filters combined with PG. As explained before, the I_{sc} of the cell exposed to these spectral distributions and with the cell response of Figure 5.5b were calculated . These have been summarised in Table 5.2.

Figure 5.6 shows the IV curves acquired from the measurements for 4 different cases: (1) without any filtering (bare cell), (2) with HB600+PG, (3) with HB650+PG, and (4) with HB700+PG. The cell temperature during the measurements was kept between 37°C and 38.5°C. The bare cell is the reference point to compare the cell performances with different filtering. A comparison of the I_{sc} for each of these cases, known to be a very good indicator of the photon flux density on solar cells, is listed in Table 5.2.

The short circuit current values, I_{sc} , were normalised using the bare cell short circuit current, $I_{bare\ cell}$, for the corresponding case (measured/modelled). This approach was taken because the amount of light striking the front surface of the receiver was not measured, and so could not be matched for the model and the experiment. Despite this, the irradiance was kept constant for all the measurement cases.

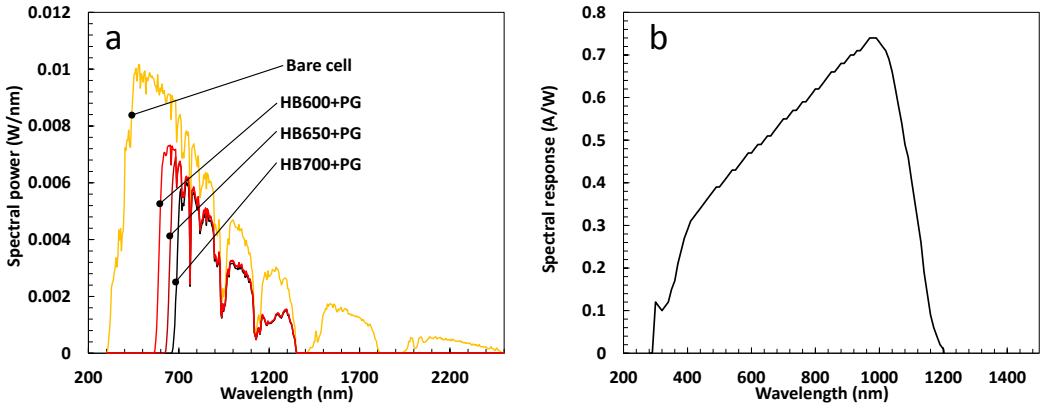

Fig. 5.5 (a) Ray tracing results of the transmitted light spectral distribution for the rectangular sample (Figure 5.4) tested using a solar simulator; (b) The spectral response of the Si solar cell used in this study

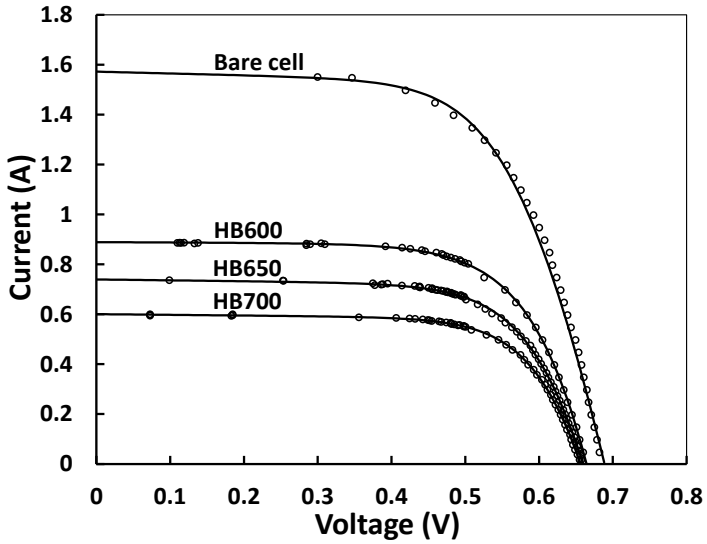

Fig. 5.6 The *IV* curves of the cell without any optical filter (bare cell), with HB600+PG, with HB650+PG, and with HB700+PG

Table 5.2 Values of measured and modelled I_{sc} for different SDG filters; values in bold have been normalised with respect to the bare cell I_{sc} in the same column

Filtering	Measured		Modelled	
	$I_{sc}(A)$	$I_{sc}/I_{bare\ cell}$	$I_{sc}(A)$	$I_{sc}/I_{bare\ cell}$
Bare cell	1.57 ± 0.04	1	2.574	1
HB600 + PG	0.89 ± 0.04	0.57 ± 0.03	1.420	0.55
HB650 + PG	0.74 ± 0.03	0.47 ± 0.02	1.197	0.47
HB700 + PG	0.60 ± 0.02	0.38 ± 0.02	1.028	0.40

As is seen in this table, the modelled normalised I_{sc} values match the experimental values very well. Hence it can be said that the ray tracing model developed for this analysis has acceptable accuracy in predicting the optical performance of the proposed filter.
The uncertainty of the I_{sc} ratios was calculated using the following method:

$$R = \frac{I_{sc}}{I_{bare\ cell}} \tag{5.5}$$

$$U_{95} = 2[(\frac{\partial R}{\partial I_{sc}} s_{I_{sc}})^2 + (\frac{\partial R}{\partial I_{bare\ cell}} s_{I_{bare\ cell}})^2]^{1/2} \tag{5.6}$$

where, U_{95} is the uncertainty band with 95% confidence level and s is standard deviation.

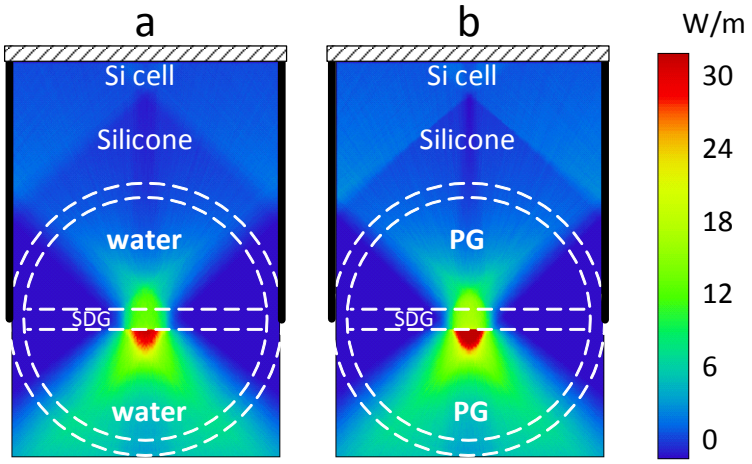

Fig. 5.7 The light power propagating through the receiver filled with (a) water, (b) PG; the values are in Watts per meter length of the receiver

The ray propagation pattern inside the receiver filled with water and PG is shown in Figure

5.7. It should be noted that this geometry will be considered for building the prototype and the experiential section of the thesis. The focal point of the optics is positioned, by design, on the bottom surface of the SDG filter in order to allow the narrowest receiver possible. As a result, the maximum intensity of light can be seen to occur at the front surface of the SDG filter. A large portion of light is absorbed in the SDG filter and the intensity of light rapidly drops across the front face of the SDG. This point is clearly illustrated in Figure 5.8, which presents the absorbed intensity instead of the propagating intensity. For clarity and contrast of the contour, note that a logarithmic colour bar has been used in this figure.

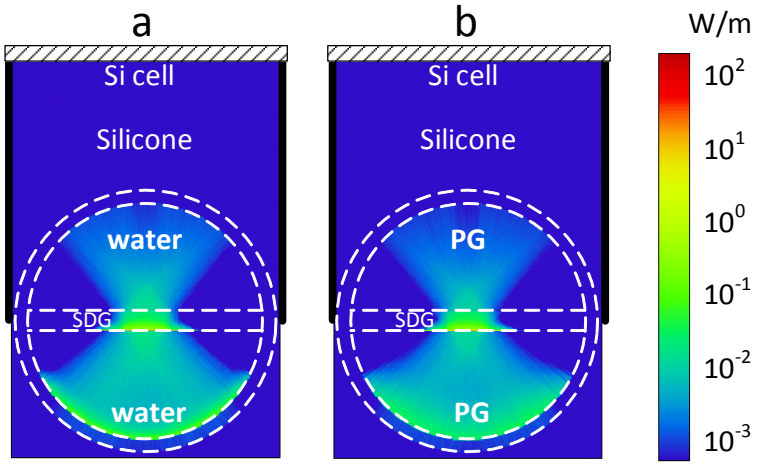

Fig. 5.8 Light power absorbed within the receiver in Watts per meter length of the receiver when filled with (a) water and (b) PG. For improved contrast the contours are presented using a logarithmic scale.

The proportion of the incident light reaching each component within the receiver is presented in Table 5.3. A total of 4.4% and 3.8% of the light is reflected back from the receiver respectively for PG and water as thermal fluids. This is mainly due to the Fresnel reflection from the bottom face of the borosilicate tube. The reflection loss is less for PG than water due to the closer refractive index match with the SDG and borosilicate glass. The side mirrors and silicone encapsulant also contribute to the optical losses by absorbing 2.5% and 2.9% of light in two cases.

A total of 23.5% and 29% of the light striking the bottom face of the borosilicate tube reach the PV cells for the water and PG cases respectively. This result is expected as the total transmission of water is lower than that of PG in solar spectrum range. The spectral distribution of this intensity on the cells is of primary importance. Figure 5.9 presents the

spectral distribution of light on the cells for both water and PG in combination with a HB700 SDG filter compared to the ideal filtering.

Table 5.3 The ray tracing analysis of the receiver identifying the intensity of light reaching each component

Component of light	Water	PG
Striking the glass tube	100%	100%
Reaching PV cells	23.5%	29%
Reflected missed rays	4.4%	3.8%
Absorbed by thermal fluid	27.7%	22%
Absorbed SDG Filter (HB700)	41.9%	42.3%
Absorbed by reflective walls and silicone	2.5%	2.9%

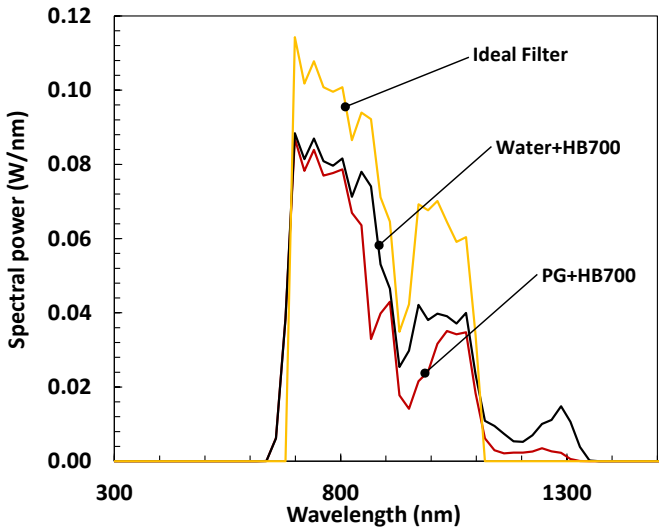

Fig. 5.9 Spectral distribution of light reaching the PV cells with water and PG as the thermal fluid. Due to the negligible spectral power present for wavelengths beyond 1500nm, these wavelengths have been suppressed for clarity.

Here “ideal filtering” means that all the radiative energy in 700-1100 nm band (as suggested by Crisostomo et al. [165]) is directed to the cells without any losses or inaccuracies. The light transmitted to the cells has a drop at around 900-1000 nm which is more prominent in the water filled tube than the PG filled tube. This is due to the higher OH absorption of water

in this band as discussed before. The transmitted light in the water filled tube is higher for the wavelengths longer than 1100 nm since water has a higher absorption compared with PG. In order to quantify the difference between the two spectral curves of Figure 5.9, the PV conversion efficiency was calculated under these two illumination distributions using the approach discussed in section 5.2.1. Results indicate 65.5% and 77% of the power in the spectral band 700-1100 nm reaches the PV cells for the water+HB700 and PG+HB700 receivers respectively. Under these conditions the PV cell generates 64% and 77% of the ideal I_{sc} respectively. It should be noted that I_{sc} takes the spectral distribution of the light into account and therefore doesn't necessarily follow the power ratios. This reveals that from an optics point of view PG is more suitable than water as a thermal fluid for spectrally splitting hybrid receivers utilising liquid filters. An additional benefit is that PG has a higher boiling temperature (approx. 188°C) that allows for fluid temperatures in excess of 100°C without the need for pressurisation.

For the two cases, 41.9% and 42.3% of the total flux is absorbed by the SDG filter for the water and PG cases respectively. By adding the fraction of energy absorbed by the thermal fluids, the total amount of energy absorbed in the high temperature channel is 69.6% and 64% respectively. However, the additional fraction of energy absorbed by the water-SDG combination comes at the expense of lower electricity generation via PV.

From the optics point of view, the sharp spectral beam splitting achieved by the SDG filter at the lower bound of the PV pass band (around 600 nm to 700 nm) is advantageous, although a "soft" edge does not lead to large losses since most of the light is absorbed in either the electrical and thermal absorbers irrespective of the band edge. As previously noted, the thermal fluid demonstrates reasonable optical performance but deviates from the ideal requirements. More research on the optical properties of existing liquids or synthesising more suitable ones is required in order to improve the absorption-transmission characteristics of the filter in IR range.

A comprehensive treatment of the heat transfer and simulated thermal efficiency of the current beam splitting receiver design are presented in [166]. For the nominal design conditions of 150°C outlet temperature for the primary thermal channel, and 60°C for the secondary thermal channel (PV cooling) thermal efficiencies of approximately 50% for the primary hot channel and 85% total (primary and secondary fluid streams) were predicted. However, the computational heat transfer simulations revealed that the receiver thermal efficiencies are strongly correlated to the external wind velocity.

The direct absorption receiver introduced in this chapter has a superior performance over the receiver design of the previous chapter that used wave interference filters instead of SDG. In order to verify the performance of the this receiver, both optical and thermal, a full scale

prototype was fabricated and mounted onto a parabolic trough concentrator with an aperture width of 1.2m and a trough length of 2m. This is covered as the experimental section of this thesis in the next chapter.

5.4 Summary

In this chapter, a new configuration was proposed for concentrating hybrid PV-T receivers for linear solar concentrators. The proposed design uses semiconductor doped glass and a thermal fluid to spectrally split the light between a high temperature thermal absorber and silicon PV cells. Using ray tracing the optics of the system was investigated and it was shown that propylene glycol outperforms water as the suitable thermal fluid for this purpose, by directing 77% of the light in 700 nm-1100 nm spectral range, which is the optimum band for Si cells in PV-T receivers. It was shown that the combination has low reflection losses due to efficient optical matching between the optical components.

Chapter 6

Experimental analysis of the spectral beam splitting receiver

---

The content of this chapter has been published as a journal article:
Cameron Stanley, Ahmad Mojiri, Mirza Rahat, and Gary Rosengarten. “Performance testing of a spectral beam splitting hybrid PV-T solar receiver”. In: *Applied Energy 169*(2016)

In this chapter, the volumetric receiver design with PG and SDG, introduced in chapter 5, has been experimentally investigated in an outdoor measurement. The receiver depicted in Figure 5.1 was built and tested on a commercial parabolic trough. The flux mapping method introduced in chapter 3 was used to size the receiver for this specific concentrator. In the end, the measured data has been reported and analysed against the expected values and the discrepancies have been discussed. Possible pathways to improve the system performance for future work has been outlined.

6.1 Experiment description

The schematic of the receiver that was used in the experiment has been shown in Figure 5.1. The general aspects of this design have been explained in the previous chapter, however more details on fabricating the experimental one are presented here. The receiver was designed and built for a commercial parabolic trough, Polytrough 1200, manufactured by NEPSolar.

6.1.1 The concentrator

Polytrough 1200 has an aperture width of 1200 mm equipped with a single axis tracking controller. The controller operates based on a sun tracking algorithm that needs the location and trough axis orientation to be known. The main mirror is made of MIRO-SUN 90 manufactured by Alanod laminated on a composite substrate and has a focal length of about 650 mm. The important dimensions of the mirror have been listed in Section 6.1.3.

6.1.2 Sizing the receiver

As it has been mentioned before, the first step to design and build the receiver is sizing it with respect to the optics of the concentrator. To do so, the method introduced in chapter 3 was used to map and measure the flux width of the trough.

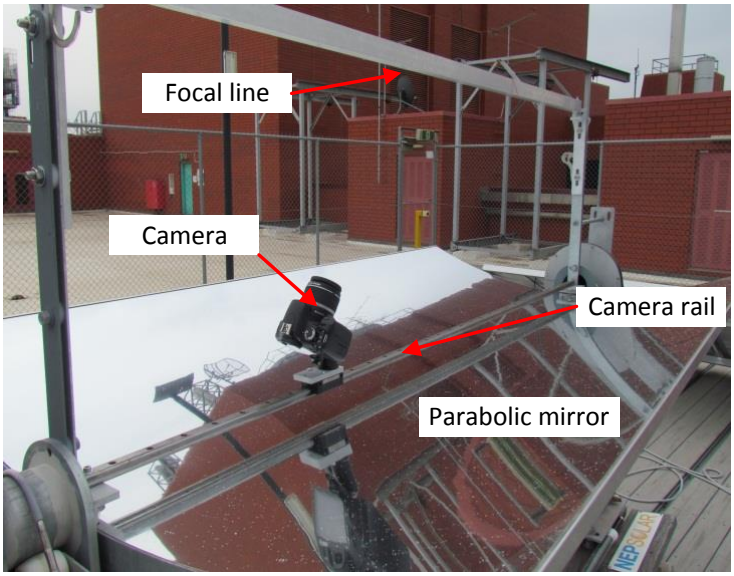

Fig. 6.1 The camera set-up for radiometric flux mapping on NEP Polytrough 1200

The camera that has been used in this experiment is Canon EOS 450D with a CMOS sensor. 0.5 mm-thick Gore diffuse reflector was used as the reflective target at the focal region. This material is highly Lambertian with reflectance of over 96% for the spectral range of up to near IR.
A camera mounting rail was installed along the axis of the trough, approximately 30mm

above the mirror surface (see Figure 6.1). Before capturing the flux image, a check board was located at the corresponding focal position. After capturing the image from the check board, the diffuse reflector was located at the same place. In order to avoid saturation on the sensor, the amount of light going into the camera was decreased by a neutral density filter. Camera setting for the two images is presented in Table 6.1. The focal length was kept the same in order not to change the geometrical characteristics of the optics. The minimum value of ISO was used to minimise the sensor noise.

Table 6.1 Camera settings for the flux mapping measurement

Parameter	Check board Image	Flux image
f-stop	$f/22$	$f/9$
Focal length	20 mm	20 mm
ISO	100	100
Exposure Time	$1/40$ sec.	$1/50$ sec.
Image stabiliser	On	On
Neutral Density Filter	Off	On

A sample result at a specific location along the focal axis is presented in Figure 6.2. Similar measurements were taken at four different locations on the axis. For the sake of brevity, they haven't been repeated here. These measurements showed that NEP Polytrough 1200 mm concentrates light onto a narrow strip of approximately 20mm.

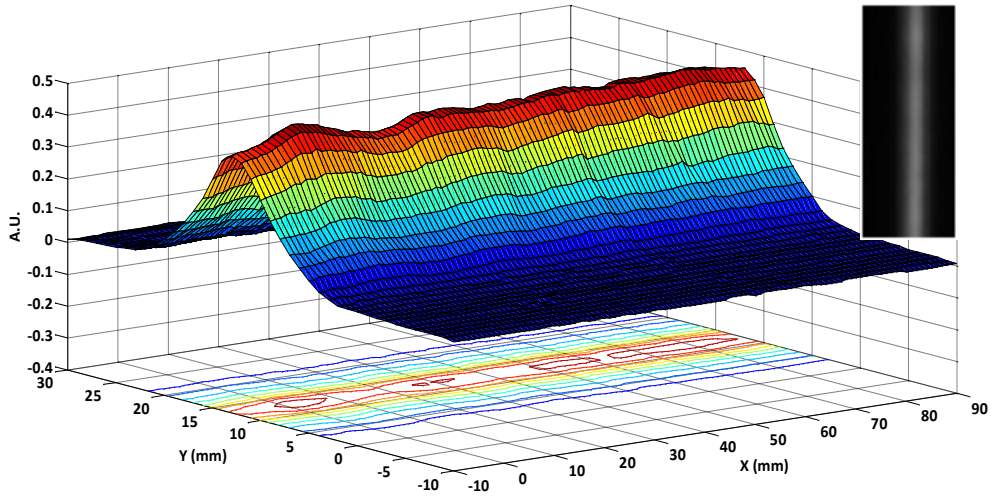

Fig. 6.2 The mapped flux of NEP Polytrough 1200 using close range radiometry

Figure 6.3 presents the cumulative energy fraction of the flux distribution as a function of the receiver width (assuming a flat receiver) for a representative location along the collector. The purpose of this measurements and calculation is to determine the variation of the energy intercepted by the receiver with respect to its size. The analysis on a flat receiver was carried out since the actual receiver in the proposed hybrid receiver is the rectangular flat SDG filter. Based on this figure, a 20 mm flat receiver captures 92% of the incoming total flux from the mirror. This corresponds to 60 times of geometrical concentration. Assuming 90% reflectance for the mirror, it can be said that the geometrical concentration ratio on the 20 mm-receiver is 49.7 times. Some energy is observed beyond the 20 mm strip which can be due to scattering and circum-solar radiation.

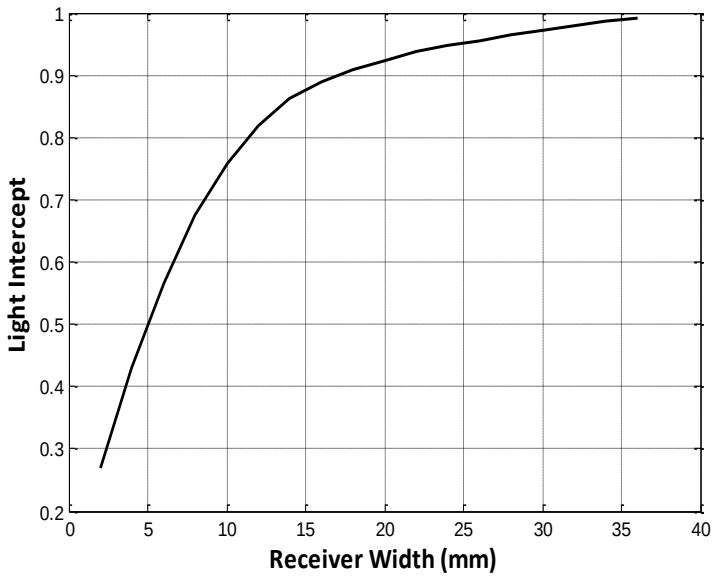

Fig. 6.3 The cumulative flux on a flat receiver at the focal region of NEP Polytrough 1200

The longitudinal non-uniformity along the focal line can stem from surface perturbations on the mirror. This distribution is more important in concentrating photovoltaic receivers mounted on parabolic troughs. Such distribution can result in a current mismatch of the cells connected in series that can reduce the overall efficiency or even damage the cells. Despite the observed deviations in the axial flux maxima, the longitudinal variation of flux (calculated on sections perpendicular to the receiver axis) is within ±14%.

6.1.3 The receiver

The receiver for the outdoor measurement was fabricated based on the schematic presented in Figure 5.1. The glass tube used in this receiver was purchased off-the-shelf and was made of borosilicate which is resistant to high temperatures. In order to have a 2 m single piece tube to install on NEP Polytrough 1200, two 1.5 m long tubes were cut and thermally fused to each other. Both ends of the tube were toughened to withstand the structural load due manifolding.

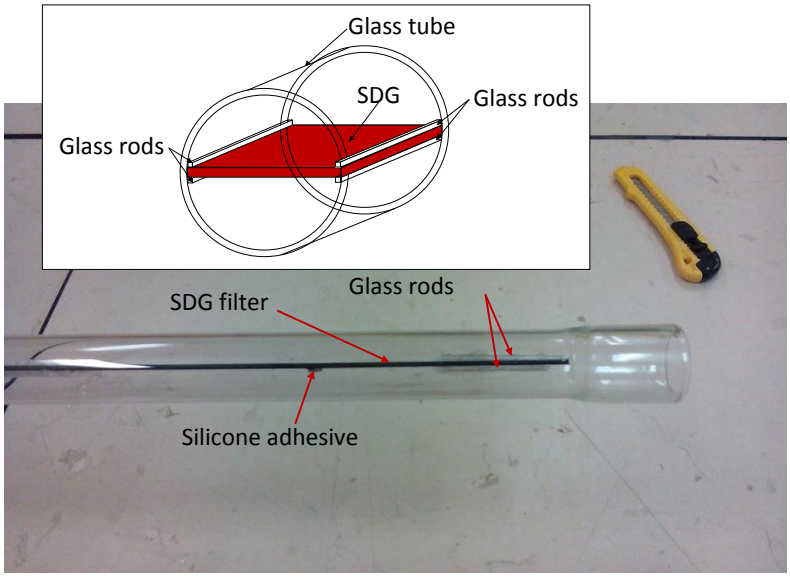

Fig. 6.4 Mounting SDG filters at the mid plane of the glass tube; a small amount of silicone adhesive as shown in the picture binds 2 consecutive filters together

A number of long rectangular glass pieces were glued to the internal wall of the tube to hold the SDG filters at its mid-plane. This has is in Figure 6.4. The thickness of these glass pieces is about 1.4 mm which is expected not to interact significantly with the fluid dynamics within the glass tube. The SDG filters were slipped through the gap between the glass pieces and held against each other using a high temperature silicone adhesive. The SDG filters used in this measurement had a cut-off wavelength of 700 nm (HB700). Their dimensions are listed in Table 6.2. At the time of building this prototype, 100 mm long filters were easily available off-the-shelf however, longer filters are more suitable for a practical receiver and can be sourced from other manufacturers. As a result of the filters bisecting the tube cross-section, two separate flow pathways are created. This reduces the Reynolds number to the laminar regime.

The width of the SDGs were chosen to be 24.6 mm which was the maximum size that matches the solar cells. In the proposed configuration, the width of the solar cell array in the receiver imposes the dimensional limit on the SDG filters i.e. the filters can't be wider than the cell width otherwise the glass tube won't fit in the aluminium extrusion which is made according to the width of the cells. As it was mentioned before, based on the radiometric measurements, more than 92% of the flux is within a 20 mm wide strip along the receiver. A slightly wider (24.6 mm) filter was used to accommodate some of the tracking errors and misalignment.

Table 6.2 Receiver and concentrator dimensions

Dimension	Value
Primary thermal absorber internal diameter, D_i (mm)	25.2
Borosilicate tube wall thickness, t (mm)	1.4
PV cooling channel internal diameter, d_i (mm)	11.5
Primary absorber hydraulic diameter, D_{hyd} (mm)	14.2
PV cell width, w_{PV} (mm)	27.5
PV cell length, l_{PV} (mm)	9.6
Number of PV cells per module	30
Number of PV modules per receiver	6
Total receiver width, W_r (mm)	50
SDG filter width, w_f (mm)	24.6
SDG filter thickness, t_f (mm)	2.0
Individual SDG filter length, l_f (mm)	100
Parabolic trough aperture width, w_{ap} (mm)	1200
Parabolic trough length, l (mm)	2000
Parabolic trough focal length, f_p (mm)	650
Geometric concentration ratio, CR (-)	≈ 42

The glass tube is attached to the aluminium channel using a layer of Elastosil silicone encapsulant. This layer of silicone is encased with the two side mirrors made of Alanod MIRO-SUN 90, which guides the light transmitting through the glass tube towards the solar cells that are attached to the internal side of aluminium extrusion (see Figure 6.5). A small gap of about 0.5 mm was maintained between the glass tube and the mirrors to avoid a thermal bridge between them. The heat transferred to the side mirrors which are made of aluminium can easily be transmitted to the aluminium extrusion and lost to the cooling flow at the top of the extrusion.

The top side of the extrusion was insulated with polystyrene foam, however to prevent the

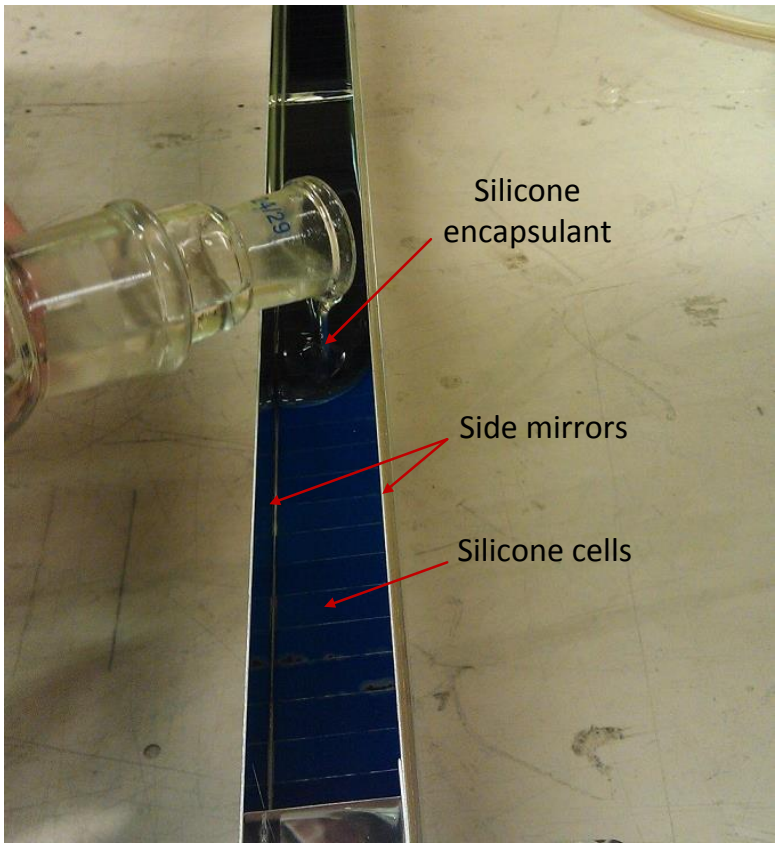

Fig. 6.5 The aluminium extrusion holding the cells. Silicone encapsulant is poured on top of the Si cells and between the side mirrors. This layer optically connects the glass tube to the solar cells

foam from being exposed to extreme temperatures that can melt the foam, a strip of fibreglass ribbon was placed between the foam and the aluminium extrusion. The external face of the foam was covered with aluminium reflective tape to protect the foam from direct concentrated radiation which can strike the foam when the receiver is slightly off the tracking position.
The integrated cooling channel at the top of the aluminium extrusion absorbs the rejected heat from the Si cells and delivers it as a secondary useful thermal output at a lower temperature. The operating temperature of this channel which is cooled by water was kept below 80 °C. This is imposed by the maximum recommended operating temperature of the Si cells used in this receiver.
The pink-dyed, corrosion inhibited Propylene Glycol (PG) by Bracton (>95% propane-1,2-diol, water, corros. inhib.) used in this receiver has long term stability with reasonably good heat transfer properties. The important properties have been listed in Table 6.3. The high boiling point of this liquid allows for low pressure operation of the glass receiver at tempera-

tures above 100°C. In order to quantify the degradation effects on the optical transmission of PG, a fresh and aged sample (after 3 months operation), were measured and compared against each other in Figure 6.6.

Table 6.3 The properties of PG at 25°C

Specific heat, C_P (kJ/kgK)	2.51
Density, ρ (kg/m^3)	1034
Dynamic viscosity, μ $(mPa.s)$	48.6
Thermal conductivity, k (W/mK)	0.206
Boiling point, T_b (°C)	155
Price, AUD/kg	$\approx$ 2.50

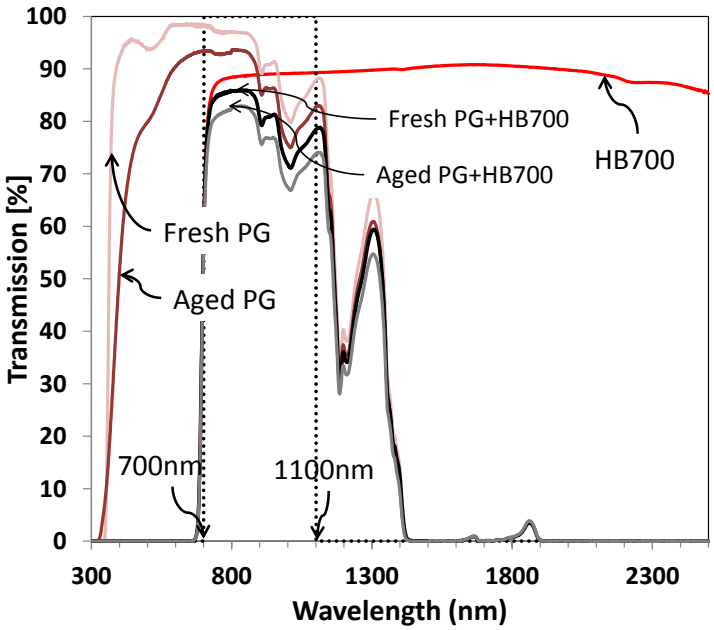

Fig. 6.6 Spectral transmittance of propylene glycol (Fresh and aged - 3 month field service) and 700 nm cut-off wavelength SDG filter (HB700). The transmission of the SDG-PG combination is also presented.

6.1.4 PV component

The PV component installed in the experimental receiver was designed and fabricated by the Centre for Sustainable Energy Systems in the Australian National University (ANU). It consists of two PV modules connected to each other in parallel. Each PV module has 3 PV sets wired in series. Each set is made of 30 individual cells interconnected in series through an electronic board. The Solar cells are a modified version of Sunpower solar cells with an efficiency in the range of 22-24%. In order to modify the actual cells for this application, the high efficiency back contact mono-crystalline cells were diced to 27.5 mm long and 9.6 mm wide pieces. The cell aspect ratio was optimised to reduce edge recombination losses, cell interconnect resistance, and cell to board thermal expansion matching. Then the small cells were positioned laterally in an array along the receiver on an electronic board. Hence the width of the PV receiver is equal to the cell length. Each board consisting 30 cells has a length of about 300 mm (see Figure 6.7). This was carried out by the Centre for Sustainable Energy Systems in the Australian National University and the final product was supplied to the RMIT solar lab.

Every 6 cells are connected to a one bypass diode. If a current mismatch above a certain threshold happens between the cells, the bypass diode is activated and 6 cells will be removed from the circuit. The bypass diode activation adds a voltage drop of almost one solar cell which means that once a diode is activated the voltage of about 7 cells will be lost.
The PV boards were glued to the internal face of the U-shaped aluminium extrusion using a thermal adhesive; due to the minute thickness of this layer, the heat generated in the cells is expected to conduct to the aluminium extrusion without significant resistance.

6.1.5 System performance testing rig

The outdoor performance measurement test was conducted at RMIT University's solar thermal lab at city campus in Carlton, Australia (Latitude -37°48' 20.0844", Longitude 144°57' 56.163"). The trough was installed in the east-west orientation which means that the tracking mechanism was tracking the sun in the north-south direction. This direction was selected to allow for a window of close to normal irradiation on the concentrator. Data was collected on a few clear days from 02 February 2015 till 31 March 2015. The prototype hybrid receiver was installed on NEP Polytrough 1200 and a high pressure high temperature test rig was used to measure its performance. A schematic of the test rig is shown in Figure 6.8.
The high temperature rig was designed to feed liquids such as PG at specific temperatures and flow rates into thermal receiver and measure the required thermal parameters for estimating

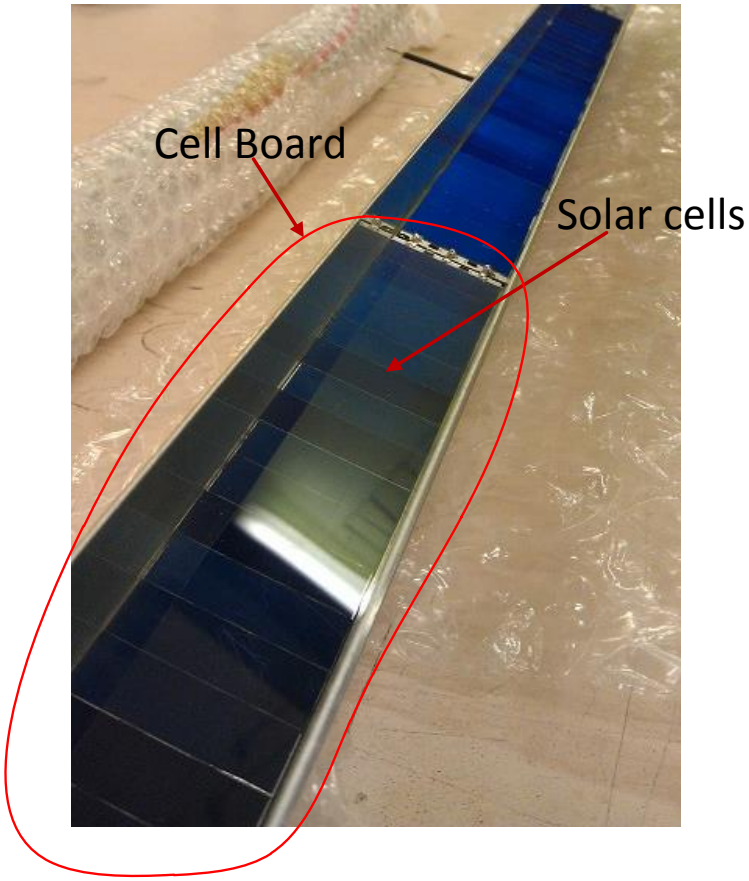

Fig. 6.7 The PV component of the receiver; each board consists 30 cells. The boards are located along the receiver onto the extrusion channel

the overall heat gain and thus efficiency. Different components of the rig were controlled by a Labview program specifically designed for it. A high temperature variable speed pump was controlled using a virtual PID controller within the program to set the flow rate at any value between 0.05 and 0.2 kg/s. The mass flow rate was measured using a micro Coriolis flow meter. The uncertainty of the flow rate was about $\pm 0.5\%$.

A 4-kW in-line heater, in the test rig was used to control the receiver inlet temperature to within 0.1 °C. The extra heat absorbed by the receiver was rejected to the ambient through a cooling system consisting of a liquid-liquid heat exchanger and a radiator equipped with a variable speed fan. The inlet and outlet temperature of the hot channel and the PV cooling channel was measured with a PT100 RTD which had been calibrated to an accuracy of 0.12 °C. The test rig was able to deliver liquid flow at temperatures of up to 200 °C.

A thermal expansion chamber was installed in the circuit to prevent the fluid system from pressurising at elevated temperatures. Another chamber was designed and installed in the

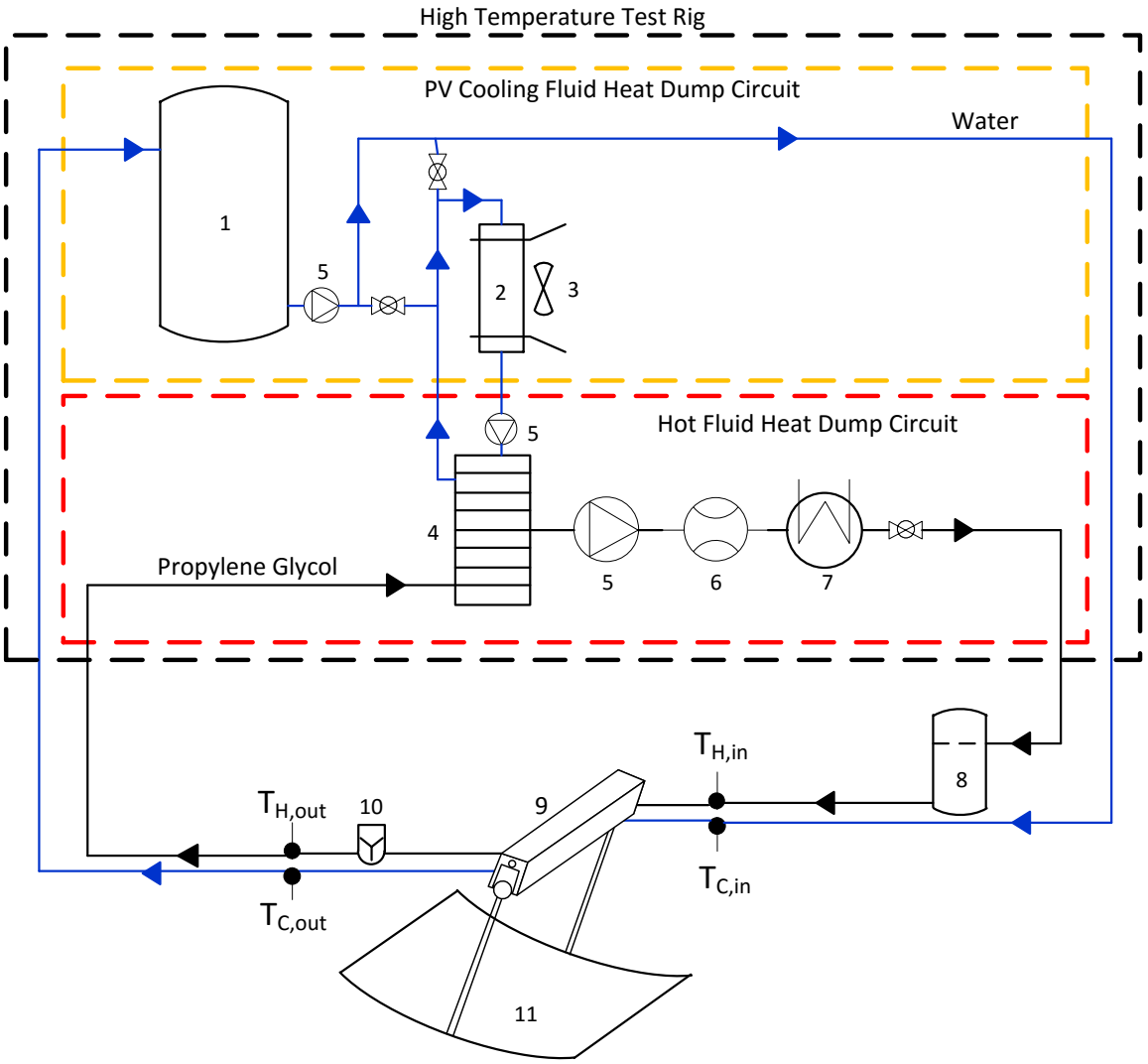

Key:

1. Water Tank
2. Air/water heat exchanger
3. Variable speed fan
4. Plate heat exchanger
5. Variable speed pump
6. Coriolis flow meter
7. Electric heating element
8. Bubble chamber
9. Hybrid PVT receiver
10. Static flow mixer
11. Parabolic trough mirror

Fig. 6.8 Experimental test set-up

circuit to collect the trapped air in the system and remove it. The water stream to the PV cooling channel was supplied from a 200 L tank at a constant flow rate. However a heating mechanism was used to change the inlet temperature of this stream to the cooling channel and study its effect on the PV performance.

The solar radiation was measured using a pair of Middleton EQ08 First Class pyronometers installed on a 2-axis tracking system at the same location of the PV-T system. One pyronometer was shaded by a disc to measure the diffuse component of the sunlight. The other pyronometer measured the global radiation. By subtracting these two values, the beam radiation intensity was determined within an accuracy of 43 W/m^2. The ambient temperature and wind speed were measured using a weather station installed next to the test rig.

Additional equipment was added to the test rig to measure the electrical performance of the receiver. This includes two separate DC loads: Kikusui PLZ-1004W and Array 3711A. Both these DC loads were controlled by a Labview program to sweep the I-V curve in predefined intervals and find the maximum power point of the PV modules. Each DC load was connected to one PV module. Once the maximum power point of the module was determined, the DC load set the voltage at that point and let the PV module run at its maximum power. This cycle was repeated every 2 minutes.

Experimental data acquisition was performed using National Instruments (NI) DAQ modules controlled by LabVIEW software. Parameters monitored during testing included: primary absorber and PV cooling channel inlet and outlet temperatures, mass flow rates, ambient air temperature, wind speed, time of the day, and global and diffuse solar radiation. Data for all parameters were recorded at 3 second intervals. The time of the day was used to account for the effects of the cosine angle of the incident light relative to the aperture plane of the parabolic mirror during the data post processing stage.

Measuring the receiver outlet temperature needed further considerations. The direct absorption of the light by the liquid occurs mainly in the first few millimetres. Moreover, the light absorbed by the SDG filters is convected by the adjacent flow causing hot flow steam near the filters at the centre of the tube. In a turbulent flow, the natural mixing phenomena eliminates temperature gradients and thermal stratification within the fluid. However, the basic calculations showed that the Re number of PG flow varies from 63 at 25 °C to 3370 at 150 °C which means that the flow is mainly in the laminar regime. This makes measuring the outlet temperature challenging as the radial thermal gradients are large.

A small static mixing mechanism was built and installed immediately downstream of the outlet port. A schematic of this has been shown in Figure 6.9. The highly laminar and thermally stratified flow enters this mixer and is perturbed while being pushed through the relatively complex pathway. The result of this perturbation is expected to be a mixed flow

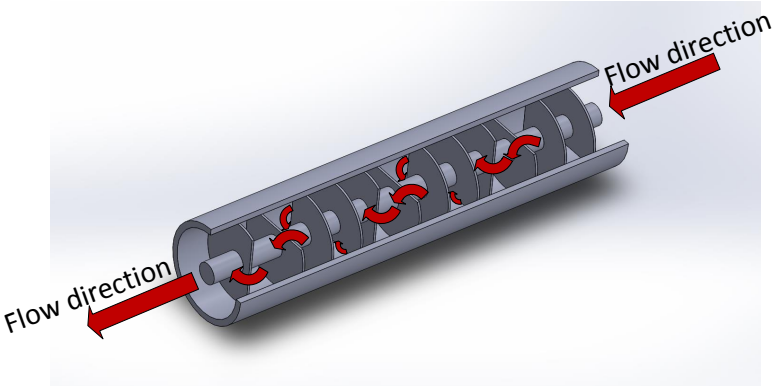

Fig. 6.9 The mixer mechanism to eliminate thermal stratification at the outlet of the receiver

with uniform temperature. After installing this mixer the RTD sensor was inserted into the flow exiting the mixer. By changing the location of the RTD tip, no measurable variation in the measured temperature was observed, which implied that the mixing mechanism was effective.

6.2 Results and discussion

The receiver prototype is shown in Figure 6.10. This was a 2m long receiver to be installed on NEP Solar's Polytrough at RMIT University. The installed receiver is presented in Figure 6.11.

Figure 6.12 shows a typical measurement acquired from the outdoor experiment explained in the previous section. The horizontal axis is local time; Australian Eastern Daylight Time (AEDT) – UTC/GMT +11:00. The vertical axis at the left is the inlet temperature to the high temperature channel, $T_{H,in}$, and the vertical axis at the right is the direct normal radiation which varies between 960 and 1000 W/m^2 during the period of this measurement. The inlet temperature was varied from 20 °C to 130 °C. 130 °C was selected as the maximum testing temperature because local boiling was observed inside the glass tube that could cause safety issues. The PV cooling channel inlet temperature, $T_{C,in}$, is also shown in this figure. This stream was held at a relatively constant temperature of between 19°C and 29°C over the period of the measurement. The temperature increase in this stream is mainly due to the ambient condition variation.

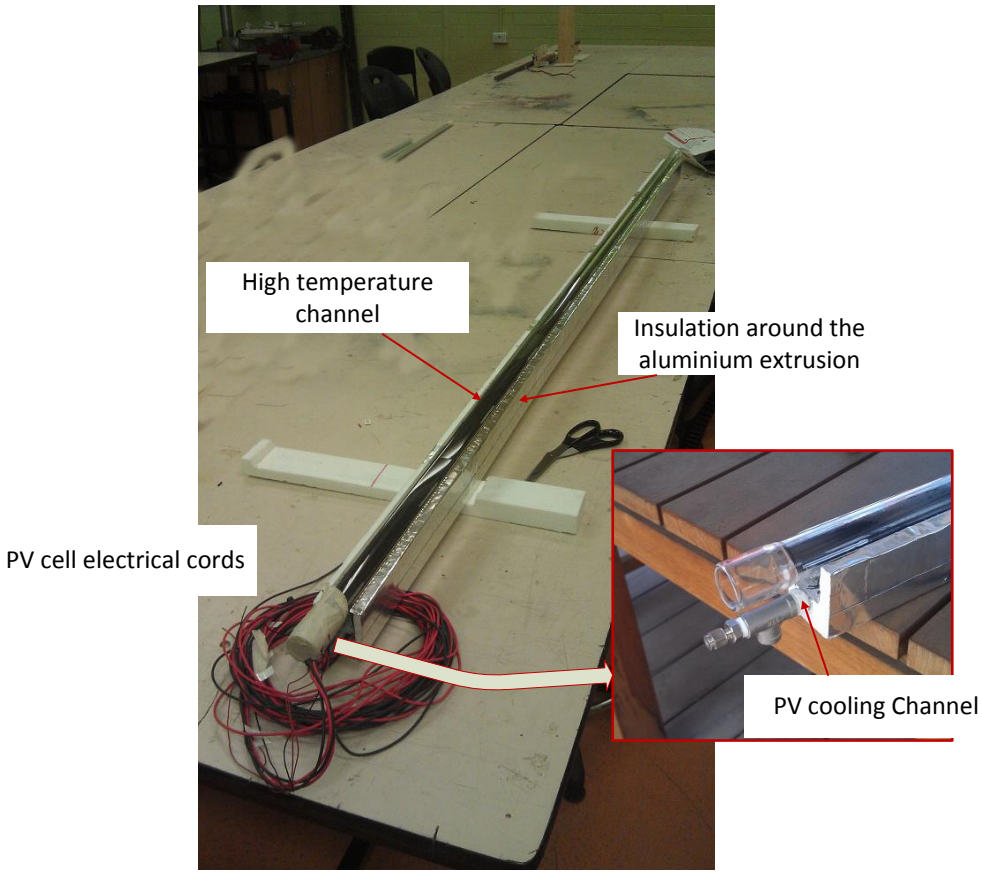

Fig. 6.10 The receiver fabricated for the outdoor measurement

6.2.1 Thermal performance

Two components in this system deliver heat: the high temperature channel filled with PG delivers $\dot{Q}_{hot}$, and the PV cooling channel filled with water, delivers $\dot{Q}_{cold}$. These parameters have been explained in Figure 6.13.

The above parameters can be calculated as follows:

$$\dot{Q}_{hot} = \dot{m}_{PG}\, C_{P,PG}\, (T_{H,out} - T_{H,in}) \tag{6.1}$$

$$\dot{Q}_{cold} = \dot{m}_{W}\, C_{P,W}\, (T_{C,out} - T_{C,in}) \tag{6.2}$$

where C_P is the specific heat at the average fluid temperature, $\dot{m}$ is the mass flow rate, T_{out} and T_{in} are the outlet and inlet temperatures of the respective fluids, and subscripts PG and W refer to propylene glycol and water respectively. The heat absorbed and delivered by the cold channel is from two sources: (1) the heat generated within the PV cells due to their

Fig. 6.11 The receiver-trough combination at the roof of RMIT University

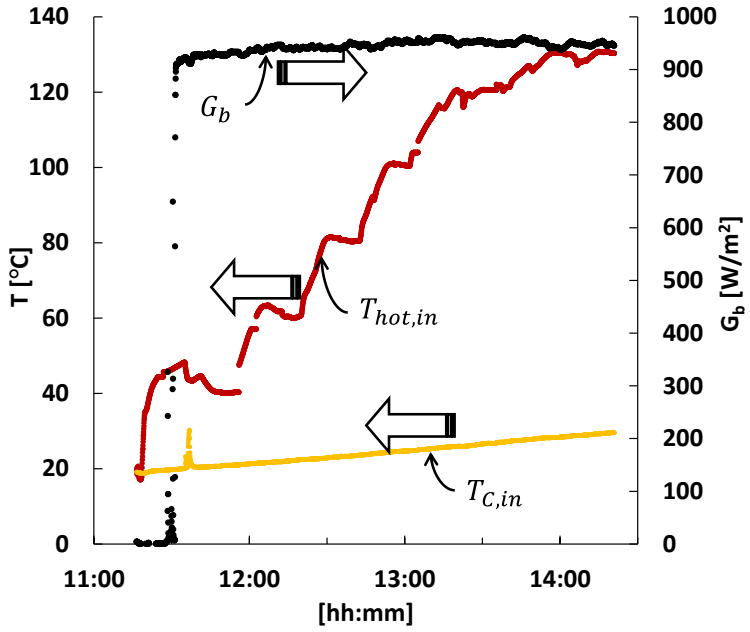

Fig. 6.12 Typical collector inlet temperature and direct beam radiation throughout a test period. average ambient temperature, $T_{amb} = 19.8°C$, average wind speed, $V_w = 1.94m/s$.

conversion efficiency of less than 1, $\dot{Q}_{pv \to cold}$, and (2) the heat that is conducted from the high temperature channel to the PV cooling through the silicone layer and the side walls,

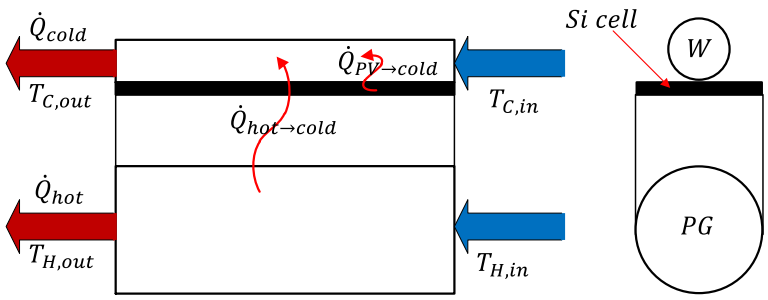

Fig. 6.13 The heat flow diagram in the hybrid receiver.

$\dot{Q}_{hot\rightarrow cold}$:

$$\dot{Q}_{cold} = \dot{Q}_{hot\rightarrow cold} + \dot{Q}_{pv\rightarrow cold} \tag{6.3}$$

The total heat delivered by the receiver is:

$$\dot{Q}_{th} = \dot{Q}_{hot} + \dot{Q}_{cold} \tag{6.4}$$

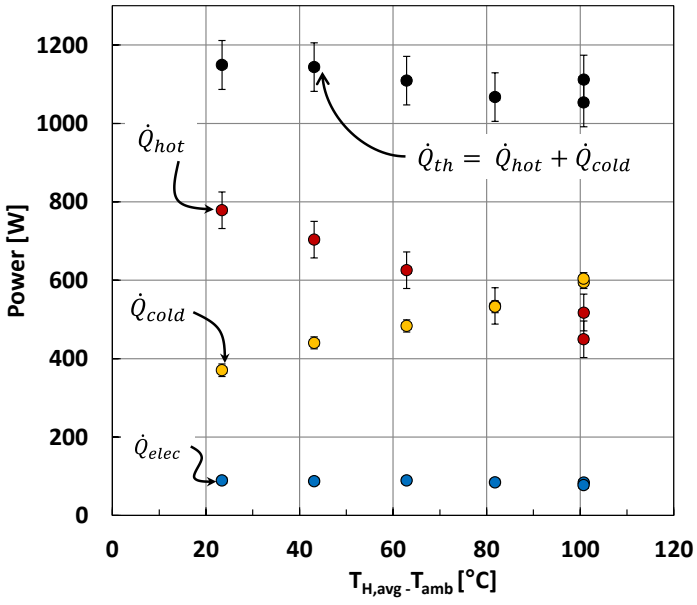

Fig. 6.14 Thermal and electrical output of the receiver as a function of the difference between collector inlet and ambient temperatures

Figure 6.14 shows the thermal and electrical power delivered by the receiver at different

inlet temperatures. The horizontal axis shows the temperature difference between the $T_{H,avg} = 0.5(T_{H,in} + T_{H,out})$ and the ambient temperature, T_{amb}. The inlet temperature of the PV cooling channel was set at 27.3 °C. The primary thermal channel delivers 778 W at low temperatures which then decreases to 517 W at $T_{H,avg} = 130$ °C. On the other hand, the heat collected by the PV cooling channel increases from 370 W to 595 W at the same time. This means that by increasing the temperature difference between the two channels, some heat is transferred from the high temperature channel to the PV cooling channel. Although the temperatures of the two streams are different from each other, there is still a level of thermal coupling between the channels.

The total heat delivered by both channels, $\dot{Q}_{th}$ is also presented in this figure. This is a combination of the above two thermal outputs which is about 1150 W at low temperatures and decreases to 1100 W at 130 $T_{H,in} = 130$ °C.

The other data which has been presented in this graph is the electrical output of the PV component. This is the total PV electricity produced by two modules in parallel that were simply added together. The power generated by them was calculated using their recorded I_{mpp} and V_{mpp} as follows:

$$\dot{Q}_{elec} = I_{mpp_1} V_{mpp_1} + I_{mpp_2} V_{mpp_2} \tag{6.5}$$

where I_{mpp} and V_{mpp} are the maximum power point current and voltage, and the subscripts 1 and 2 represent the two sets of PV cells which are wired in parallel.

As it is seen in this graph, the electrical output remains relatively constant at about 85 W. This is mainly because the PV cooling channel temperature was kept constant throughout the measurement. Hence the PV conversion efficiency was not affected by the elevated $T_{H,in}$. The DNI value was also steady at the time of the measurement which resulted in a constant PV power output.

6.2.2 Heat transfer between the two streams

As it was mentioned above a level of heat transfer was detected between the high temperature and the PV cooling channels. Although the heat delivered by the PV cooling channel is considered useful energy, this process is an exergy loss because heat is converted from high temperature to low temperature without producing work. Hence it was important to quantify the amount of heat transferred between the channels.

In order to have an indication of the heat transfer between the two channels, another experiment was conducted in which there was no heat gain from the sunlight. The receiver was

moved away from the tracking position by about 4 to 5 °to avoid receiving any concentrated light from the trough. The off-tracking angle was kept low in order not to change the ambient effects on the receiver such as its orientation and wind effects.
Inlet and outlet temperatures of the high temperature and PV cooling channels were monitored while varying the value of $T_{H,in}$ between 50°C and 110°C. The results from this experiment are presented in Figure 6.15.

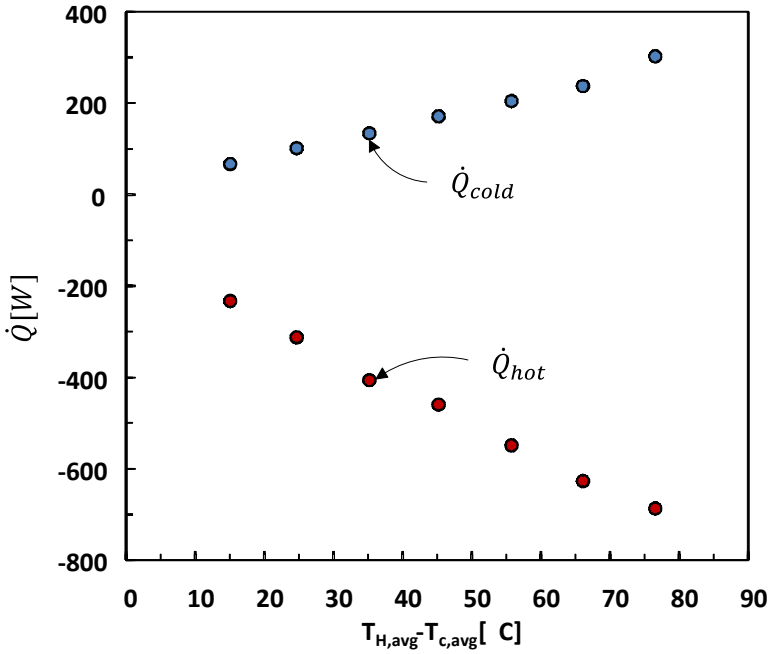

Fig. 6.15 Collector heat loss measured with the receiver in the "off-sun" position, ambient conditions: $T_{amb} = 31.4°C$, $V_w = 3.4m/s$

In this case, all the heat collected by the PV cooling channel was due to the heat conducted from the high temperature channel to the PV cooling channel i.e. $\dot{Q}_{hot\rightarrow cold} = h(T_{H,avg} - T_{C,avg})$. A linear curve fit through this data provides the following expression:

$$\dot{Q}_{hot\rightarrow cold} = 3.79(T_{H,avg} - T_{C,avg}) \tag{6.6}$$

where $T_{H,avg}$ and $T_{C,avg}$ represent the bulk mean temperature of the primary absorber and PV cooling channels respectively.

6.2.3 Beam splitting performance

By extrapolating the data in Figure 6.14 to 0 ($T_{H,avg} = T_{amb}$) an indication of beam splitting performance in the receiver can be acquired. Because in this condition, there is no heat loss to or gain from the ambient air, all the energy received by the receiver is just from the sun. This has been formulated as below:

$$\beta_{th} = \frac{\dot{Q}_{hot}\,|_{(T_{H,avg}=T_{amb})} + \dot{Q}_{hot\rightarrow cold}}{(\dot{Q}_{th} + \dot{Q}_{elec})\,|_{(T_{H,avg}=T_{amb})}} \tag{6.7}$$

where β_{th} is the thermal beam splitting fraction. Likewise, the PV cell beam splitting fraction is defined from:

$$\beta_{th} + \beta_{elec} = 1 \tag{6.8}$$

Knowing the value of β_{th} helps to determine the thermal and electrical efficiency of the receiver with respect to the energy available to each of these components after splitting the beam.

$$\eta_{th,hot} = \frac{\dot{Q}_{hot}}{\beta_{th}\, G_b\, A_{eff}} \tag{6.9}$$

Here G_b is the direct beam radiation and $A_{eff} = l \times (w_a - w_r)$ is the effective aperture area, accounting for shading of the receiver. Figure 6.16 presents the experimentally measured values for $\eta_{th,hot}$ against the predicted collector performance previously calculated in [166].

The efficiency of the hot channel starts at about 61% and more or less linearly reduces to about 30%. At the reduced temperature of 0.11 which corresponds to 130 °C temperature of the hot channel, the thermal efficiency drops to about zero. This is because at such high temperature, PG started local boiling at hot spots of the receiver (its boiling temperature is 155°C). Such hot spots are mainly at the surface of the SDG filters.
When assembling the receiver, two adjacent filters were connected to each other using a small high temperatures glue. The glue created a small bump on filter surfaces. This along with the small gaps between the filter due to small edge chamfers, creates low velocity or even stagnant flow spots within the fluid. When the PG bulk temperatures rises to high temperatures, the liquid in these spots starts boiling.
Local boiling of the PG absorbs significant latent heat. Since the thermal efficiency is measured and calculated based on sensible heat (signal coming from the RTDs), the heat absorbed as latent type is not included in the efficiency values and the reported efficiency is significantly lower.

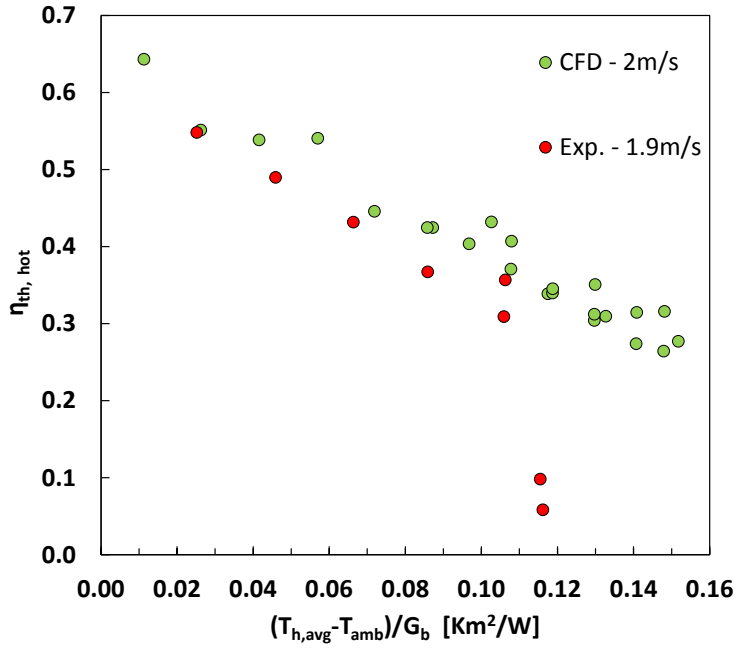

Fig. 6.16 Primary absorber channel thermal efficiency – expressed relative to energy available for thermal absorption

It should be mentioned that by improving the assembling method and removing any non-smoothness from the surface of the filter assembly, the chance of local boiling can be minimised. One option to do this is using longer filters without any edge chamfers.
A linear curve fit applied to the experimental results excluding the values corresponding to fluid boiling yields the following expression:

$$\eta_{th,hot} = 0.61 - 2.68\frac{T_{H,avg} - T_{amb}}{G_d} \tag{6.10}$$

Using this expression the estimated stagnation temperature is approximately 234°C. Extrapolating the performance to the intended operating conditions of $T_{H,in} = 150°C$ we obtain an estimated thermal efficiency of $\eta_{th,H} \approx 26\%$ ($T_{amb} = 20°C$, $G_d = 900W/m^2$). Whilst these values are considerably lower than other commercially available CST collectors (e.g. Chromasun, NEP Solar) they demonstrate the potential for high grade thermal energy generation concurrently with electrical output using volumetric beam splitting techniques.
In order to give a true measure of the energy utilisation of the receiver, it is necessary to express the useful energy gains with respect to the total energy available for utilisation. The overall system thermal efficiency η_{th} and electrical efficiency η_{elec} are defined using the

following expressions:

$$\eta_{th} = \frac{\dot{Q}_{th}}{\dot{Q}_{avail}} \tag{6.11}$$

$$\eta_{elec} = \frac{\dot{Q}_{elec}}{\dot{Q}_{avail}} \tag{6.12}$$

where $\dot{Q}_{avail} = G_d\ A_m cos(\theta)$ is the total direct radiant energy reaching the aperture plane of the collector and $cos(\theta)$ is the angle the sun makes with the collector normal. Figure 6.17 presents the thermal efficiency of the high and low grade heat streams and a total conversion efficiency calculated with respect to this quantity. The plot indicates that there is a gradual decline in the total conversion efficiency as the collector temperature is increased. At $T_{H,in} = 120°C$ the total thermal efficiency is approximately 46%.

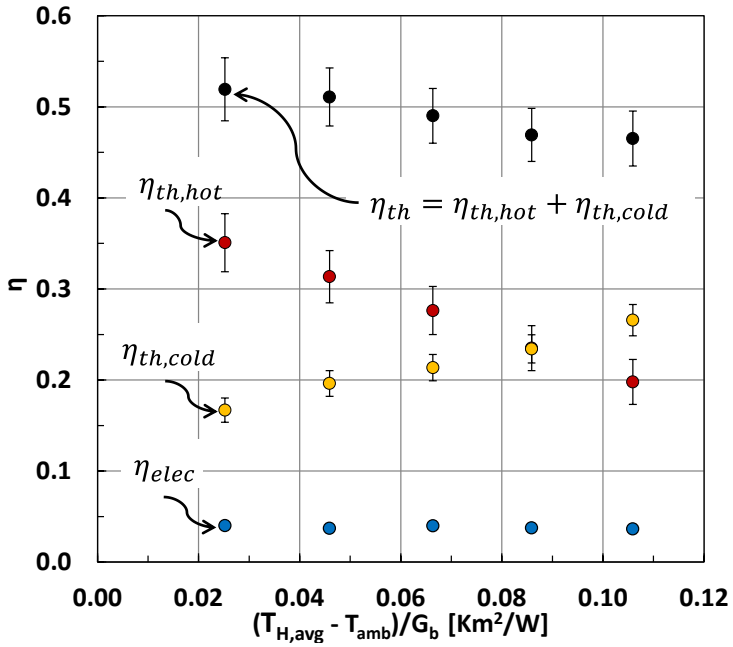

Fig. 6.17 Collector system efficiency – expressed relative to total direct radiant energy incident on the concentrator aperture area

By extrapolating the total systems efficiency data back to the vertical axis (including the PV output), the optical efficiency of the systems can be estimated to be 65%. This includes actual mirror, interception, shading, misalignment, and receiver Fresnel reflection losses. There is a number of improvement opportunities to minimise these losses and improve the

system efficiency.

6.2.4 Electrical performance

As it was mentioned before, two DC loads were programmed to sweep through the I-V curve of the two PV modules in the receiver. Each module had 90 cells in series. This was carried out every 3 minutes and one sweep took 30 seconds to complete. Sample I-V data has been presented in Figure 6.18a.
The V_{OC} of each module reached 64 V which was boosted by high concentration on the cells. The I_{SC} of each module reached about 0.92 A. Using this data, the power-voltage data were generated within the Labview program to find the mpp of each module. This data has been presented in 6.18b. The maximum power generated by each module reached about 38 W at V_{mpp} of 54 V. The maximum power generated by both modules was about 76 W which was equal to 42.4 W/m of the receiver length.

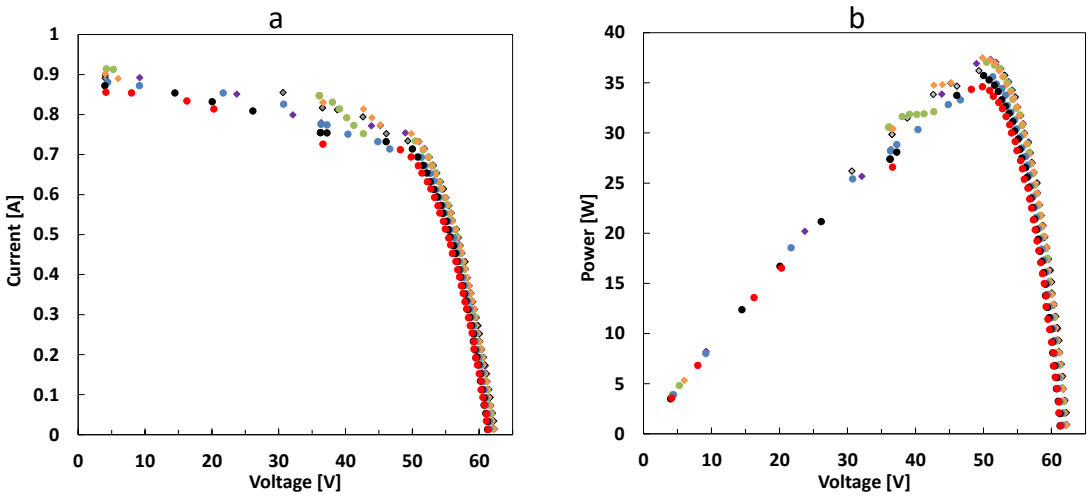

Fig. 6.18 Typical (a) $I-V$, and (b) power curves for a set of 3 PV modules (90 cells)

PV conversion efficiency of the receiver with respect to the total power reaching the mirror aperture is about 3.5% to 3.8%. This is lower than what ws expected and the causes needs to be analysed. Two causes were identified to be affecting the PV efficiency: (1) the overall optical losses of the system which reduces the amount of light reaching the PV cells; this reduces the I_{SC}, (2) The non-uniform partial shading of the cells along the receiver which mainly reduces the V_{OC} due to bypass diode activation.

6.2.5 Partial cell shading

As mentioned before, the SDG filters were inserted into the tube and maintained at its mid-plane using the structure created by glass rods. Adjacent filters needed to be bound to each other in order to prevent them from dislocation. At the time of assembling this prototype, no optically clear adhesive with high durability under high temperatures and compatible with hot PG was found at a reasonable price. Hence a less transparent high temperature silicone adhesive was used instead (see Figure 6.4).
The adhesive between the filters caused these areas to be less transparent compared to the rest of the filter area. The cells beneath these spots receive less light and generate less current in comparison to the rest of the cells. This results in a current mismatch between them. Once this mismatch reaches a certain threshold, the bypass diodes are activated. Each activated diode will remove the voltage of 7 cells from the system. The jagged nature of the data points at voltages less than about 50 V in Figure 6.18a. It should be noted that bypass diodes are activated by increasing the current.

6.2.6 Effect of non-uniform illumination

As it was discussed in section 6.1.2, the longitudinal light intensity distribution along the receiver varies by $\pm 14\%$. This means that in the worst case scenario, a cell in a series configuration will generate 14% less current. Although some other cells over-perform, this cell will determine the actual net current generated by the module. Hence, the whole module is under-performing by 14% in short circuit current.
Considering the cell generated power to be approximated by:

$$P = FF \times V_{OC} \times I_{SC} \tag{6.13}$$

and assuming that open circuit voltage and fill factor remain the same, the power generated by the cell will be under-performing by 14%. This adds an additional loss due to light non-uniformity along the receiver induced by the mirror surface sag.

6.2.7 Reduction in PV cell short circuit current, I_{sc}

Detailed optical modelling of the hybrid receiver, performed using ray tracing software Zemax and presented in the previous section, revealed 29% of the light incident upon the receiver reaches the PV cells. Also, 77% of the available energy in the ideal filtered band

of 700-1100 nm reaches the PV cells, which represents approximately 26% of the incident energy.

From Figure 6.18a, it can be seen that the maximum measured I_{SC} was 0.92 A. During these measurements the DNI value was about $990W/m^2$. Under these conditions, if we assume ideal spectral splitting with cut-off wavelengths at 700 nm and 1100 nm and no optical losses the short circuit current would have been 2.4 A (determined by integration of the spectral response of the cells with the spectral power density). The measured value is considerably less than this ($\approx$ 38% of ideal. The difference can be somewhat understood by investigating the likely losses.

The reflectivity of both the primary parabolic concentrator and internal side mirrors is around 80-85% in this spectral band. Potentially this value could be as much as 10% lower than the manufacturer data due to the influences of dust and grime on the mirror surface. Likewise, additional absorption can be expected within the borosilicate glass absorber tube due to dirt and other residues accumulated during the manual fabrication process, which can be assumed to add a further 5% loss.

Up to 10% loss can also be possible due to the intercept factor of the receiver, considering the fact that the circumsolar radiation (with 5°cone angle) cannot be captured by the receiver. Combining these supposed losses it is possible the measured I_{SC} could be reduced by as much as 42% of the ideal value. Other possible sources of error which are not possible to consider here and could further reduce this value are factors such as the influence of temperature on the transmission spectra of both the PG and SDG filters.

6.2.8 The influence of cell temperature

The PV cooling channel of the receiver can be used as a secondary source of heat for low temperature applications. However its maximum operating temperature is restricted by the suitable temperature for the Si cells. There is a trade-off between the cells efficiency and elevating the channel temperature. In order to quantify this, a new experiment was conducted. In this experiment, the temperature of the PV cooling channel was varied from 35 °C to 66 °C. During this scan, the electrical power generated by the PV cells was monitored. The data has been presented in Figure 6.19. The vertical axis is the normalised power with respect to the reference power at 25°C.

A linear regression was fit to the data. The slope of the line ($-0.34\%/°C$) represents the temperature coefficient of the cells which matches well with the reported data for Si cells. During the same period there was a measured reduction in the V_{oc} of the cells of $-1.53mV/°C$.

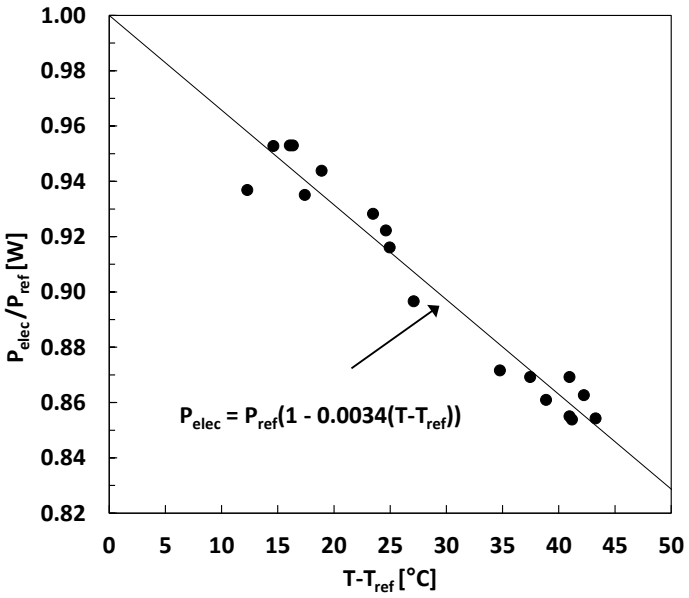

Fig. 6.19 Dependence of PV output on cooling channel temperature. Here the reference condition refers to a cooling channel inlet temperature of 25°C.

6.2.9 Pumping power

For any thermal system, having an indication of the required pumping power is essential to investigate its net performance. In this prototype, the flow was mainly in laminar regime so the estimation of the required pumping power has been calculated for Re number of 63 to 3370 as mentioned in section 6.1.5.

$$f = \frac{64}{Re} \tag{6.14}$$

$$\Delta P = f \frac{L}{D} \frac{\rho V^2}{2} \tag{6.15}$$

The pressure drop at Re numbers of 63 and 3370 with a flow rate of 0.08 kg/s is about 1050 and 19 Pa per meter respectively. This corresponds to about 0.08 W/m and 0.015 W/m of the required pumping power which shows that in comparison to the thermal (250 W/m) and PV (42 W/m) power delivered by the receiver, the pumping parasitic losses are negligible.

6.2.10 Future improvements

Three main loss mechanism appeared in the system. First, the optical losses reduced the amount of the light reaching the receiver specifically in the 700-1100 nm band due to low reflection of aluminium based mirrors. Other type of mirrors such as silver based ones have

higher reflection in this range. The mirrors, at least the side mirrors within the receiver, can be replaced with such silver based ones to suppress optical losses.
The second source of losses in the system is due to the heat loss from the glass tube to the ambient, particularly at the presence of high velocity wind. A relatively practical solution for this is using a transparent thermal shield in front of the tube to reduce the convective coefficient. This can be similar to a glass tube in tube configuration. The other loss mechanism is due to the heat transfer from the PG channel to the PV cooling channel through the silicone encapsulant in between. An air gap or transparent insulator such as silica aerogel can be located within the silicone layer to break the thermal bridge.
The partial shading on the cells due to the filter assembly problems significantly reduces the electrical output. This requires proper consideration. A possible solution is customising the cross section of the glass tube in order to avoid using any glass rods and silicone adhesive. Such customised glass tube can have a groove at each side to hold the filters. Also longer filters can be used without any adhesive in between to avoid non-uniform illumination on the cells. This also reduces the chance of local boiling in the receiver.
For increasing the operational temperature of the primary channel, replacing PG with another liquid that has higher boiling temperature with suitable optical and heat transfer properties is essential. However at the time of conducting this research, such liquid was not identified. More research and perhaps material development is required to find a more suitable heat transfer fluid.

6.3 Summary

A real scale prototype of the receiver introduced in the previous chapter was built and tested in an outdoor measurement. This chapter reported the experiment details and the acquired results.
The receiver reached an optical efficiency of 61%. The quality o the parabolic mirror, misalignments, Fresnel reflection losses, and intercept factor were identified to be the main optical loss mechanisms. The primary high temperature channel achieved an efficiency of about 35.1% at 40°C and 19.8% at 120°C with respect to the solar power striking the aperture of the primary parabolic mirror. The same efficiencies were 54.8% and 30.9% with respect to the solar energy available for thermal conversion after splitting the beam.
The heat collected by the PV cooling channel may also be applied by the demand side. In that case, the total thermal efficiency of the system, considering the total output from both thermal channels, was about 46.5% at 120°C.

The PV component reached a power output of 85 W/m length of the receiver which corresponded to a PV conversion efficiency of 16% with respect to the light available for PV conversion after beam splitting.

Chapter 7

Conclusions

In this thesis the feasibility of employing direct absorption spectral beam splitting in concentrating PV-T receivers was investigated. The considered PV-T receiver was a high temperature (above 120 degree C) receiver to be installed on linear solar concentrators such as Fresnel arrays or parabolic troughs. The beam splitting component of the receiver needed to be able to direct the wavelengths between ~700 nm and ~1100 nm to silicon solar cells and the rest of the spectrum to a thermal absorber.

The effect of cut-off wavelengths on the thermal and PV conversion performance of such receivers were studied in this thesis. It was shown that for a specific thermal configuration, with a simple heat sink at the back of Si PV cells, the concentration ratio drives the optimal cut-off wavelengths. If the cell-heat sink temperature difference is to remain below 15°C at a concentration ratio of 40, the cut-off wavelengths should be about 670 nm and 1100 nm for a fluid heat sink with 1000 W/m^2 convection coefficient which is common for a cooling flow through a tube. However the cell temperature is not the only factor determining the suitable cut-off wavelengths. The energy output from the system was also considered to be an important factor. Should electrical energy be considered several times more valuable than heat, the suitable range for the PV was decided to be 700 nm to 1100 nm. It was shown that with such cut-off wavelengths, the cell can reach an efficiency of 29.8% in theory.

Achieving accurate and efficient spectral beam splitting for hybrid PV-T systems in linear concentrators is an ongoing challenge. By conducting a thorough literature review, the main methods of spectral beam splitting for solar energy introduced so far were identified. Dichroic , wave interference, filters have been studied extensively for solar PV applications. However, there hadn't been any successful demonstration for hybrid PV-T systems in the literature at the time of starting this research. Most of the systems reported in the literature have focused on pure PV systems and less attention has been paid to high temperature PV-T configurations. Other innovative methods were required to achieve spectral beam splitting in

such receivers.

In this thesis, major focus was on volumetric absorbers. It was shown that combining dichroic filters with a spectrally selective thermal fluid can help to simplify the structure of the required filter. In a configuration similar to the proposed one in chapter 4, the thermal fluid absorbs the wavelengths in the infra-red, and the dichroic filter-absorbing side walls combination absorbs the major fraction of the light at wavelengths below 700 nm. Using this method, the required dichroic filter can be as simple as an edge filter instead of a bandpass or bandstop one. Edge filters have simpler structures and are easier to manufacture. The experimental analysis of the proposed configuration showed that such a receiver can be made with the optical properties of very close to the designed one. The PV efficiency with this optics can reach 26.1%, however it was shown that there was a degree of spectral mismatch between the proposed receiver and the desired filter. Although the method was simpler than the common dichroic filtering methods but its performance did not warrant consideration as a practical option. The structure of a dichroic filter with suitable accuracy needs more dielectric layers which leads to more complexity and higher cost.

Studying the unique optical properties of semiconductor doped glass showed a significant potential for them to be used as an effective light filter/thermal absorber for concentrating hybrid PV-T receivers. The advantage of these filters is their sharp cut-off wavelengths and effective absorbance of low band of light. They are generally long-pass filters that can be produced at a relatively low cost compared to dichroic filters. However they also need to be combined with another filtering medium to absorb the wavelengths beyond 1100 nm to create a band pass effect.

A novel receiver design based on the above approach was introduced in this thesis in chapter 5. It combined SDG filters with propylene glycol in a borosilicate tube as an optical filter and a high temperature thermal receiver. The combination absorbs a specific band of the light and transforms it into heat. The absorbed heat in the SDG filter is convected to propylene glycol. The concentrated light passing the tube is filtered, and the wavelengths in the range of 700 to 1100 nm reach the cells located at the top of the receiver.

The optical analysis showed that 64% of the incoming light is absorbed as heat in the high temperature channel and 29% is directed to the Si cells. The spectral distribution of light on the cells is of primary importance. A ray tracing analysis showed that 77% of the light on the cells is within 700 nm-1100 nm range. The cells were expected to reach an efficiency of about 26.5% under this illumination. An indoor experimental study showed that the proposed design can achieve optical properties close to the modelling results. This system presented only 3.8% reflection losses, which is because of good refractive index matching between the optical components.

This design was the basis of the prototype receiver for the outdoor measurement in real world conditions. A major step in taking the idea to this level was to study the illumination characteristics of the solar concentrator. The concentrator used for this thesis was NEP-Solar Polytrough 1200, which is a parabolic trough suitable for ground and rooftop mounting. Analysis of the current methods of flux profile measurement in the literature showed that there is a lack of proper methods for measuring the flux at close range. This is an important issue because usually there is not enough space in such concentrators to mount the camera far enough from the receiver in radiometric measurement.

Using the close range radiometry measurement introduced in this thesis, it was determined that 92% of the flux is within 20 mm wide strip along the receiver. Although the fabricated prototype didn't achieve the theoretically predicted efficiency, it showed the possibility of using a combination of selective heat transfer liquids, here propylene glycol, and SDG filters as a light filtering medium. The system measurement showed a high temperature thermal efficiency of 30.9% and PV conversion efficiency of about 16% at 120°C under the light received by the high temperature thermal absorber and the PV cells respectively.

The low efficiency of the system is due to various reasons including the lack of uniform illumination along the PV cells causing low electrical output. More suitable fabrication methods are required to assemble the receiver eliminating any significant non-uniformity along the series connected PV cells. The low efficiency of the thermal component is mainly due to heat loss to the environment which should be tackled by implementing a transparent thermal insulation around the high temperature glass tube.

The degradation of the PG after 3 months of filling the system didn't affect the optics adversely, however its thermal properties may be affected. PG is suitable for temperatures of up to 120 °C but above this temperature local boiling can occur due to low Reynolds number and lack of mixing in the thermal channel. The optical properties of PG deviates from the ideal properties for accurate spectral splitting in the long wavelengths, although it shows strong absorption in infra red. The undesirable absorption at about 850 nm is contradictory to higher electrical yield since this band is in the high spectral response range of Si cells. More suitable liquids should be selected or synthesised to optically suit Si cells.

Another area that needs to be carefully considered is that aluminium based concentrating mirrors suffer from reflection drop in at about 870 nm which is not desirable for Si cells. In spectrally splitting systems this causes significant electrical efficiency drop. Other type of mirror for example silver based or mirrors with specially engineered coating to boost the reflection in this band is required to address this issue.

This research showed the possibility of thermally decoupling PV cells from a high temperature thermal receiver in a PV-thermal collector. The performance test of the system proved

the idea. However, due to the fact that this system was the first of its kind ever designed and built, predicting and preventing all potential hurdles to improve its efficiency was not possible.

A thermal absorber with a temperature limited to 120°C is suitable for process heat supply but not for power generation. A hybrid thermal-PV collector can be a suitable option when there is limited rooftop space. In that case extracting the highest possible energy from the available area is critical. On the other hand, the suitability of this system for power generation which is an important target for this proposal should be investigated.

Organic Rankin cycles have been suggested for generating electricity from such a low temperature heat source but their practicality is questionable. The proposed system in this thesis must be improved significantly to be able to generate heat at higher temperatures to drive a more efficient thermodynamic cycle. Several factors that limited the performance of the prototype system have been listed in chapter 6. They restricted the efficiency and the maximum operating temperature achieved in the experiment. Most of these issues are engineering problems with potential solutions such as vacuum insulation around the high temperature channel as well as within the silicone layer.

The operating temperature of the proposed spectral beam splitter is limited by the maximum allowed temperature of the glass parts and the liquid. A high quality borosilicate glass tube with a glass transition temperature of above 550°C is able to maintain a working fluid at 350°C. The current SDG filters are limited by their glass transition temperature which is about 530°C. Their temperature should not exceed 330°C. This is close to the temperature that oil based parabolic trough plants can achieve (390°C - due to the oil instability at high temperatures). Should a more suitable working fluid other than propylene glycol be identified for the proposed system, an operating temperature of above 300°C is feasible.

In that case, the collector can operate as a pre-heater for a solar field in series configuration. The outlet of the hybrid receiver can feed into traditional concentrating solar collectors. Then the hybrid receivers can deliver heat and electricity concurrently. The hot fluid delivered by the last receiver enters the second stage of heating in traditional parabolic troughs that can increase the temperature of the working fluid to 390°C which is the current limit for oil based CSP plants. Such temperature can power a more efficient thermodynamic cycle.

As future work, it is recommended to consider better thermal insulation around the high temperature channel. This includes a transparent thermal shield in front of the glass tube exposed to the concentrated light as well as a transparent heat transfer barrier between the glass tube and the solar cells.

A glass tube with a specifically designed cross section can be also used to hold the SDG filters in place. This can remove the requirement for difficult and unstable filter mounting

mechanism using small glass rods. It can also help to slip filters into the glass tube without gluing them together. This can create a more longitudinally uniform illumination on the cells along the channel and significantly increase the electrical performance of the receiver.
The performance of the receiver optics in collecting the circum-solar radiation should be investigated experimentally as well as using ray tracing models. This aspect of the receiver can be improved to help achieve a better optical efficiency. The type of the mirror can also be changed for the sake of higher spectral reflectance in 700-1100 nm ban which can improve the electrical performance.

References

[1] Enerdata. https://yearbook.enerdata.net/energy-consumption-data.html.

[2] David Ginley, Martin A Green, and Reuben Collins. Solar energy conversion toward 1 terawatt. *Mrs Bulletin*, 33(04):355–364, 2008.

[3] Agust'n M Delgado-Torres. Solar thermal heat engines for water pumping: An update. *Renewable and Sustainable Energy Reviews*, 13(2):462–472, 2009.

[4] VV Tyagi, SC Kaushik, and SK Tyagi. Advancement in solar photovoltaic thermal (pv t) hybrid collector technology. *Renewable and Sustainable Energy Reviews*, 16(3):1383–1398, 2012.

[5] Martin A Green, Keith Emery, Yoshihiro Hishikawa, Wilhelm Warta, and Ewan D Dunlop. Solar cell efficiency tables (version 45). *Progress in photovoltaics: research and applications*, 23(1):1–9, 2015.

[6] Ethan R Torrey, Jennifer Krohn, P Paul Ruden, and PI Cohen. Efficiency of a laterally engineered architecture for photovoltaics. In *Photovoltaic Specialists Conference (PVSC), 2010 35th IEEE*, pages 002978–002983. IEEE, 2010.

[7] Howard M Branz, William Regan, Kacy J Gerst, J Brian Borak, and Elizabeth A Santori. Hybrid solar converters for maximum exergy and inexpensive dispatchable electricity. *Energy & Environmental Science*, 2015.

[8] Thermal energy storage, technology brief (2013). www.irena.org.

[9] MAC Chendo, MR Jacobson, and DE Osborn. Liquid and thin-film filters for hybrid solar energy conversion systems. *Solar & wind technology*, 4(2):131–138, 1987.

[10] William Shockley and Hans J Queisser. Detailed balance limit of efficiency of p-n junction solar cells. *Journal of applied physics*, 32(3):510–519, 1961.

[11] ED Jackson. Areas for improvement of the semiconductor solar energy converter. In *Transactions of the Conference on the Use of Solar Energy*, volume 5, pages 122–126, 1955.

[12] RL Moon, LW James, HA Vander Plas, TO Yep, GA Antypas, and Y Chai. Multigap solar cell requirements and the performance of algaas and si cells in concentrated sunlight. In *13th Photovoltaic specialists conference*, volume 1, pages 859–867, 1978.

[13] AG Imenes and DR Mills. Spectral beam splitting technology for increased conversion efficiency in solar concentrating systems: a review. *Solar energy materials and solar cells*, 84(1):19–69, 2004.

[14] Raymond K Kostuk and Glenn Rosenberg. Analysis and design of holographic solar concentrators. In *Solar Energy+ Applications*, pages 70430I–70430I. International Society for Optics and Photonics, 2008.

[15] Raymond K Kostuk, Jose Castillo, Juan M Russo, and Glenn Rosenberg. Spectral-shifting and holographic planar concentrators for use with photovoltaic solar cells. In *Solar Energy+ Applications*, pages 66490I–66490I. International Society for Optics and Photonics, 2007.

[16] Raymond K Kostuk, Jose Castro, Brian Myer, Demming Zhang, and Glenn Rosenberg. Holographic elements in solar concentrator and collection systems. In *SPIE Solar Energy+ Technology*, pages 74070E–74070E. International Society for Optics and Photonics, 2009.

[17] H.A. Macleod. *Thin-Film Optical Filters, Fourth Edition*. Series in Optics and Optoelectronics. Taylor & Francis, 2010.

[18] Marius Peters, Jan Christoph Goldschmidt, Philipp Löper, Bernhard Groß, Johannes Üpping, Frank Dimroth, Ralf B Wehrspohn, and Benedikt Bläsi. Spectrally-selective photonic structures for pv applications. *Energies*, 3(2):171–193, 2010.

[19] AG Imenes, D Buie, and D McKenzie. The design of broadband, wide-angle interference filters for solar concentrating systems. *Solar Energy Materials and Solar Cells*, 90(11):1579–1606, 2006.

[20] Gang Wang, Xiao-Fang Cheng, Peng Hu, Ze-Shao Chen, Yang Liu, and Lei Jia. Theoretical analysis of spectral selective transmission coatings for solar energy pv system. *International Journal of Thermophysics*, 34(12):2322–2333, 2013.

[21] VP Khvostikov, SV Sorokina, NS Potapovich, VI Vasil'ev, AS Vlasov, MZ Shvarts, N Kh Timoshina, and VM Andreev. Single- junction solar cells for spectrum splitting pv system. In *Proc. 25th Europ. Photovoltaic Solar Energy Conf. and Exhibition.-Valencia*, pages 167–171, 2010.

[22] Alexander V Tikhonravov, Michael K Trubetskov, and Gary W DeBell. Application of the needle optimization technique to the design of optical coatings. *Applied optics*, 35(28):5493–5508, 1996.

[23] Brian T Sullivan and JA Dobrowolski. Implementation of a numerical needle method for thin-film design. *Applied optics*, 35(28):5484–5492, 1996.

[24] AG Imenes, D Buie, DR Mills, P Schramek, and SG Bosi. A new strategy for improved spectral performance in solar power plants. *Solar energy*, 80(10):1263–1269, 2006.

[25] Juan M Russo, Deming Zhang, Michael Gordon, Shelby Vorndran, Yuechen Wu, and Raymond K Kostuk. Spectrum splitting metrics and effect of filter characteristics on photovoltaic system performance. *Optics express*, 22(102):A528–A541, 2014.

[26] David Berney Needleman, Jonathan P Mailoa, Riley E Brandt, Niall M Mangan, and Tonio Buonassisi. Sensitivity analysis of optical metrics for spectral splitting photovoltaic systems: A case study. 2015.

[27] Carissa N Eisler, Emily C Warmann, Cristofer Flowers, Michelle Dee, Emily D Kosten, Harry Atwater, et al. Design improvements for the polyhedral specular reflector spectrum-splitting module for ultra-high efficiency (> 50%). In *Photovoltaic Specialist Conference (PVSC), 2014 IEEE 40th*, pages 2224–2229. IEEE, 2014.

[28] Cristofer Flowers, Carissa N Eisler, Harry Atwater, et al. Electrically independent subcircuits for a seven-junction spectrum splitting photovoltaic module. In *Photovoltaic Specialist Conference (PVSC), 2014 IEEE 40th*, pages 1339–1343. IEEE, 2014.

[29] Allen Barnett, Christiana Honsberg, Douglas Kirkpatrick, Sarah Kurtz, Duncan Moore, David Salzman, Richard Schwartz, Jeffrey Gray, Stuart Bowden, Keith Goossen, et al. 50% efficient solar cell architectures and designs. In *Photovoltaic Energy Conversion, Conference Record of the 2006 IEEE 4th World Conference on*, volume 2, pages 2560–2564. IEEE, 2006.

[30] James D McCambridge, Myles A Steiner, Blair L Unger, Keith A Emery, Eric L Christensen, Mark W Wanlass, Allen L Gray, Laszlo Takacs, Roger Buelow, Timothy A McCollum, et al. Compact spectrum splitting photovoltaic module with high efficiency. *Progress in Photovoltaics: Research and Applications*, 19(3):352–360, 2011.

[31] Chunhui Shou, Zhongyang Luo, Tao Wang, Weidong Shen, Gary Rosengarten, Wei Wei, Cheng Wang, Mingjiang Ni, and Kefa Cen. Investigation of a broadband tio 2/sio 2 optical thin-film filter for hybrid solar power systems. *Applied Energy*, 92:298–306, 2012.

[32] A Imenes, C Fell, and W Stein. Spectral beam splitter for solar hydrogen production. In *Proceedings of Solar*, volume 7, 2007.

[33] Deming Zhang, Yuechen Wu, Juan M Russo, Michael Gordon, Shelby Vorndran, and Raymond K Kostuk. Optical performance of dichroic spectrum-splitting filters. *Journal of Photonics for Energy*, 4(1):043095–043095, 2014.

[34] Felipe Crisostomo, Robert A. Taylor, T Zhang, Perez-Wurfl I., Gary Rosengarten, Vernie Everett, and Evatt R. Hawkes. Experimental testing of sinx/sio2 thin film filters for a concentrating solar hybrid pv/t collector. *Renewable Energy*, in press, 2014.

[35] 3m cool mirror film 330 2013. http://multimedia.3m.com/mws/media/752578O/3mtm-cool-mirror-film-330.pdf.

[36] Zhengshan J Yu, Kathryn C Fisher, Brian M Wheelwright, Roger P Angel, and Zachary C Holman. Pvmirror: a new concept for tandem solar cells and hybrid solar converters. 2015.

[37] Donato Vincenzi, Alessandro Busato, Marco Stefancich, and Giuliano Martinelli. Concentrating pv system based on spectral separation of solar radiation. *physica status solidi (a)*, 206(2):375–378, 2009.

[38] Ye Jia-Sheng, Wang Jin-Ze, Huang Qing-Li, Dong Bi-Zhen, Zhang Yan, and Yang Guo-Zhen. A single diffractive optical element implementing spectrum-splitting and beam-concentration functions simultaneously with high diffraction efficiency. *Chinese Physics B*, 22(3):034201, 2013.

[39] Qingli Huang, Jinze Wang, Baogang Quan, Qiulin Zhang, Dongxiang Zhang, Dongmei Li, Qingbo Meng, Li Pan, Yanqin Wang, and Guozhen Yang. Design and fabrication of a diffractive optical element as a spectrum-splitting solar concentrator for lateral multijunction solar cells. *Applied optics*, 52(11):2312–2319, 2013.

[40] Matthew D Escarra, Sunita Darbe, Emily C Warmann, Harry Atwater, et al. Spectrum-splitting photovoltaics: Holographic spectrum splitting in eight-junction, ultra-high efficiency module. In *Photovoltaic Specialists Conference (PVSC), 2013 IEEE 39th*, pages 1852–1855. IEEE, 2013.

[41] Yuhan Yao, He Liu, and Wei Wu. Spectrum splitting using multi-layer dielectric metasurfaces for efficient solar energy harvesting. *Applied Physics A*, 115(3):713–719, 2014.

[42] Jia-hong Huang, Wun-Ciang Fei, Wei-Chi Hsu, and Jui-che Tsai. Solar concentrator constructed with a circular prism array. *Applied optics*, 49(23):4472–4478, 2010.

[43] Carlo Maragliano, Matteo Chiesa, and Marco Stefancich. Point-focus spectral splitting solar concentrator for multiple cells concentrating photovoltaic system. *arXiv preprint arXiv:1504.00258*, 2015.

[44] Carlo Maragliano, Tim Milakovich, Matteo Bronzoni, Stefano Rampino, Eugene A Fitzgerald, Matteo Chiesa, and Marco Stefancich. Demonstration of a novel dispersive spectral splitting optical element for cost-effective photovoltaic conversion. *arXiv preprint arXiv:1508.00210*, 2015.

[45] Ekkard Brinksmeier, Ralf Gläbe, and Lars Schönemann. Review on diamond-machining processes for the generation of functional surface structures. *CIRP Journal of Manufacturing Science and Technology*, 5(1):1–7, 2012.

[46] Marco Stefancich, Ahmed Zayan, Matteo Chiesa, Stefano Rampino, Dario Roncati, Lionel Kimerling, and Jurgen Michel. Single element spectral splitting solar concentrator for multiple cells cpv system. *Optics express*, 20(8):9004–9018, 2012.

[47] Carlo Maragliano, Ahmed Zayan, and Marco Stefancich. Three-dimensional point-focus spectral splitting solar concentrator system. *International Journal of Optics and Applications*, 4(4A):6–11, 2014.

[48] Francesco Meinardi, Hunter McDaniel, Francesco Carulli, Annalisa Colombo, Kirill A Velizhanin, Nikolay S Makarov, Roberto Simonutti, Victor I Klimov, and Sergio Brovelli. Highly efficient large-area colourless luminescent solar concentrators using heavy-metal-free colloidal quantum dots. *Nature nanotechnology*, 2015.

[49] Chun-Hsien Chou, Min-Hung Hsu, and Fung-Chung Chen. Flexible luminescent waveguiding photovoltaics exhibiting strong scattering effects from the dye aggregation. *Nano Energy*, 15:729–736, 2015.

[50] Michael G Debije and Paul PC Verbunt. Thirty years of luminescent solar concentrator research: solar energy for the built environment. *Advanced Energy Materials*, 2(1):12–35, 2012.

[51] Jan Christoph Goldschmidt, Chau Do, Marius Peters, and Adolf Goetzberger. Spectral splitting module geometry that utilizes light trapping. *Solar Energy Materials and Solar Cells*, 108:57–64, 2013.

[52] Greg D Barber, Paul G Hoertz, Seung-Hyun Anna Lee, Neal M Abrams, Janine Mikulca, Thomas E Mallouk, Paul Liska, Shaik M Zakeeruddin, Michael Gratzel, Anita Ho-Baillie, et al. Utilization of direct and diffuse sunlight in a dye-sensitized solar cell silicon photovoltaic hybrid concentrator system. *The Journal of Physical Chemistry Letters*, 2(6):581–585, 2011.

[53] Roland Winston, Eli Yablonovitch, Lun Jiang, Bennett K Widyolar, Mahmoud Abdelhamid, Gregg Scranton, David Cygan, and Alexandr Kozlov. Hybrid solar collector using nonimaging optics and photovoltaic components. In *SPIE Optical Engineering+ Applications*, pages 957208–957208. International Society for Optics and Photonics, 2015.

[54] Anja Royne, Christopher J Dey, and David R Mills. Cooling of photovoltaic cells under concentrated illumination: a critical review. *Solar energy materials and solar cells*, 86(4):451–483, 2005.

[55] PJ Verlinden, AW Blakers, KJ Weber, J Babaei, V Everett, MJ Kerr, MF Stuckings, D Gordeev, and MJ Stocks. Sliver® solar cells: A new thin-crystalline silicon photovoltaic technology. *Solar energy materials and solar cells*, 90(18):3422–3430, 2006.

[56] Sven Ruhle, Akiba Segal, Ayelet Vilan, Sarah R Kurtz, Larissa Grinis, Arie Zaban, Igor Lubomirsky, and David Cahen. A two junction, four terminal photovoltaic device for enhanced light to electric power conversion using a low-cost dichroic mirror. *Journal of Renewable and Sustainable Energy*, 1(1):013106, 2009.

[57] Todd P Otanicar, Patrick E Phelan, Ravi S Prasher, Gary Rosengarten, and Robert A Taylor. Nanofluid-based direct absorption solar collector. *Journal of renewable and sustainable energy*, 2(3):033102, 2010.

[58] Todd P Otanicar, Patrick E Phelan, and Jay S Golden. Optical properties of liquids for direct absorption solar thermal energy systems. *Solar Energy*, 83(7):969–977, 2009.

[59] Robert A Taylor, Todd Otanicar, and Gary Rosengarten. Nanofluid-based optical filter optimization for pv/t systems. *Light: Science & Applications*, 1(10):e34, 2012.

[60] Drew DeJarnette, Todd Otanicar, Nick Brekke, Parameswar Hari, and Kenneth Roberts. Selective spectral filtration with nanoparticles for concentrating solar collectors. *Journal of Photonics for Energy*, 5(1):057008–057008, 2015.

[61] Felipe Crisostomo, Justin Becker, Sara Mesgari, Natasha Hjerrild, and Robert A Taylor. Desing and on-sun testing of a hybrid pvt prototype using a nanofluid-based selective absorption filter. In *European Energy Market (EEM), 2015 12th International Conference on the*, pages 1–5. IEEE, 2015.

[62] Marta Vivar and Vernie Everett. A review of optical and thermal transfer fluids used for optical adaptation or beam-splitting in concentrating solar systems. *Progress in Photovoltaics: Research and Applications*, 22(6):612–633, 2014.

[63] R Looser, M Vivar, and V Everett. Spectral characterisation and long-term performance analysis of various commercial heat transfer fluids (htf) as direct-absorption filters for cpv-t beam-splitting applications. *Applied Energy*, 113:1496–1511, 2014.

[64] Qing Hua Wang, Kourosh Kalantar-Zadeh, Andras Kis, Jonathan N Coleman, and Michael S Strano. Electronics and optoelectronics of two-dimensional transition metal dichalcogenides. *Nature nanotechnology*, 7(11):699–712, 2012.

[65] Hee Sung Lee, Sung-Wook Min, Youn-Gyung Chang, Min Kyu Park, Taewook Nam, Hyungjun Kim, Jae Hoon Kim, Sunmin Ryu, and Seongil Im. Mos2 nanosheet phototransistors with thickness-modulated optical energy gap. *Nano letters*, 12(7):3695–3700, 2012.

[66] Alaeddine Mokri and Mahieddine Emziane. Performance-based analysis of a double receiver photovoltaic sysytem. In *Proceedings of the World renewable energy congress, Linköping, Sweden*, 2011.

[67] Alaeddine Mokri and Mahieddine Emziane. A tandem four-terminal cpv system consisting of al 0.3 ga 0.7 as and ge solar cells. In *Energy Conference and Exhibition (EnergyCon), 2010 IEEE International*, pages 876–878. IEEE, 2010.

[68] Alaeddine Mokri and Mahieddine Emziane. A new approach for designing multi-receiver photovoltaic systems: Use of band-stop optical filters. In *Proceedings of the international symposium on environment friendly energies in electrical applications, Ghardaïa, Algeria*, 2010.

[69] A Mokri and M Emziane. A photovoltaic system with three solar cells and a band-stop optical filter. *Journal of Renewable and Sustainable Energy*, 3(2):023113, 2011.

[70] Alaeddine Mokri and Mahieddine Emziane. A novel concentrating photovoltaic system with two separate receivers. In *GCC Conference and Exhibition (GCC), 2011 IEEE*, pages 357–360. IEEE, 2011.

[71] Alaeddine Mokri and Mahieddine Emziane. Evaluation of a combined cpv and tpv system under high dni. In *GCC Conference and Exhibition (GCC), 2011 IEEE*, pages 158–161. IEEE, 2011.

[72] VP Khvostikov, AS Vlasov, SV Sorokina, NS Potapovich, N Kh Timoshina, MZ Shvarts, and VM Andreev. High-efficiency (η= 39.6%, am 1.5 d) cascade of photoconverters in solar splitting systems. *Semiconductors*, 45(6):792–797, 2011.

[73] Yuan Zhao and Ming-Yu Sheng. Design of spectrum splitting solar cell assemblies. In *Advances in Optoelectronics and Micro/Nano-Optics (AOM), 2010 OSA-IEEE-COS*, pages 1–3. IEEE, 2010.

[74] Kanglin Xiong, Shulong Lu, Jianrong Dong, Taofei Zhou, Desheng Jiang, Rongxin Wang, and Hui Yang. Light-splitting photovoltaic system utilizing two dual-junction solar cells. *Solar Energy*, 84(12):1975–1978, 2010.

[75] Yuan Zhao, Ming-Yu Sheng, Wei-Xi Zhou, Yan Shen, Er-Tao Hu, Jian-Bo Chen, Min Xu, Yu-Xiang Zheng, Young-Pak Lee, David W Lynch, et al. A solar photovoltaic system with ideal efficiency close to the theoretical limit. *Optics express*, 20(101):A28–A38, 2012.

[76] Alaeddine Mokri and Mahieddine Emziane. A triple-cell concentrator pv system with no current-matching and no lattice-matching constrains. In *Sustainability in Energy and Buildings*, pages 193–200. Springer, 2012.

[77] Bernhard Mitchell, Gerhard Peharz, Gerald Siefer, Marius Peters, Tobias Gandy, Jan Christoph Goldschmidt, Jan Benick, Stefan W Glunz, Andreas W Bett, and Frank Dimroth. Four-junction spectral beam-splitting photovoltaic receiver with high optical efficiency. *Progress in Photovoltaics: Research and Applications*, 19(1):61–72, 2011.

[78] A Goetzberger, JC Goldschmidt, M Peters, and P Löper. Light trapping, a new approach to spectrum splitting. *Solar Energy Materials and Solar Cells*, 92(12):1570–1578, 2008.

[79] Jason H Karp and Joseph E Ford. Planar micro-optic solar concentration using multiple imaging lenses into a common slab waveguide. In *SPIE Solar Energy+ Technology*, pages 74070D–74070D. International Society for Optics and Photonics, 2009.

[80] Jason H Karp, Eric J Tremblay, and Joseph E Ford. Planar micro-optic solar concentrator. *Optics express*, 18(2):1122–1133, 2010.

[81] Jason H Karp, Eric J Tremblay, and Joseph E Ford. Micro-optic solar concentration and next-generation prototypes. In *Photovoltaic Specialists Conference (PVSC), 2010 35th IEEE*, pages 000493–000497. IEEE, 2010.

[82] Jason H Karp, Eric J Tremblay, Justin M Hallas, and Joseph E Ford. Orthogonal and secondary concentration in planar micro-optic solar collectors. *Optics express*, 19(104):A673–A685, 2011.

[83] Lewis M Fraas, JE Avery, HX Huang, E Shifman, K Edmondson, and RR King. Toward 40% and higher solar cells in a new cassegrainian pv module. In *Photovoltaic Specialists Conference, 2005. Conference Record of the Thirty-first IEEE*, pages 751–753. IEEE, 2005.

[84] MICHAEL Ludowise and Lewis Fraas. High-concentration cassegrainian solar cell modules and arrays. *Solar Cells and Their Applications*, 217:337, 2010.

[85] Lewis M Fraas. Optimal cell selection for series connection in cassegrain pv module, August 9 2011. US Patent 7,994,417.

[86] LM Fraas, JE Avery, JE Strauch, and G Girard. Dual focus cassegrainian module can achieve >45% efficiency. In *Photovoltaic Specialists Conference (PVSC), 2009 34th IEEE*, pages 001169–001173. IEEE, 2009.

[87] Eric Christensen, Greg Schmidt, Blair Unger, and Duncan T Moore. Design, assembly, and testing of a spectral splitting solar concentrator module. In *International Optical Design Conference 2010*, pages 765211–765211. International Society for Optics and Photonics, 2010.

[88] Allen Barnett, Douglas Kirkpatrick, Christiana Honsberg, Duncan Moore, Mark Wanlass, Keith Emergy, Richard Schwartz, Dave Carlson, Stuart Bowden, Dan Aiken, et al. Milestones toward 50% efficient solar cell modules. Technical report, DTIC Document, 2007.

[89] Xiaoting Wang, Nick Waite, Paola Murcia, Keith Emery, Myles Steiner, Fouad Kiamilev, Keith Goossen, Christiana Honsberg, and Allen Barnett. Improved outdoor measurements for very high efficiency solar cell sub-modules. In *Photovoltaic Specialists Conference (PVSC), 2009 34th IEEE*, pages 000409–000414. IEEE, 2009.

[90] Xiaoting Wang and Allen Barnett. One lateral spectrum splitting concentrator photovoltaic architecture: Measurements of current assemblies and analysis of pathways to 40% efficient modules. In *Photovoltaic Specialists Conference (PVSC), 2010 35th IEEE*, pages 002745–002750. IEEE, 2010.

[91] Xiaoting Wang, Nick Waite, Paola Murcia, Keith Emery, Myles Steiner, Fouad Kiamilev, Keith Goossen, Christiana Honsberg, and Allen Barnett. Lateral spectrum splitting concentrator photovoltaics: direct measurement of component and submodule efficiency. *Progress in Photovoltaics: Research and Applications*, 20(2):149–165, 2012.

[92] Allen Barnett, Xiaoting Wang, Nick Waite, Paola Murcia, Christiana Honsberg, Doug Kirkpatrick, Dan Laubacher, Fouad Kiamilev, Keith Goossen, Mark Wanlass, et al. Initial test bed for very high efficiency solar cell. In *Photovoltaic Specialists Conference, 2008. PVSC'08. 33rd IEEE*, pages 1–7. IEEE, 2008.

[93] Martin A Green and Anita Ho-Baillie. Forty three per cent composite split-spectrum concentrator solar cell efficiency. *Progress in Photovoltaics: Research and Applications*, 18(1):42–47, 2010.

[94] L Fraas, J Avery, H Huang, Leonid Minkin, and Eli Shifman. Demonstration of a 33% efficient cassegrainian solar module. In *Photovoltaic Energy Conversion, Conference Record of the 2006 IEEE 4th World Conference on*, volume 1, pages 679–682. IEEE, 2006.

[95] Jason H Karp and Joseph E Ford. Multiband solar concentrator using transmissive dichroic beamsplitting. In *Solar Energy+ Applications*, pages 70430F–70430F. International Society for Optics and Photonics, 2008.

[96] Akiba Segal, Michael Epstein, and Amnon Yogev. Hybrid concentrated photovoltaic and thermal power conversion at different spectral bands. *Solar Energy*, 76(5):591–601, 2004.

[97] Chun-Hui Shou, Zhong-Yang Luo, Tao Wang, Wei-Dong Shen, Gary Rosengarten, Cheng Wang, Ming-Jiang Ni, and Ke-Fa Cen. A dielectric multilayer filter for combining photovoltaics with a stirling engine for improvement of the efficiency of solar electricity generation. *Chin Phys Lett*, 28:8402, 2011.

[98] Christopher M Maghanga, Gunnar A Niklasson, Claes G Granqvist, and Mghendi Mwamburi. Spectrally selective reflector surfaces for heat reduction in concentrator solar cells: modeling and applications of tio 2: Nb-based thin films. *Applied optics*, 50(19):3296–3302, 2011.

[99] Anne G Imenes and David R McKenzie. Flat-topped broadband rugate filters. *Applied optics*, 45(30):7841–7850, 2006.

[100] Shouli Jiang, Peng Hu, Songping Mo, and Zeshao Chen. Optical modeling for a two-stage parabolic trough concentrating photovoltaic/thermal system using spectral beam splitting technology. *Solar Energy Materials and Solar Cells*, 94(10):1686–1696, 2010.

[101] Shouli Jiang, Gang Wang, Peng Hu, Zeshao Chen, and Lei Jia. The design of beam splitter for two-stage reflective spectral beam splitting concentrating pv/thermal system. In *Power and Energy Engineering Conference (APPEEC), 2011 Asia-Pacific*, pages 1–4. IEEE, 2011.

[102] Jiang Shou-Li, Hu Peng, Mo Song-ping, and Chen Ze-shao. Modeling for two-stage dish concentrating spectral beam splitting photovoltaic/thermal system. In *Power and Energy Engineering Conference, 2009. APPEEC 2009. Asia-Pacific*, pages 1–4. IEEE, 2009.

[103] Xing Ju, Zhifeng Wang, Gilles Flamant, Peng Li, and Wenyu Zhao. Numerical analysis and optimization of a spectrum splitting concentration photovoltaic–thermoelectric hybrid system. *Solar Energy*, 86(6):1941–1954, 2012.

[104] D Kraemer, L Hu, A Muto, X Chen, G Chen, and M Chiesa. Photovoltaic-thermoelectric hybrid systems: A general optimization methodology. *Applied Physics Letters*, 92(24):243503, 2008.

[105] Jean-Pierre Fleurial. Thermoelectric power generation materials: Technology and application opportunities. *JOM*, 61(4):79–85, 2009.

[106] Jiafei Zhao, Zhongyang Luo, Yanmei Zhang, Chunhui Shou, and Mingjiang Ni. Optimal design and performance analysis of a low concentrating photovoltaic/thermal system using the direct absorption collection concept. In *Power and Energy Engineering Conference (APPEEC), 2010 Asia-Pacific*, pages 1–6. IEEE, 2010.

[107] Todd P Otanicar, Ihtesham Chowdhury, Ravi Prasher, and Patrick E Phelan. Band-gap tuned direct absorption for a hybrid concentrating solar photovoltaic/thermal system. *Journal of Solar Energy Engineering*, 133(4):041014, 2011.

[108] Robert A Taylor, Todd P Otanicar, Yasitha Herukerrupu, Fabienne Bremond, Gary Rosengarten, Evatt R Hawkes, Xuchuan Jiang, and Sylvain Coulombe. Feasibility of nanofluid-based optical filters. *Applied optics*, 52(7):1413–1422, 2013.

[109] Mark D Redwood, Raveen Dhillon, Rafael L Orozco, Xu Zhang, David J Binks, Mark Dickinson, and Lynne E Macaskie. Enhanced photosynthetic output via dichroic beam-sharing. *Biotechnology letters*, 34(12):2229–2234, 2012.

[110] RJ Schwartz and MD Lammert. Silicon solar cells for high concentration applications. In *Electron Devices Meeting, 1975 International*, volume 21, pages 350–352. IEEE, 1975.

[111] Emmanuel Van Kerschaver and Guy Beaucarne. Back-contact solar cells: A review. *Progress in Photovoltaics: Research and Applications*, 14(2):107–123, 2006.

[112] Xiangning Lu, Tielin Shi, Qi Xia, and Guanglan Liao. Thermal conduction analysis and characterization of solder bumps in flip chip package. *Applied Thermal Engineering*, 36:181–187, 2012.

[113] Amy S Fleischer, Li-hsin Chang, and Barry C Johnson. The effect of die attach voiding on the thermal resistance of chip level packages. *Microelectronics Reliability*, 46(5):794–804, 2006.

[114] Stefano Baricordi, Gabriele Calabrese, Federico Gualdi, Vincenzo Guidi, Matteo Pasquini, Luana Pozzetti, and Donato Vincenzi. A joint thermal–electrical analysis of void formation effects on concentrator silicon solar cells solder layer. *Solar Energy Materials and Solar Cells*, 111:133–140, 2013.

[115] Priyanka Singh and N Mr Ravindra. Temperature dependence of solar cell performance—an analysis. *Solar Energy Materials and Solar Cells*, 101:36–45, 2012.

[116] YP Varshni. Temperature dependence of the energy gap in semiconductors. *Physica*, 34(1):149–154, 1967.

[117] Martin A Green. Solar cell fill factors: General graph and empirical expressions. *Solid-State Electronics*, 24(8):788–789, 1981.

[118] RS Ottens, Volker Quetschke, Stacy Wise, AA Alemi, Ramsey Lundock, Guido Mueller, David H Reitze, David B Tanner, and Bernard F Whiting. Near-field radiative heat transfer between macroscopic planar surfaces. *Physical Review Letters*, 107(1):014301, 2011.

[119] Rodolphe Vaillon, Lucile Robin, Cristian Muresan, and Christophe Ménézo. Modeling of coupled spectral radiation, thermal and carrier transport in a silicon photovoltaic cell. *International journal of heat and mass transfer*, 49(23):4454–4468, 2006.

[120] Kenny C Otiaba, RS Bhatti, Ndy N Ekere, Sabuj Mallik, MO Alam, Emeka H Amalu, and Mathias Ekpu. Numerical study on thermal impacts of different void patterns on performance of chip-scale packaged power device. *Microelectronics Reliability*, 52(7):1409–1419, 2012.

[121] Rolf Diehm, Mathias Nowottnick, and Uwe Pape. Reduction of voids in solder joints an alternative to vacuum soldering. *Proc. of the IPC APEX EXPO, San Diego, CA*, 28, 2012.

[122] Reference Solar Spectral Irradiance: Air Mass 1.5. http://rredc.nrel.gov/solar/spectra/am1.5/.

[123] Eckhard Lüpfert, Klaus Pottler, Steffen Ulmer, Klaus-J Riffelmann, Andreas Neumann, and Björn Schiricke. Parabolic trough optical performance analysis techniques. *Journal of solar energy engineering*, 129(2):147–152, 2007.

[124] JB Blackmon. Development and performance of a digital image radiometer for heliostat evaluation at solar one. *Journal of solar energy engineering*, 107(4):315–321, 1985.

[125] Glen Johnston. Focal region measurements of the 20m tiled dish at the australian national university. *Solar Energy*, 63(2):117–124, 1998.

[126] Steffen Ulmer, Wolfgang Reinalter, Peter Heller, Eckhard Lüpfert, and Diego Martinez. Beam characterization and improvement with a flux mapping system for dish concentrators. In *ASME Solar 2002: International Solar Energy Conference*, pages 285–292. American Society of Mechanical Engineers, 2002.

[127] I Antón, D Pachón, and G Sala. Characterization of optical collectors for concentration photovoltaic applications. *Progress in Photovoltaics: Research and Applications*, 11(6):387–405, 2003.

[128] Eckhard Lüpfert, Andreas Neumann, Klaus-J Riffelmann, and Steffen Ulmer. Comparative flux measurement and raytracing for the characterization of the focal region of solar parabolic trough collectors. In *ASME 2004 International Solar Energy Conference*, pages 689–694. American Society of Mechanical Engineers, 2004.

[129] Björn Schiricke, Robert Pitz-Paal, Eckhard Lüpfert, Klaus Pottler, Markus Pfänder, Klaus-J Riffelmann, and Andreas Neumann. Experimental verification of optical modeling of parabolic trough collectors by flux measurement. *Journal of Solar Energy Engineering*, 131(1):011004, 2009.

[130] Jawad Sarwar, Grigoris Georgakis, Robert LaChance, and Nesrin Ozalp. Description and characterization of an adjustable flux solar simulator for solar thermal, thermochemical and photovoltaic applications. *Solar Energy*, 100:179–194, 2014.

[131] Hyunjin Lee, Kwankyo Chai, Jongkyu Kim, Sangnam Lee, Hwanki Yoon, Changkyun Yu, and Yongheack Kang. Optical performance evaluation of a solar furnace by measuring the highly concentrated solar flux. *Energy*, 66:63–69, 2014.

[132] A Neumann and U Groer. Experimenting with concentrated sunlight using the DLR solar furnace. *Solar Energy*, 58(4):181–190, 1996.

[133] M Schubnell, J Keller, and A Imhof. Flux density distribution in the focal region of a solar concentrator system. *Journal of solar energy engineering*, 113(2):112–116, 1991.

[134] Antonio Parretta, Carlo Privato, Giuseppe Nenna, Andrea Antonini, and Marco Stefancich. Monitoring of concentrated radiation beam for photovoltaic and thermal solar energy conversion applications. *Applied optics*, 45(30):7885–7897, 2006.

[135] V.N. Mahajan. *Optical Imaging and Aberrations: Ray geometrical optics*. Number pts. 1-2 in Optical Imaging and Aberrations. SPIE Optical Engineering Press, 1998.

[136] Clifford K Ho and Siri S Khalsa. A photographic flux mapping method for concentrating solar collectors and receivers. *Journal of Solar Energy Engineering*, 134(4):041004, 2012.

[137] S.F. Ray. *Applied photographic optics: lenses and optical systems for photography, film, video, electronic and digital imaging*. Focal, 2002.

[138] Peter B Catrysse, Xinqiao Liu, and Abbas El Gamal. Qe reduction due to pixel vignetting in cmos image sensors. In *Electronic Imaging*, pages 420–430. International Society for Optics and Photonics, 2000.

[139] Jean Yves Bouguet. Camera calibration toolbox for matlab, 2013.

[140] Gore diffuse reflector, 2010.

[141] Yuanjie Zheng, Stephen Lin, Chandra Kambhamettu, Jingyi Yu, and Sing Bing Kang. Single-image vignetting correction. *Pattern Analysis and Machine Intelligence, IEEE Transactions on*, 31(12):2243–2256, 2009.

[142] Dan B Goldman and Jiun-Hung Chen. Vignette and exposure calibration and compensation. In *Computer Vision, 2005. ICCV 2005. Tenth IEEE International Conference on*, volume 1, pages 899–906. IEEE, 2005.

[143] Seon Joo Kim and Marc Pollefeys. Robust radiometric calibration and vignetting correction. *Pattern Analysis and Machine Intelligence, IEEE Transactions on*, 30(4):562–576, 2008.

[144] Robert Taylor, Sylvain Coulombe, Todd Otanicar, Patrick Phelan, Andrey Gunawan, Wei Lv, Gary Rosengarten, Ravi Prasher, and Himanshu Tyagi. Small particles, big impacts: A review of the diverse applications of nanofluids. *Journal of Applied Physics*, 113(1):011301, 2013.

[145] John E Minardi and Henry N Chuang. Performance of a "black" liquid flat-plate solar collector. *Solar Energy*, 17(3):179–183, 1975.

[146] V Everett, AW Blakers, J Cotsell, J Harvey, R van Scheppingen, and D Walters. Improving the efficiency of linear concentrator receiver systems. In *Solar09, the 47th ANZSES Annual Conference, Townsville*, 2009.

[147] Vernie Everett, Daniel Walter, Judy Harvey, Marta Vivar, R Van Scheppingen, S Surve, A Blakers, P Le Lievre, M Greaves, and A Tanner. A closed loop tracking system for a linear fresnel hybrid pv/thermal micro-concentrator system. In *25th European Photovoltaic Solar Energy Conference and Exhibition (25th EU PVSEC)/5th World Conference on Photovoltaic Energy Conversion (WCPEC-5), Valencia (Spain)*, pages 1063–1065, 2010.

[148] Vernie Everett, Daniel Walter, Judy Harvey, Marta Vivar, R Van Scheppingen, S Surve, A Blakers, P Le Lievre, M Greaves, and A Tanner. Enhanced longitudinal and lateral flux uniformity for linear fresnel reflectors in concentrating photovoltaic systems. In *25th European Photovoltaic Solar Energy Conference and Exhibition (25th EU PVSEC)/5th World Conference on Photovoltaic Energy Conversion (WCPEC-5), Valencia (Spain)*, pages 1060–1062, 2010.

[149] Tanzeen Sultana, Graham L Morrison, and Gary Rosengarten. Thermal performance of a novel rooftop solar micro-concentrating collector. *Solar Energy*, 86(7):1992–2000, 2012.

[150] D Walter, V Everett, M Vivar, J Harvey, R Van Scheppingen, S Surve, J Muric-Nesic, A Blakers, Andreas W Bett, Robert D McConnell, et al. A monolithic microconcentrator receiver for a hybrid pv-thermal system: Preliminary performance. In *Aip Conference Proceedings*, volume 1277, page 70, 2010.

[151] M Vivar, V Everett, M Fuentes, A Blakers, A Tanner, P Le Lievre, and M Greaves. Initial field performance of a hybrid cpv-t microconcentrator system. *Progress in Photovoltaics: Research and Applications*, 21(8):1659–1671, 2013.

[152] the Radiant Zemax LLC. Zemax 13 , 2013.

[153] National Renewable Energy Laboratory (NREL). Reference solar spectral irradiance: Air mass 1.5 , 2014.

[154] M.F. Modest. *Radiative Heat Transfer*. Elsevier Science, 2013.

[155] Openfilters , 2014.

[156] Stéphane Larouche and Ludvik Martinu. Openfilters: open-source software for the design, optimization, and synthesis of optical filters. *Applied optics*, 47(13):C219–C230, 2008.

[157] Vernie Everett, Daniel Walter, Judy Harvey, Marta Vivar, R Van Scheppingen, S Surve, A Blakers, P Le Lievre, M Greaves, and A Tanner. A linear fresnel hybrid pv/thermal micro-concentrator system for rooftop integration. In *25th European Photovoltaic Solar Energy Conference and Exhibition (25th EU PVSEC)/5th World Conference on Photovoltaic Energy Conversion (WCPEC-5)*, pages 3937–3941, 2010.

[158] M.J. Weber. *Handbook of Optical Materials*. Laser & Optical Science & Technology. Taylor & Francis, 2002.

[159] Cameron Stanley, Ahmad Mojiri, Nitin Karwa, and Gary Rosengarten. Thermal performance analysis of a concentrating beam splitting hybrid pvt collector. In *EuroSun 2014, AIX LES BAINS, France*, 2014.

[160] KE Remitz, N Neuroth, and B Speit. Semiconductor doped glass as a nonlinear material. *Materials Science and Engineering: B*, 9(4):413–416, 1991.

[161] GianPiero Banfi, Vittorio Degiorgio, and Burkhard Speit. Neutron scattering investigation of the structure of semiconductor-doped glasses. *Journal of applied physics*, 74(11):6925–6935, 1993.

[162] Martin Kull and Jean-Louis Coutaz. Intensity-dependent absorption and luminescence in semiconductor-doped glasses. *JOSA B*, 7(8):1463–1472, 1990.

[163] Advanced Optics SCHOTT Pasadena. Glass filters. 2009.

[164] Yiliang Wu, Vernie Everett, Elizabeth Thomsen, and Andrew Blakers. Investigation of the temperature dependence of the optical properties of thermal transfer fluids for hybrid cpv-t systems. In *9TH INTERNATIONAL CONFERENCE ON CONCENTRATOR PHOTOVOLTAIC SYSTEMS: CPV-9*, volume 1556, pages 84–87. AIP Publishing, 2013.

[165] Felipe Crisostomo, Robert A Taylor, Desiree Surjadi, Ahmad Mojiri, Gary Rosengarten, and Evatt R Hawkes. Spectral splitting strategy and optical model for the development of a concentrating hybrid pv/t collector. *Applied Energy*, 141:238–246, 2015.

[166] Cameron Stanley, Ahmad Mojiri, Nitin Karwa, and Gary Rosengarten. Thermal performance analysis of concentrating beam splitting hybrid pvt collectors. EuroSun, 2014.

Appendix A

Uncertainty analysis

In this section, the uncertainty analysis of the experimental results presented in Chapter 6 are outlined. To do so, the calculations and corresponding assumptions are explained.

A.1 Tube diameter

The cross-section of the high temperature glass tube has been presented in Figure A.1.

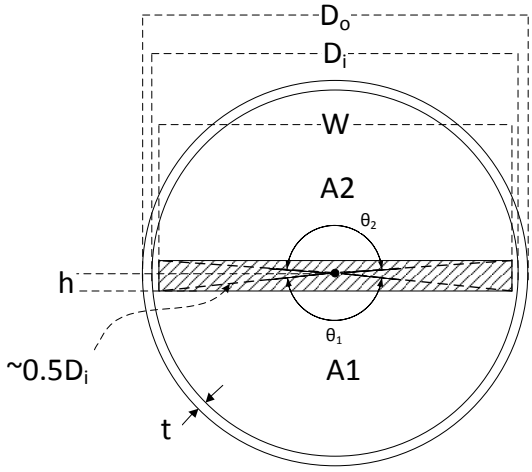

Fig. A.1 The schematic of the tube cross-section

In this figure, from the manufacturer data:
$D_o = 0.028\ m$

$t = 0.0014\ m$

$$D_i = D_o - 2t$$

$$B_{D_o} = 0.00025\ m$$

$$B_t = 0.00005\ m$$

Here, B is the bias error.

$$\mathrm{d}D_i/\mathrm{d}D_o = 1$$

$$\mathrm{d}D_i/\mathrm{d}t = -2$$

$$B_{D_i} = \sqrt{(\frac{\mathrm{d}D_i}{\mathrm{d}D_o} \times B_{D_o})^2 + (\frac{\mathrm{d}D_i}{\mathrm{d}t} \times B_t)^2 + 2 \times (\frac{\mathrm{d}D_i}{\mathrm{d}D_o} \times \frac{\mathrm{d}D_i}{\mathrm{d}t} \times B_{Do} \times B_t)}$$

$$U_{D_i} = B_{D_i}$$

$$U_{D_i}\% = B_{D_i}/D_i$$

A.2 Hydraulic diameter of the glass tube

The SDG filter bisects the tube cross-section into 2 semi-circle regions. This has been presented in Figure A.1. Due to the manufacturing tolerances, the filter sits slightly below the middle line of the tube. h is the distance of the bottom of the SDG from the centre of the tube which is ideally 1. Using these values, other parameters can be calculated as below:

$$\theta_1 = 2 \times \arccos(\frac{2h}{D_i})$$

$$P_1 = W + \theta_1 \times \frac{D_i}{2}$$

$$A_1 = 0.5 \times (\theta_1 - \sin(\theta_1)) \times (\frac{D_i}{2})^2$$

The hydraulic diameter can be calculated as below:

$D_{hyd1} = \frac{4A_1}{P_1}$

Similar calculations can be applied for the top segment of the cross-section:

$\theta_2 = 2 \times acos(\frac{(4-2h)}{D_i})$

$P_2 = W + \theta_2 \times \frac{D_i}{2}$

$A_2 = 0.5 \times (\theta_2 - \sin(\theta_2)) \times (\frac{D_i}{2})^2$

$D_{hyd2} = \frac{4A_2}{P_2}$
The total equivalent hydraulic diameter can be calculate as:
$D_{hyd} = D_{hyd1} + D_{hyd2}$
Using the above equations, the uncertainty propagation terms can be calculated as below:

$\frac{\mathrm{d}D_{hyd1}}{\mathrm{d}D_i} = 4 \times [\frac{1}{P_1}\frac{\mathrm{d}A_1}{\mathrm{d}D_i} + A_1 \frac{\frac{-\mathrm{d}P_1}{\mathrm{d}D_i}}{{P_1}^2}]$

To calculate the value of this equation, the chain rule can be applied:

$\frac{\mathrm{d}A_1}{\mathrm{d}D_i} = \frac{\partial A_1}{\partial \theta_1}\frac{\partial \theta_1}{\partial D_i} + \frac{\partial A_1}{\partial D_i}$

$\frac{\mathrm{d}P_1}{\mathrm{d}D_i} = \frac{\partial P_1}{\partial \theta_1}\frac{\partial \theta_1}{\partial D_i} + \frac{\partial P_1}{\partial D_i}$

$\frac{\partial A_1}{\partial \theta_1} = 0.5(\frac{D_i}{2})^2(1 - cos(\theta_1))$

$\frac{\partial \theta_1}{\partial D_i} = \frac{4h}{{D_i}^2} \times \frac{1}{\sqrt{1-(\frac{2h}{D_i})^2}}$

$\frac{\partial A_1}{\partial D_i} = 0.5(\theta_1 + sin(\theta_1)) \times \frac{D_i}{2}$

$\frac{\partial P_1}{\partial \theta_1} = \frac{D_i}{2}$
$\frac{\partial P_1}{\partial D_i} = \frac{\theta_1}{2}$

$\frac{\mathrm{d}D_{hyd1}}{\mathrm{d}h} = 4 \times [\frac{1}{P_1}\frac{\mathrm{d}A_1}{\mathrm{d}h} + A_1 \frac{\frac{-\mathrm{d}P_1}{\mathrm{d}h}}{{P_1}^2}]$

Which again:
$\frac{\mathrm{d}A_1}{\mathrm{d}h} = \frac{\partial A_1}{\partial \theta_1}\frac{\partial \theta_1}{\partial h}$

$$\frac{dP_1}{dh} = \frac{\partial P_1}{\partial \theta_1}\frac{\partial \theta_1}{\partial h}$$

$$\frac{\partial \theta_1}{\partial h} = \frac{4}{D_i} \times \frac{-1}{\sqrt{1-(\frac{2h}{D_i})^2}}$$

Similar terms can be derived for D_{hyd2}:

$$\frac{dD_{hyd2}}{dD_i} = 4 \times [\frac{1}{P_2}\frac{dA_2}{dD_i} + A_2 \frac{\frac{-dP_2}{dD_i}}{{P_2}^2}]$$

$$\frac{dA_2}{dD_i} = \frac{\partial A_2}{\partial \theta_2}\frac{\partial \theta_2}{\partial D_i} + \frac{\partial A_2}{\partial D_i}$$

$$\frac{dP_2}{dD_i} = \frac{\partial P_2}{\partial \theta_2}\frac{\partial \theta_2}{\partial D_i} + \frac{\partial P_2}{\partial D_i}$$

$$\frac{\partial A_2}{\partial \theta_2} = 0.5(\frac{D_i}{2})^2(1 - cos(\theta_2))$$

$$\frac{\partial \theta_2}{\partial D_i} = \frac{8-4h}{{D_i}^2} \times \frac{1}{\sqrt{1-(\frac{4-2h}{D_i})^2}}$$

$$\frac{\partial A_2}{\partial D_i} = 0.5(\theta_2 - sin(\theta_2)) \times \frac{D_i}{2}$$

$$\frac{\partial P_2}{\partial \theta_2} = \frac{D_i}{2}$$

$$\frac{\partial P_2}{\partial D_i} = \frac{\theta_2}{2}$$

$$\frac{dD_{hyd2}}{dh} = 4 \times [\frac{1}{P_2}\frac{dA_2}{dh} + A_2 \frac{\frac{-dP_2}{dh}}{{P_2}^2}]$$

For which:

$$\frac{dA_2}{dh} = \frac{\partial A_2}{\partial \theta_2}\frac{\partial \theta_2}{\partial h}$$

$$\frac{dP_2}{dh} = \frac{\partial P_2}{\partial \theta_2}\frac{\partial \theta_2}{\partial h}$$

$$\frac{\partial \theta_2}{\partial h} = \frac{4}{D_i} \times \frac{-1}{\sqrt{1-(\frac{4-2h}{D_i})^2}}$$

A.3 Extrusion cooling channel diameter

The uncertainty of the extrusion cooling channel was calculated based on the tolerances mentioned in the CAD model sent to the manufacturer and the die uncertainties:

$B_{CAD} = 0.0001\ m$

$B_{die} = 0.00025\ m$

$B_{extr} = \sqrt{B_{CAD}^2 + B_{die}^2}$

A.4 Temperature read by RTDs

Calibrated RTDs with the below uncertainties were used to measure the temperature at the inlet and outlet of each channel:

$B_{T_{H,in}} = 0.1149\ K$

$B_{T_{H,out}} = 0.1249\ K$

$B_{T_{C,in}} = 0.1201\ K$

$B_{T_{C,out}} = 0.1179\ K$

$B_{T_{amb}} = 0.25\ K$

The random errors taken as 2 times the standard deviations during the measurement are:

$s_{T_{H,in}} = 0.001\ K$

$s_{T_{H,out}} = 0.001\ K$

$s_{T_{C,in}} = 0.001\ K$

$s_{T_{C,out}} = 0.001\ K$

$s_{T_{amb}} = 0.01\ K$

The total uncertainty of the RTD measurements can be calculated as:

$U_{T_{H,in}} = \sqrt{B_{T_{H,in}}^2 + s_{T_{H,in}}^2}$

$U_{T_{H,out}} = \sqrt{B_{T_{H,out}}^2 + s_{T_{H,out}}^2}$

$U_{T_{C,in}} = \sqrt{B_{T_{C,in}}^2 + s_{T_{C,in}}^2}$

$U_{T_{C,out}} = \sqrt{B_{T_{C,out}}^2 + s_{T_{C,out}}^2}$

$U_{T_{amb}} = \sqrt{B_{T_{amb}}^2 + s_{T_{amb}}^2}$

A.5 PG flow rate

The Coriolis flow meter had a bias error of 0.2% of the flow rate (acquired from the manufacturer data sheet). The random error was estimated as 2 times the standard deviation of the readings for a constant operating temperature.
$B_{\dot{m}_{PG}} = 0.002 \times \dot{m}_{PG}\ kg/s$
$s_{\dot{m}_{PG}} = 0.000362\ kg/s$

Hence,
$U_{\dot{m}_{PG}} = \sqrt{B_{\dot{m}_{PG}}^2 + s_{\dot{m}_{PG}}^2}$

A.6 Water flow rate

The water flow rate was measured using a simple catch and time approach. The volume of the flask was 0.001 m^3. It took about 32.8 s to fill the flask. The water temperature was assumed to be the mean of $T_{C,in}$ and $T_{C,out}$. Time is assumed to be measured with an accuracy of 0.2 s. The volume of water in the flask was measured with an accuracy of 5ml.
$B_{vol} = 0.000005\ m^3$
$B_{time} = 0.2\ s$

$\dot{m}_W = \frac{\rho \times vol.}{time}$

Hence,
$\frac{\mathrm{d}(\dot{m}_W)}{\mathrm{d}(vol.)} = \frac{\rho}{time}$

$\frac{\mathrm{d}(\dot{m}_W)}{\mathrm{d}(time)} = \frac{-\rho \times vol.}{time^2}$

and,
$B_{\dot{m}_W} = \sqrt{(\frac{\mathrm{d}(\dot{m}_W)}{\mathrm{d}(vol.)} \times B_{vol.})^2 + (\frac{\mathrm{d}(\dot{m}_W)}{\mathrm{d}(time)} \times B_{time})^2}$

The random error is assumed to be the same as bias error. Then,
$U_{\dot{m}_W} = \sqrt{2} \times B_{\dot{m}_W}$

A.7 Dynamic viscosity of PG

Empirical correlations have been used here to estimate the PG viscosity and its uncertainties. The viscosity of PG-water mixture can be estimated as (from the work published by Sun and Teja):

$\ln(\mu) = w_1 \ln \mu_{PG} + w_2 \ln \mu_W + (\ln \mu_{PG} - \ln \mu_w) w_1 w_2 (Z_4 + Z_5 w_1 + Z_6 T + Z_7 w_1^2)$

$w_1 + w_2 = 1$

The viscosity of pure PG as a function of temperature is:

$\ln(\mu_{PG}) = Z_1 + Z_2 \times T + Z_3 \times T^2$

For water,

$\ln(\mu_W) = -3.758023 + 590.9808/(T + 137.2645)$

The coefficients are listed in Table A.1. w_1 and w_2 are the volume fractions of PG and water

Table A.1 Coefficients of the viscosity correlations

Coefficient	Value
Z_1	-3.9701
Z_2	1000.8
Z_3	-104.10
Z_5	-5.0007
Z_6	9.8106×10^{-4}
Z_7	3.2452

respectively. For pure PG, $w_2 = 0$. B_{w_1} was assumed to be 1% and B_T was assumed to be equal to $U_{T_{H,in}}$. Using the above equations and values, the uncertainty associated with the viscosity values can be calculated as below:

$U_\mu = \sqrt{(\frac{\partial \mu}{\partial w_1} \times B_{w_1})^2 + (\frac{\partial \mu}{\partial T} \times B_T)^2}$

A.8 Re number

The uncertainty associated with the Re number of the flow in the high temperature channel can now be calculated using the data presented in the previous sections.

$Re = \frac{\dot{m}_{PG} D_{hdr}}{A\mu}$

$$U_{Re} = \sqrt{(\frac{\partial Re}{\partial \dot{m}_{PG}} \times U_{\dot{m}_{PG}})^2 + (\frac{\partial Re}{\partial D_{hyd}} \times U_{D_{hyd}})^2 + (\frac{\partial Re}{\partial \mu} \times U_{\mu})^2}$$

A.9 Wind speed

The uncertainty of the measured wind speed was calculated based on the manufacturers data: $B_{wind} = 0.11\ m/s$

The random error was assumed to be $0.1\ m/s$. Hence:

$$U_{wind} = \sqrt{B_{wind}^2 + s_{wind}^2}$$

A.10 Radiation

The solar radiation was measured using a pair of pyronometers. The uncertainty associated with their readings are based on the manufacturers data. It should be noted that the installation bias errors were not possible to quantify at the time of running the experiments. Hence this section should be refined in future.

$B_0 = 3\ W/m^2$
$B_{stability} = 0.015 \times G\ W/m^2$
$B_{non-linearity} = 0.005 \times G\ W/m^2$
$B_{directional} = 15\ W/m^2$
$B_{spectral} = 0.03 \times G\ W/m^2$
$B_{temperature} = 0.02 \times G\ W/m^2$
$B_{tilt} = 0.0025 \times G\ W/m^2$
$B_{calib} = 46\ W/m^2$

$$B_{radiation} = \sqrt{(B_0^2 + B_{stability}^2 + B_{non-linearity}^2 + B_{directional}^2 + B_{spectral}^2 + B_{temperature}^2 + B_{tilt}^2 + B_{calib}^2)}$$

A.11 PG specific heat

The specific heat value was calculated at the mean temperature of PG:

$T_{mean} = \frac{T_{H,in}+T_{H,out}}{2}$
From empirical values,

$$C_{pPG} = 5.8 \times T_{mean} + 2370.6$$

$$\frac{dT_{mean}}{dT_{H,in}} = 0.5$$

$$\frac{dT_{mean}}{dT_{H,out}} = 0.5$$

$$\frac{dC_{pPG}}{dT_{mean}} = 5.8$$

$$U_{C_{pPG},T_{mean}} = 5.8 \times U_{T_{mean}}$$

From curve fitting to the measured C_{pPG} values:
$s_{C_{pPG}} = 12.4\ J/kgK$

$$U_{C_{pPG}} = \sqrt{s^2_{C_{pPG}} + U^2_{C_{pPG},T_{mean}}}$$

A.12 Water specific heat

The specific heat for water is calculated in a similar way to the specific heat of PG:

$T_{W,mean} = \frac{T_{C,in}+T_{C,out}}{2}$
From empirical values,

$$C_{p,W} = 1000 \times (-9.035 \times 10^{-11} \times T^5_{W,mean} + 2.4338 \times 10^{-8} \times T^4_{W,mean} - 2.5574 \times 10^{-6}$$

$$\times T^3_{W,mean} + 1.3938 \times 10^{-4} \times T^2_{W,mean} - 3.8157 \times 10^{-3} \times T_{W,mean})$$

$$\frac{dT_{W,mean}}{dT_{c,in}} = 0.5$$

$$\frac{dT_{W,mean}}{dT_{C,out}} = 0.5$$

$$U_{T_{W,mean}} = \sqrt{(\frac{dT_{W,mean}}{dT_{C,in}} \times U_{T_{C,in}})^2 + (\frac{dT_{W,mean}}{dT_{C,out}} \times U_{T_{C,out}})^2}$$

$$U_{C_{p,W},T_{W,mean}} = \frac{\partial C_{p,W}}{\partial T_{W,mean}} \times U_{T_{W,mean}}$$

From curve fitting to the measured C_{pPG} values:
$s_{C_{p,W}} = 1.072\ J/kgK$

$$U_{C_{p,W}} = \sqrt{s^2_{C_{p,W}} + U^2_{C_{p,W},T_{W,mean}}}$$

A.13 Heat delivered by PG, $\dot{Q}_{hot}$

$$\dot{Q}_{hot} = \dot{m}_{PG} \times C_{p,PG} \times (T_{H,out} - T_{H,in})$$

$$\frac{\partial \dot{Q}_{hot}}{\partial \dot{m}_{PG}} = C_{p,PG} \times (T_{H,out} - T_{H,in})$$

$$\frac{\partial \dot{Q}_{hot}}{\partial C_{p,PG}} = \dot{m}_{PG} \times (T_{H,out} - T_{H,in})$$

$$\frac{\partial \dot{Q}_{hot}}{\partial T_{H,out}} = C_{p,PG} \times \dot{m}_{PG}$$

$$\frac{\partial \dot{Q}_{hot}}{\partial T_{H,in}} = -C_{p,PG} \times \dot{m}_{PG}$$

$$U_{\dot{Q}_{hot}} = \sqrt{(\frac{\partial \dot{Q}_{hot}}{\partial \dot{m}_{PG}} \times U_{\dot{m}_{PG}})^2 + (\frac{\partial \dot{Q}_{hot}}{\partial C_{p,PG}} \times U_{C_{p,PG}})^2 + (\frac{\partial \dot{Q}_{hot}}{\partial T_{H,out}} \times U_{T_{H,out}})^2 + (\frac{\partial \dot{Q}_{hot}}{\partial T_{H,in}} \times U_{T_{H,in}})^2}$$

A.14 Heat delivered by water, $\dot{Q}_{Cold}$

$$\dot{Q}_{cold} = \dot{m}_W \times C_{p,W} \times (T_{C,out} - T_{C,in})$$

$$\frac{\partial \dot{Q}_{cold}}{\partial \dot{m}_W} = C_{p,W} \times (T_{C,out} - T_{C,in})$$

$$\frac{\partial \dot{Q}_{cold}}{\partial C_{p,W}} = \dot{m}_W \times (T_{C,out} - T_{C,in})$$

$$\frac{\partial \dot{Q}_{cold}}{\partial T_{C,out}} = C_{p,w} \times \dot{m}_W$$

$$\frac{\partial \dot{Q}_{cold}}{\partial T_{C,in}} = -C_{p,W} \times \dot{m}_W$$

$$U_{\dot{Q}_{cold}} = \sqrt{(\frac{\partial \dot{Q}_{cold}}{\partial \dot{m}_W} \times U_{\dot{m}_W})^2 + (\frac{\partial \dot{Q}_{cold}}{\partial C_{p,W}} \times U_{C_{p,W}})^2 + (\frac{\partial \dot{Q}_{cold}}{\partial T_{C,out}} \times U_{T_{C,out}})^2 + (\frac{\partial \dot{Q}_{cold}}{\partial T_{C,in}} \times U_{T_{C,in}})^2}$$

A.15 PV power, $\dot{Q}_{elec}$

The PV output was measured using two different DC loads. The bias errors of 3711A electronic load from the manufacturer data is:
$B_{V_1} = 0.002 \times V_1 + 0.3$
$B_{I_1} = 0.002 \times I_1 + 0.003$

The second DC load is Kikusui PLZ 1004. From the manufacturer data for this one:

$B_{V_2} = 0.001 \times V_2 + 0.150$
$B_{I_2} = 0.002 \times I + 0.002$

The maximum value of each parameter was taken as the bias error:
$B_V = max(B_{V_1}, B_{V_2})$
$B_I = max(B_{I_1}, B_{I_2})$

The power from the PV module is calculated as below:
$\dot{Q}_{elec} = I \times V$

Hence,

$$\frac{\partial \dot{Q}_{elec}}{\partial I} = V$$

$$\frac{\partial \dot{Q}_{elec}}{\partial V} = I$$

It is assumed that there is no correlation between I and V errors. Hence,

$$U_{\dot{Q}_{elec}} = \sqrt{(\frac{\partial \dot{Q}_{elec}}{\partial V} \times B_V)^2 + (\frac{\partial \dot{Q}_{elec}}{\partial I} \times B_I)^2}$$

A.16 Power reaching the aperture, $\dot{Q}_{avail}$

The dimensions of the mirror aperture are:

$L = 1.99\ m$;

$W = 1.2\ m$;

$Area = L \times W$;

It is assumed that:

$U_L = 0.005\ m$

$U_W = 0.002\ m$

$\frac{\partial Area}{\partial W} = L$

$\frac{\partial Area}{\partial L} = W$

$U_{Area} = \sqrt{(\frac{\partial Area}{\partial L} \times U_L)^2 + (\frac{\partial Area}{\partial W} \times U_W)^2}$

The effect of tracking errors are ignored due to the very high accuracy of the NEP tracking system.

A.17 Efficiency, η

The output parameter is called $\dot{Q}$. This can be $\dot{Q}_{hot}$, $\dot{Q}_{cold}$ or $\dot{Q}_{elec}$. The efficiency term is calculated as below:

$\eta = \frac{\dot{Q}}{\dot{Q}_{avail}}$

$$U_\eta = \sqrt{(\frac{\partial \eta}{\partial \dot{Q}} \times U_{\dot{Q}})^2 + (\frac{\partial \eta}{\partial \dot{Q}_{avail}} \times U_{\dot{Q}_{avail}})^2}$$